

Optimisation of ICON-CLM for the EURO-CORDEX domain: developments, sensitivities, tuning

Beate Geyer¹, Angelo Campanale², Evgenii Churiulin³, Hendrik Feldmann³, Klaus Goergen⁴, Stefan Hagemann¹, Ha Thi Minh Ho-Hagemann¹, Muhammed Muhshif Karadan⁵, Klaus Keuler⁵, Pavel Khain⁶, Divyaja Lawand⁵, Patrick Ludwig³, Vera Maurer⁷, Sergei Petrov^{1,*}, Stefan Poll⁴, Christopher Purr⁷, Emmanuele Russo⁸, Martina Schubert-Frisius⁹, Jan-Peter Schulz^{7,2}, Shweta Singh⁷, Christian Steger⁷, Heimo Truhetz¹⁰, and Andreas Will^{5,*}

¹Institute of Coastal Systems, Helmholtz-Zentrum Hereon, Geesthacht, Germany

²Euro-Mediterranean Center on Climate Change (CMCC Foundation), Caserta, Italy

³Institute of Meteorology and Climate Research Troposphere Research (IMKTRO), Karlsruhe Institute of Technology, Karlsruhe, Germany

⁴Institut für Bio- und Geowissenschaften (Agrosphere, IBG-3), Forschungszentrum Jülich, Jülich, Germany

⁵Fachgebiet Atmosphärische Prozesse, Brandenburgische Technische Universität Cottbus-Senftenberg, Cottbus, Germany

⁶Israel Meteorological Service, Bet-Dagan, Israel

⁷Deutscher Wetterdienst, Offenbach am Main, Germany

⁸Institute for Atmospheric and Climate Science, ETH Zurich, Zürich, Switzerland

⁹GERICS, Helmholtz-Zentrum Hereon, Geesthacht, Germany

¹⁰Wegener Center for Climate and Global Change (WEGC) - University of Graz, Graz, Austria

*These authors contributed equally to this work.

Correspondence: Beate Geyer (beate.geyer@hereon.de)

Abstract. Optimising the model performance to reduce model biases is a challenging task in global and regional climate modelling, especially relevant for free-running climate change simulations. This challenge is addressed in the present study through a systematic regional climate model tuning strategy using a novel methodology, which includes an iterative update of the reference configuration and combines expert judgement with objective tuning using a Linear Meta-Model optimisation (LiMMo) to derive an optimised model configuration. We applied this methodology to the regional climate model ICON-CLM setup over Europe at 12 km grid size (EURO-CORDEX domain) in order to reduce, e.g., the overestimation of incoming solar radiation and too low 2-m temperature. During this process, the sensitivity of the model to changes of 29 model parameters and their physical consistency was tested and investigated. Comparing the results of optimisation by expert judgement with those of LiMMo showed that the latter not only confirmed the expert judgement by focusing on a priori known highly sensitive parameters, but also allowed for fine-tuning of the model configuration with explicit control over the tuning process, making parameter combinations more efficient. With reference to the default ICON numerical weather prediction configuration, the model optimisation yielded significant improvements for a real climate mode simulations use case. For example, biases in incoming short wave radiation could be reduced by 30 %, latent heat flux biases by 15 %, by tuning cloud parameters in combination with surface flux parameters. Furthermore, the new optimised configuration could only be reached by using updated, higher-quality external datasets, including transient aerosols. Based on the community-based coordinated parameter tuning, we recommend an ICON-CLM model configuration for the EURO-CORDEX domain that is already being used for the downscaling of global CMIP6 simulations.

1 Introduction

The Icosahedral Non-hydrostatic (ICON) model is a flexible and scalable high-performance modelling framework for weather, climate, and environmental predictions and projections (Zängl et al., 2015, 2022; Müller et al., 2025). ICON is a joint project of Deutscher Wetterdienst (DWD), Max-Planck-Institute for Meteorology (MPI-M), the German Climate Computing Center (DKRZ), the Karlsruhe Institute of Technology (KIT), and the Center for Climate Systems Modeling (C2SM). The Consortium for Small-Scale Modeling (COSMO, www.cosmo-model.org) and the Climate Limited-area Modelling Community (CLM-Community, www.clm-community.eu) are collaborating partners in the areas of limited-area numerical weather prediction (NWP) and regional climate modelling (RCM).

ICON was introduced for operational global weather predictions at DWD in 2015 and has developed into one of the world's leading weather prediction models in recent years, according to weather prediction skill scores. Due to the different time scales involved, the model quality requirements and verification/evaluation processes are different between NWP and RCM applications. The former is used for short-term weather forecasts (up to two weeks), while the latter is employed for long-term, free-running climate projections until the end of the 21st century or beyond. To use ICON for regional climate projections, however, some modifications to the model source code and adjustments of the model configuration and parameter settings are required.

To use ICON in climate limited-area mode (ICON-CLM), developments and adjustments began in September 2014 with the establishment of the CLM-Community ICON Project Group. Based on ICON release 2.6.1, the first version of ICON-CLM was presented in 2021 (Pham et al., 2021). This included the testing of domain decomposition, restarts, and usage of different time steps, with a horizontal resolution of R2B8 (approximately 10 km) over the limited area pan-European EURO-CORDEX domain. Although the initial evaluation of the first version of ICON-CLM showed very promising results, the model configuration was based on the default NWP configuration for global NWP simulations (Pham et al., 2021).

Since the last two years, new ICON versions have been released biannually. The ICON-CLM model has been used in various studies as both an atmospheric-only model (Sieck et al., 2026) and a regional Earth system coupled model (Ho-Hagemann et al., 2024; Maurer et al., 2025). It has been, or is currently being, used in several national projects to assess recent and future climate developments in Germany and Europe. These projects include NUKLEUS (Sieck, 2020), UDAG (Früh, 2023), DAS-Basisdienst (DWD, 2023) and CoastalFutures (Schrum, 2021). In these studies, different versions of ICON with various namelist or parameter settings were used. While the simulations generally agree well with observations, there is still potential to reduce model biases, particularly in radiation and cloud processes (Maurer et al., 2025). Up to now, no comprehensive tuning procedure has been used to optimise the model quality for ICON in RCM use. It is important to note that different ICON-CLM configurations (model version, forcing, domain, grid resolution) require their own tunings to achieve the best regional climate simulation for a specific research domain. This process requires a significant amount of effort from various members of the CLM-Community at different institutions.

Parameter tuning is essential in Earth system modelling to align simulations with observations, supporting applications from weather forecasting (Zängl, 2023) to climate projections (Mauritsen and Roeckner, 2020). An increase in model complexity and resolution increases computational demands, creating a need for efficient and transparent tuning methods. All methods rely on high-quality observational datasets, and the selection of these datasets can influence the results. Four main approaches are usually used in climate modelling (Hourdin et al., 2017). First, expert tuning based on a manual model configuration adjustment based on expert judgement and experience (e.g., Mauritsen et al., 2012). Second, metamodel-based tuning, where surrogate models approximate full simulations (Neelin et al., 2010; Bellprat et al., 2012). Third, Bayesian calibration, using uncertainty and prior knowledge to estimate model parameters (e.g., Hourdin et al., 2023). Fourth, hierarchical emulators, which combine multi-resolution outputs to balance cost and accuracy of simulations vs biases (e.g., Williamson et al., 2012).

One objective of the CLM-Community is to provide community members with well-tested and thoroughly evaluated model versions and setups. This is of particular importance for versions and configurations that will be used in production, e.g., in 2025 as part of the COordinated Regional Climate Downscaling Experiment (CORDEX, 2025) of the World Climate Research Programme (WCRP), as these data are frequently used for climate services, adaptation planning, and policy consultancy. An extensive evaluation of COSMO 5.0, the predecessor of ICON, was carried out by the CLM-Community in 2014/15 (Anders et al., 2024) and of COSMO 6.0 in 2023/24 (Geyer, 2026). These tests were organised into phases of internal community projects called COPAT (Coordinated Parameter Testing): COPAT1 for COSMO 5.0 and COPAT2 for COSMO 6.0. This procedure has now been repeated and advanced for ICON-CLM to release the first officially recommended version and configuration of ICON-CLM, which will be used to downscale global simulations of the Coupled Model Intercomparison Project Phase 6

(CMIP6; Eyring et al., 2016) in the context of the European branch of the Coordinated Regional Downscaling experiment (EURO-CORDEX) of the WCRP. Therefore, the focus of this study is on the European domain, as many CLM Community member institutions primarily concentrate their research interests on Europe and run simulations for this region. The COPAT comprehensive tuning and evaluation activities are a highlight of the CLM-Community. To our knowledge, these activities have not been performed and reported in other regional climate model development communities, making the CLM-Community unique in this regard.

This paper has the following goals: (I) It provides a description of the complete RCM tuning strategy to optimise the configuration of ICON-CLM for the EURO-CORDEX domain with a resolution of 0.11° (approx. 12 km, Fig. S1) for a real use case. (II) Additionally, it introduces necessary model developments and adjustments to improve performance. (III) To optimise the model quality, we started with extensive ICON-CLM sensitivity tests, which provide insights into general model behaviour. (IV) The ensuing expert tuning in combination with the novel Linear Meta Model optimisation tuning (LiMMo; Petrov et al., 2025) is demonstrated. LiMMo belongs to the second category of parameter tuning methods - the objective calibration. (V) Finally, an optimum ICON-CLM regional climate simulation configuration is derived and presented. Model simulations were objectively evaluated by comparing them with various observational and ERA5 reanalysis data (Hersbach et al., 2020). The tests were mainly conducted in 2023 and 2024, incorporating the ICON release 2.6.6 and the ICON open-source release icon_2024.07 (ICON partnership (DWD, MPI-M, DKRZ, KIT, C2SM), 2024). The final test was performed using version icon_2024.07, which incorporates all additional developments; hence, the optimised configuration is widely usable.

The paper is structured as follows. Section 2 presents the data and methods used in this study, including the RCM tuning concept and a detailed description of the procedures. Section 3 shows the results of the sensitivity study, tuning outcomes for ICON-CLM and a comparison of expert and objective LiMMo tuning. The last section concludes with a summary of findings.

2 Methods

We first introduce an overview of our four-stage RCM configuration optimisation procedure (Sect. 2.1) applied in this study (reference, measures, expert, and LiMMo tuning) and highlight the most relevant technical steps of the ICON-CLM configuration optimisation for each of the tuning methods. In Sect. 2.2, we outline ICON-CLM standard parametrisations and new developments considered in the optimisation procedure. In Sect. 2.3, we describe the basic model setup with special emphasis on the external datasets and the design of our study. Note that each configuration tested in the COPAT2 experiment has been assigned a unique identifier. In Sect. 2.4, we briefly describe the LiMMo tuning framework, i.e. the linear meta-model and the optimisation framework. This optimisation framework has been developed as part of the study presented in this paper and is described in detail by Petrov et al. (2025). In Sect. 2.5, we introduce the observational reference data and the evaluated model variables used in this study. Finally, we present the evaluation measures (Sect. 2.6).

2.1 Tuning Strategy

100 The tuning strategy has been developed during the COPAT2 initiative of the CLM-Community. It is designed to systematically tune RCMs. The strategy with its four stages is shown in Fig. 1 and briefly described below. It should be noted that stage 3 (expert tuning) and stage 4 (LiMMo tuning) are alternative methods of finding an optimised configuration. In our study, both methods have been applied.

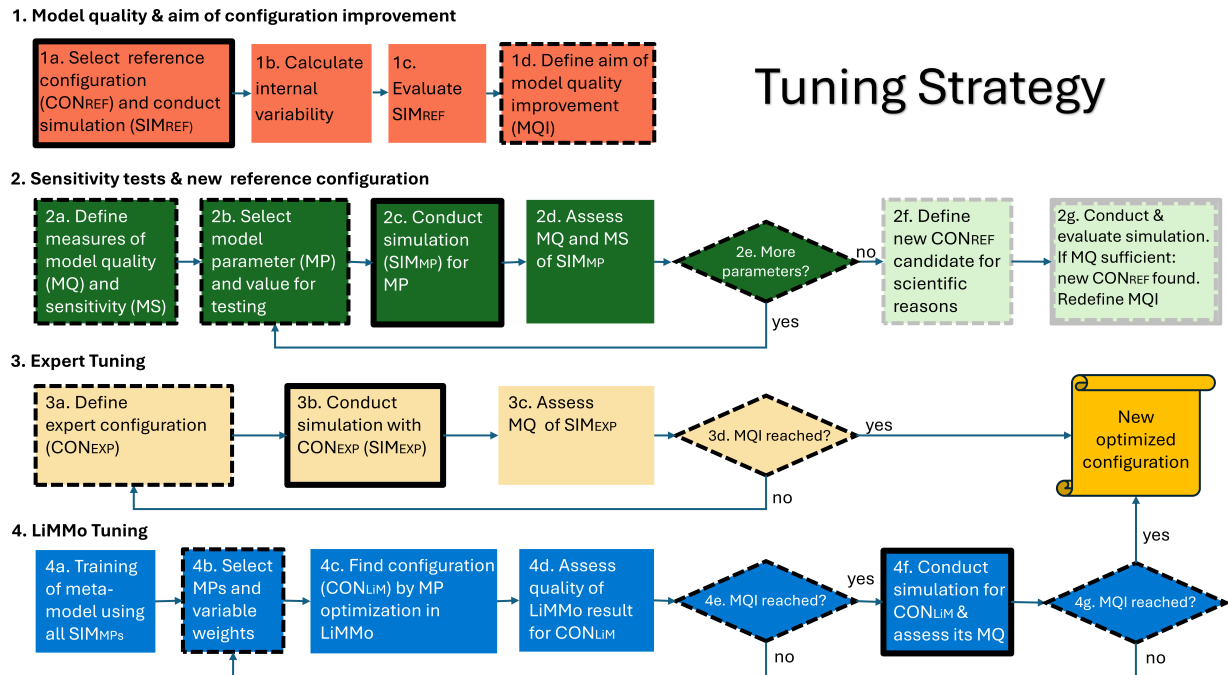


Figure 1. RCM tuning strategy framework. The four rows correspond to four stages. Rectangles correspond to activities, diamond-shaped polygons correspond to decisions. A thick solid frame (1a, 2c, 3b, and 4f) marks computationally intensive activities; a dashed frame (1d, 2a, 2b, 2e, 2f, 2g, 3a, 3d, 4b, 4e, and 4g) marks activities that require expert judgement. Light yellow and green colours indicate optional steps.

105 **‘The model quality & aim of configuration improvement’** (row 1). A definition of the tuning aim (1d) is the starting point for the tuning process (rows 3 and 4). This requires selecting the initial configuration and performing the corresponding simulation (1a). The initial configuration might come from previous tuning initiatives or from other applications of the model (for example, from NWP configurations of a weather service). In this study, we used the configuration C2I101 suggested by the NUKLEUS project (see Sect. 2.3.2) as our initial configuration. The computation of the simulations’ corresponding intrinsic variability came next (1b); it was determined by the monthly Root Mean Square (RMS) differences between two simulations with disturbed initial conditions (see Sect. 2.4.2 and Table 4). In this study perturbed simulations are identified as
 110 C2I200 and C2I207 (Table D1). Intrinsic variability is used to identify significant model biases and changes in RCM results

due to configuration changes. It is also used to define the non-dimensional norm of a simulation's quality (see Sect. 2.4.2). Following that, the evaluation of the reference simulation (1c) takes place. The tuning aim (1d) depends on the evaluation in 1c and the general simulation purpose or aim, i.e., the intended use of the simulation. As the insight into model behaviour, sensitivity, and biases grows during the optimisation process, the tuning aim may be iteratively revised.

The second stage, '**Sensitivity tests & new reference configuration**' (row 2), consists of investigating the effects of single parameter changes and finding a new reference configuration that is better from a physical point of view than the initial one. The first step (2a) is devoted to the definition of the quality norm that quantitatively represents the tuning aim (1d). In our case, we use the comprehensive ScoPi score (see Sect. 2.6.1), the simple RMSE, and seasonal 2D biases to judge the quality of individual simulations compared to independent reference data. In addition, the sensitivity of the model with respect to parameter changes in its configuration is derived from parameter sensitivity tests (2a). To do so, we use the sensitivity measure presented in Sect. 2.6.2. The selection of the specific parameters of the configuration and their values to be tested (2b) is based on expert suggestions and the availability of newly developed external datasets that are relevant for climate simulations, like soil data, aerosols, orography, etc., which also affect the performance of a simulation (see Table 5). Once the simulations with the changed configurations and external parameters are conducted (2c), they are evaluated in terms of quality and sensitivity (2d). To efficiently analyse the model quality and model sensitivity, parameters are grouped according to physical processes in the model (Sect. 3.2). In our study, new reference configurations, C2I200c and later on C2I250c (Table C1), were found as a result of stage 2. Further results of stage 2 can be found in Sect. 3.2.

After conducting and evaluating all sensitivity tests for changes of single parameters in the model configuration in stage 2, the tuning effects of combined parameter changes are quantified. In the current study, we present two options for tuning: The first option, '**Expert Tuning**' (row 3), involves manual selection of parameter combinations based on insights from the previous stage, with the goal of reducing key model biases. The results are discussed in Sect. 3.4.1. The second option is the novel meta-model-based '**LiMMo Tuning**' (row 4), in which the user-defined optimisation procedure automatically selects parameter values. It is introduced in Sect. 2.4, and the results of its application are discussed in Sect. 3.4.2. An important advantage of LiMMo over expert tuning is that simulations with combined parameter changes are not needed for LiMMo tuning (compare 3b to 4f). Instead, users can use the meta-model like an experimental environment and obtain approximations of optimised configuration model results without performing computationally intensive simulations. In our study, as a result of expert tuning, the C2I268c configuration was found. The LiMMo optimisation yielded the C2I291c and C2I294c configurations (see Table C1).

140 2.2 ICON-CLM parameterisations

ICON-CLM is based on the limited-area mode of ICON for NWP. The core element of ICON-CLM is a non-hydrostatic, fully compressible numerical solver that is formulated on an icosahedral-triangular Arakawa-C grid and provides exact local mass conservation and mass-consistent tracer transport. In order to make ICON-CLM applicable in RCM applications, further developments and adjustments, such as transient anthropogenic greenhouse concentrations and aerosols or time-dependent sea surface temperatures, are included.

A detailed description of ICON dynamics can be found in Zängl et al. (2015) and first insights into the specialities of the climate mode in Pham et al. (2021). Here, we describe the relevant applied general physical parameterisations of ICON (Sect. 2.2.1). Afterwards, we discuss newly introduced climate-specific parameterisations of surface fluxes (Sect. 2.2.2) and cloud cover (Sect. 2.2.3) that turned out to be relevant in the course of the stage 2 model quality checking, which are meanwhile parts of the official ICON releases.

2.2.1 Standard physical parameterisations

‘Fast physics’ (called every advection time step): The land surface scheme TERRA (Schrodin and Heise, 2001; Schulz et al., 2016) provides vertical profiles of prognostic soil temperature, water, and ice for up to nine surface tiles (up to three different land use tiles, three snow tiles, and three water tiles). Recent developments include a new resistance-based formulation of bare soil evaporation and a new technique for computing the surface temperature, the so-called skin temperature (Schulz and Vogel, 2020). Both developments improve the prediction of the 2-m temperature, for instance, and other surface variables (Geyer, 2026). The effects of urban structures at the land surface are described by the urban model TERRA_URB (Wouters et al., 2016, 2017), which was ported from the COSMO model to ICON in the framework of the COSMO Consortium’s Priority Project CITTÀ (Schulz et al., 2022; Campanale et al., 2025). The freshwater lake model FLake (Mironov, 2008) and a sea ice scheme derived from FLake (Mironov et al., 2012) provide prognostic surface temperatures over lakes and sea ice, respectively. The turbulent transfer and diffusion schemes of ICON are based on the Mellor-Yamada level-2 scheme, using a prognostic equation for turbulent kinetic energy (Raschendorfer, 2001). The turbulent transfer, i.e., the computation of transfer coefficients and with that of surface turbulent heat fluxes, is done on every surface tile. The grid-scale precipitation scheme accounts for precipitation formation over the ice phase, using the hydrometeor categories of cloud water, cloud ice, rainwater, and snow (Seifert, 2008).

‘Slow physics’ (called at lower frequency): The shortwave and longwave radiation are computed with ‘ecRad’, the radiation scheme of the European Centre for Medium-Range Weather Forecasts (ECMWF), as introduced by Hogan and Bozzo (2018). Its implementation in ICON is described by Rieger (2019). The Tiedtke-Bechtold scheme for shallow and deep convection (Tiedtke, 1989; Bechtold et al., 2008) was adopted from ECMWF’s Integrated Forecasting System (IFS) model. The grid-scale effects by the sub-grid scale orography (SSO) are described by IFS’s SSO scheme (Lott and Miller, 1997; Schulz, 2008), and grid-scale effects by the non-orographic gravity-wave drag are based on Orr et al. (2010). Cloud cover is represented by a diagnostic scheme using a quadratic distribution function of total water (sum of water vapour and cloud water) for liquid clouds, and an analogous equation for ice clouds, also taking convective anvils into account.

2.2.2 New developments in parameterisation of surface fluxes

The distribution of the incoming short-wave radiation between the components of the surface energy budget can be tuned by specifying scaling parameters. The sensitivities of the modelled climate with respect to the most important of these parameters have been tested during parameter optimisation in this study, however, near surface temperature biases remained and therefore, additional tuning parameters were introduced: the soil-moisture dependent tuning of the surface albedo and a factor on the

180 minimum stomata resistance attributed to each land-use type given by external data (GLOBCOVER). These new parameters are part of the official ICON release now.

The portion of incoming solar energy absorbed at the surface depends on the surface albedo. Therefore, the albedo strongly influences the heating of the soil. In ICON-CLM, we prescribe monthly MODIS surface albedo (Schaaf and Wang, 2021) at the land surface. This encompasses the vegetation type and the bare soil albedo. A new parameter `tune_albedo_wso` (with its values abbreviated to *taw*) was introduced, correcting the albedo for very dry soils with *taw1* and very wet ones with *taw2* 185 for the soil types sand, sandy loam, loam, and loamy clay (soil types 3-6 in TERRA). The idea behind this tuning is that wetter soils are darker and, thus, less reflective. The albedo α is corrected by α_c , dependent on soil moisture in the top soil layer w_{so}^{top} , whose thickness Δz_{so}^{top} is set to 10 mm in the parameterisation. The albedo for the near-infrared (nir), visible (vis), and ultraviolet (uv) wavelength bands $\alpha_{i,0}$ is corrected as follows:

$$\alpha_i(w_{so}^{top}) = \max[\alpha_{i,0} \cdot (1 + \alpha_{vis,c}(w_{so}^{top})/\alpha_{vis,0}), \alpha_{i,\min}] \quad (1)$$

190 with $i \in \{\text{nir}, \text{vis}, \text{uv}\}$, $\alpha_{nir,\min} = 0.08$, $\alpha_{vis,\min} = 0.05$, $\alpha_{uv,\min} = 0.02$, $\alpha_{i,0}$: uncorrected albedo

The limit values $\alpha_{i,\min}$ used in the ICON model remained unchanged. The albedo correction of the visible band $\alpha_{vis,c}$ is introduced for dry (*taw1*) and wet (*taw2*) soils with a smooth transition between the soil moisture $w_{so,d}^{top}$ (dry limit) and $w_{so,w}^{top}$ (wet limit) in the following way:

$$\alpha_{vis,c}(w_{so}^{top}) = \begin{cases} taw1 & \text{if } w_{so}^{top} \leq w_{so,d}^{top} \\ taw2 & \text{if } w_{so}^{top} \geq w_{so,w}^{top} \\ taw2 + (taw1 - taw2) \sin^2\left[\frac{\pi(w_{so}^{top} + 3w_{so,w}^{top} - 4w_{so,d}^{top})}{2(w_{so,w}^{top} - w_{so,d}^{top})}\right] & \text{otherwise} \end{cases}$$

195 We use the soil moisture limit values

$$w_{so,d}^{top} = 0.001 \text{ m} \hat{=} 0.1 \cdot \Delta z_{so}^{top} \text{ and } w_{so,w}^{top} = 0.002 \text{ m} \hat{=} 0.2 \cdot \Delta z_{so}^{top}.$$

Using $\alpha_{vis,c}(w_{so}^{top})$, the corrected albedos α_{vis} , α_{nir} , and α_{uv} are determined via Eq. 1. The correction is done only for the vegetation-free part of each tile. At the end of the albedo routine, the values are aggregated over all tiles.

200 The most important tuning parameters for further fine-tuning the surface energy budget by affecting the turbulent heat fluxes are the resistances to the fluxes in the laminar boundary layer: `rlam_heat`, `cr_bsmin`, `rat_lam`, `rat_sea`, `rsmin_fac`. In addition to the parameters already available in the model, the parameter `rsmin_fac` has been introduced in order to have the opportunity of tuning the latent and sensible fluxes independently over water and over land. Table 1 gives an overview of the impacts of the resistance parameters on the heat fluxes and surface types.

205 The main resistance parameter that scales both fluxes over land and water surfaces is `rlam_heat`. The parameter `rat_sea` is scaling the resistance of the fluxes over water. Here, the latent heat flux is equal to potential evaporation. The resistances and their scaling factors for vegetation, the land-use class-dependent evaporation/stomata resistance for plants are tunable by adjusting `rsmin_fac`. `cr_bsmin` is the tunable minimal bare soil resistance for evaporation. `rat_lam` influences the latent heat flux over land only.

All namelist parameters used are listed with a short description in Table A1.

Table 1. Parameters of turbulent heat flux resistance

	bare soil	vegetation	water
sensible	$r_{lam_heat} \times cr_bsmin$	$r_{lam_heat} \times r_{smin_fac}$	$r_{lam_heat} \times rat_sea$
latent	$r_{lam_heat} \times cr_bsmin \times rat_lam$	$r_{lam_heat} \times r_{smin_fac} \times rat_lam$	$r_{lam_heat} \times rat_sea$

210 2.2.3 New developments in parameterisation of sub-grid scale cloud cover

The ICON model includes three parameterisations that contribute to the simulated cloud cover. These encompass grid-scale cloud cover, subgrid-scale cloud cover from convection parameterisation, and subgrid-scale cloud cover from stratus or stratocumulus shallow clouds. The grid-scale cloud cover occurs when the grid-box relative humidity (**rh**) reaches 100 %. In this case, the cloud cover is automatically set to one, and the microphysics parameterisation is initiated, potentially producing precipitation. When **rh** is below 100 %, the grid-scale cloud cover remains zero. When the grid box **rh** is below 100 % but the stratification is unstable, the convection parameterisation is activated, and the cloud cover is estimated from the cloud water detained into the anvil (Bechtold et al., 2008). This cloud cover aims to describe shallow or penetrative cumulus, which may produce light to medium precipitation. The third cloud cover parameterisation is the subgrid-scale cloud cover of stratus or stratocumulus shallow clouds (Prill et al., 2024). When the grid-box mean **rh** is slightly below 100 % and subgrid-scale turbulent fluctuations are large enough, the grid box may contain small clouds (with **rh** of 100 %) and cloud-free areas with **rh** below 100 %. The turbulent fluctuations are parametrised using a top-hat total water distribution with a fixed half-width, which is around 5 % of the total water, which means that the water content varies uniformly within a narrow range around the mean value. This leads to a quadratic dependence of the subgrid-scale cloud cover on the total water.

The subgrid-scale cloud cover parameterisation due to turbulence is regarded as most uncertain, and therefore several parameters of the scheme are introduced as tuning parameters in ICON. The parameter `tune_box_liq` determines the half-width of the top-hat total water distribution. The parameter `tune_box_liq_asy` is a scaling factor that determines the asymmetry term of the cloud cover for over- and undersaturation. The quadratic increase of cloud cover from 0 to 1 ranges between rh_i and rh_f , where

$$\begin{aligned}
 rh_i &= 100 \cdot (1 - 2 \cdot tune_box_liq \cdot tune_box_liq_asy), \\
 rh_f &= 100 \cdot (1 + 2 \cdot tune_box_liq).
 \end{aligned}
 \tag{2}$$

In practice, since **rh** is not allowed to exceed 100 %, the cloud cover is cut off and does not reach 1 at **rh** = 100 %. With higher `tune_box_liq` or `tune_box_liq_asy`, the quadratic increase of cloud cover starts at lower rh_i , resulting in higher cloud cover. However, the increase of `tune_box_liq_asy` leads to the increase of cloud cover for the entire range between rh_i and **rh** = 100 %, while the increase of `tune_box_liq` does not change the value of the cloud cover at **rh** = 100 %. Therefore, a higher sensitivity is expected to `tune_box_liq_asy` in comparison to `tune_box_liq`. Practically, the increase of cloud cover at lower **rh** is reflected in larger areas covered by partial cloudiness.

Finally, the scaling parameter `allow_overcast` determines the steepness of the parabolic function. Its decrease increases the steepness, preserving rh_i . As a result, a lower `allow_overcast` results in a higher cloud cover, especially at **rh** close to 100 %. This increase is reflected in the appearance of local spots with full overcast.

240 We used the ICON namelist parameter `allow_overcast` with a newly introduced monthly dependency. This change was inspired by the identification of monthly variations in model errors through a detailed analysis of test simulations. Technically, we simulated in monthly chunks and passed the appropriate monthly value to the namelist. It is defined for the month m as the mean value ao with added user-defined deviations from the mean **aoac**, scaled with a tunable amplitude aoa :

$$\text{allow_overcast}[m] = ao + aoa \cdot \mathbf{aoac}[m]. \quad (3)$$

245 Since this parameterisation does not include precipitation production, the described parameters affect the simulated radiation transfer through the clouds only. Therefore, their tuning is useful for correcting global radiation biases related to uncertainties in subgrid-scale cloud cover.

2.3 ICON-CLM model setup

This section provides an overview of our specific settings for this study. First, we provide a general description of the setup
250 of ICON-CLM (Sect. 2.3.1), followed by an explanation of the design and naming conventions of the experiments in this study (Sect. 2.3.2). A special focus is put on the transient forcing of aerosol and ozone and the time-dependent insolation in Sect. 2.3.3.

2.3.1 ICON-CLM basic model setup

The ICON-CLM model domain for this study is the EURO-CORDEX region. The horizontal grid resolution is R13B5 in ICON
255 terminology, which equals a mesh size of 12.14 km (Fig. S1). Vertically, a hybrid height-based terrain-following coordinate (Smooth L_Evel V_Ertical (SLEVE) coordinate; Schär et al., 2002) is used with 60 layers up to a model top of 23.5 km. We use a model time step for advection of 100 s. In this study, ICON-CLM is driven by 3-hourly ERA5 reanalysis data (Hersbach et al., 2020). In previous tests (Sieck et al., 2026), it became obvious that an upper-boundary nudging towards the ERA5 data was beneficial for the European model domain due to the very large extension of the domain: The centre points of the western and
260 the eastern boundaries are more than 7000 km apart. During the transition between summer and winter, high and low-pressure systems develop and travel across Europe at a high frequency. The nudging communicates these developments to the regional model and avoids strong boundary effects. It is applied above a height of 10.5 km to the horizontal wind components and additionally to the density and the virtual potential temperature using pressure, temperature, and specific humidity of ERA5. The nudging coefficient is maximum (i.e., = 1) at the uppermost level and decreases to < 0.5 in the third model layer from the
265 top (full level height of 18.87 km), < 0.25 in the fifth (at 16.34 km height), and < 0.1 in the ninth (14.06 km).

At the ocean surface, ICON-CLM is using interpolated sea surface temperatures and sea ice fraction from ERA5. All boundary data are updated every three hours.

The ICON model provides different functionalities for the temporal aggregation of output variables and for vertical interpolation. We use the aggregation typical for climate variables and the interpolation to pressure levels and levels of constant height above mean sea level. ICON-CLM is running in a scripting framework or workflow engine, the so-called Starter Package for ICON-CLM Experiments (SPICE, Geyer et al., 2025a). The workflow consists of a parallel pre-processing of the lateral boundary conditions, the ICON-CLM simulation itself, post-processing, and archiving. The post-processing includes the interpolation of model output from the R13B5 ICON grid to the rotated EUR-12 grid and the generation of time series, the interpolation to constant heights above ground, and the calculation of typical climate variables like potential evapotranspiration, which are not directly diagnosed within ICON.

2.3.2 Reference simulation and study design

The reference simulation is the experiment C2I101 (Geyer et al., 2025b, reference configuration for experiments listed in Table C1). It is using the general setup as described in Sect. 2.3.1 and the physical parameterisations as described in Sect. 2.2.1, apart from the urban parametrisation TERRA_URB. As external parameters, GLOBE orography data (Team et al., 1999), FAO soil types (Food and Agriculture Organization of the United Nations, 2003), land-use data from GLOBCOVER2009 (European Space Agency and Université Catholique de Louvain, 2010), monthly varying Tegen aerosols (Tegen et al., 1997), and MODIS surface albedo (Schaaf and Wang, 2021) for different wavelength bands were used. Spectral solar irradiance (Coddington et al., 2016) and ozone data (Global and regional Earth-system Monitoring using Satellite and in-situ data project (GEMS) climatology merged with data by the project ‘Monitoring Atmospheric Composition and Climate’ (MACC), Inness et al., 2009, 2015) were prescribed as in the default NWP setup for global applications. These settings constitute the reference configuration (Fig. 1, stage 1g) for all experiments conducted in the definition phase of a new reference, where we mainly tested the external datasets, existing alternative parametrisations, and a group of parameters. Table A1 provides an overview of the tested parameters along with their descriptions, while Table C1 details the specific modifications applied in each experiment, identified by IDs ranging from C2I101 to C2I130. Here, all simulations were conducted for the period 1979–1984, with the period 1980–1984 used for model evaluation and shown in the figures with seasonal means. The initial year served as a spin-up period to allow the system to reach a quasi-equilibrium state (Table B1). An alternative initialisation with soil moisture from a longer spin-up experiment is available among the sensitivity experiments.

The new reference was defined as (C2I200 / C2I200c) according to the tuning strategy (Fig. 1, stage 2g), using new settings as for example, transient aerosols (cf. Sect. 3.3 and Table D1 for more details). For the tuning process, a second time period, 2002–2008, was used (experiment IDs C2I2**c). The period from 2003 to 2008 was used for the evaluation and tuning, and the figures refer to the seasonal means obtained from this period. This second period was added to increase the number of available observational data, as sufficient satellite data are not available in earlier times. Optimised LiMMo configurations were tested in experiments C2I291c and C2I294c (cf. tuning strategy step 4f). The ICON namelist parameters and the simulation acronyms are written in the manuscript with font `typewriter`.

Since the tuning initiative took place at the same time as the development of the ICON source code, the model version was changed several times during the process (see Table B2).

2.3.3 Transient Forcing

The settings for the transient forcing of aerosol and ozone and the time-dependent insolation were gradually adopted from the ICON setup for coupled global climate projections, ICON-XPP, (Müller et al., 2025); see experiments C2I105, C2I118, 305 C2I119 (Table C1) for a description of the respective ICON settings. The implementations were adopted from a predecessor of ICON-XPP, called ICON-ESM (Jungclaus et al., 2022), which are in turn very similar to those in the atmospheric part of the general circulation model by the Max-Planck-Institute, ECHAM-6 (Stevens et al., 2013). The main development had to be invested into the treatment of the input parameters provided by these climatologies, which required adaptations in the radiation interface for ecRad. For the aerosols, the input of the transient ‘Max Planck Aerosol Climatology Version 2’ (MACv2) of 310 Kinne (2019a) is implemented, with the option to use the simple plume scheme MACv2-SP of Stevens et al. (2017). Only the simple plume scheme includes the option to account for different aerosol concentrations in dependence on the respective climate scenario. As the optimised setup described in this article will also be used to downscale GCM simulations for different scenarios, the simple plume scheme must be used. Additionally, a transient climatology for volcanic aerosols (Stenchikov et al., 1998) can be read. For ozone, the CMIP6 dataset (Checa-Garcia, 2018) was made available. Moreover, an option to switch on 315 time-dependent spectral solar irradiance as recommended for CMIP6 (Matthes et al., 2017) is available.

Due to the switch from the Tegen aerosol climatology to the transient MACv2-SP climatology, the aerosol-microphysics coupling as used in NWP is not applicable anymore. Therefore, the use of an external MODIS climatology of cloud droplet number concentration (CDNC) was implemented for ICON-XPP, which is tested in C2I241 (see Table D1). The current implementation uses a non-transient, but monthly varying climatology of Gryspeerdt et al. (2022) and was adjusted with a 320 satellite-based CDNC retrieval by Bennartz and Rausch (2017) and Grosvenor et al. (2018) as used in ECMWF’s IFS model. To account for the scenario-dependence of aerosols and, with that, of CDNCs, we implemented a scaling factor that can be derived from the implementation of the simple plume scheme (Fiedler et al., 2019). This implementation is not tested for the periods considered here, but will be used for the production of RCM scenarios.

2.4 LiMMo framework

325 Figure 1 (Stage 4: **LiMMo Tuning**) briefly describes the meta-model-based tuning framework developed and applied in the current study (Petrov et al., 2025). This framework is very useful for leveraging sensitivity simulations (Fig. 1, stage 2c) and adds significant value to the process of finding the optimal model configuration. The first stage of meta-model-based tuning involves statistically approximating the monthly mean climate model output and building (or training) a meta-model, or emulator (Fig. 1, 4a). The next stage is the optimisation loop (Fig. 1, 4b-d). At this stage, the user selects the weights of 330 the model variables in order to scale the terms of the error norm function, which quantifies the discrepancy between the meta-model and the observational data (Fig. 1, 4b). Then, the optimisation procedure is conducted to yield the parameter values that minimise the error norm function (Fig. 1, 4c). Then, the user checks whether the meta-model’s biases with optimal parameter values fulfil the global tuning aim (Fig. 1, 4d). If so, a control test run of the climate model is conducted to confirm the findings. (Fig. 1, 4f).

335 In this section, we give the general description of the framework (Sect. 2.4.1) and present the error norm function that guides an optimisation (Sect. 2.4.2).

2.4.1 General description

The meta-model framework has two distinctive features: first, a linear regression emulator, and second, gradient-based optimisation of meta-model parameters to minimise the error norm between the emulator and the observations.

340 Unlike previous studies, which mainly utilised quadratic regression (Gregoire et al., 2011; Bellprat et al., 2016), the LiMMo concept has successfully proven that linear approximation possesses decent approximation quality for multi-year monthly mean values, requiring only a linear number of simulations (for N parameters, the number of simulations required for training is $O(N)$). Contrary to this, the quadratic regression requires $O(N^2)$ simulations, because one has to conduct one new simulation with every two parameters disturbed simultaneously to approximate the interaction terms. This imposes a significant limitation
 345 on the number of parameters available for tuning.

The linear regression $\text{REG}(\mathbf{p})$ defined in the following equation is a function of the model parameters \mathbf{p} and approximates ICON-CLM variables. The regression yields monthly mean values, which correspond to the climatological monthly means (average December, January, etc.):

$$\text{REG}_{i,j,k,n}(\mathbf{p}) = \text{MOD}_{i,j,k,n}^{\text{ref}} + \sum_m (p_m - p_m^{\text{ref}}) \cdot \mathbf{K}_{i,j,k,n}^m. \quad (4)$$

350 Here, $\text{REG}_{i,j,k,n}$ is the 2D regression result ((i, j) are spatial indices, k is the number of the climatological month, and n is the index of the model variable), $\text{MOD}_{i,j,k,n}^{\text{ref}}$ is the model output for the reference simulation, p_m and p_m^{ref} are the test parameter and reference parameter values for the parameter with index m (corresponding to MOD^{ref}), and $\mathbf{K}_{i,j,k,n}^m$ is the tendency tensor of the parameter p_m . The tendency tensor is assembled explicitly as the linear combination of simulations (see Table 5, column ‘signal’), divided by the parameter increment (see Table 5, columns ‘test value’ and ‘ref value’). Note that the regression in
 355 Eq. 4 is constructed to be exact for the reference parameter values.

To start the experiments with the meta-model, we select the error norm function $\text{ERR}(\mathbf{p})$, which sets the distance between meta-model (Eq. 4) and observational data. We give the details of the error norm function in the following section (Sect. 2.4.2). Mathematically, the aim of the meta-model tuning is to find the vector of model parameters \mathbf{p} that would minimise the $\text{ERR}(\mathbf{p})$.

360 For the linear regression approximation with a spatial RMSE-based error norm, the target minimisation function $\text{ERR}(\mathbf{p})$ is a smooth, convex, scaled Euclidean norm function of the model parameters. This function is known to have only one global minimum. Consequently, the initial parameter values have no impact on the outcome, and the optimisation process always converges to the global minimum. However, this minimum may be on the boundary of the constrained region for certain parameters. This, however, should not be the case for physically consistent parameters and physically meaningful parameter ranges of parameter values admitted. Section 3.4.2 will show that this was not the case for the parameters optimised in this
 365 study.

In previous studies devoted to objective calibration (e.g., Bellprat et al., 2016; Avgoustoglou et al., 2022), Monte Carlo sampling was utilised for this purpose. The general problem of this approach is the exponentially growing complexity with the dimensionality of the parameter space N , which in practice limits N . In previous studies, N was limited to 7–8 parameters.

In the LiMMo framework, the Monte Carlo method is applied to binary parameters (logical and integer value parameters).
 370 The number of these parameters can be significantly higher due to the very fast solution of the linear model. Thus, more sophisticated methods are not necessary to solve this type of problem within a few hours.

For real number parameters, the LiMMo framework suggests the implementation of gradient-based optimisation. This method searches for the next value of the parameter vector $\mathbf{p}^n \rightarrow \mathbf{p}^{n+1}$ in the direction opposite to the gradient of the error norm in the parameter space ($\partial \text{ERR}(\mathbf{p})/\partial \mathbf{p}$), until the increment of the error norm function becomes less than a given threshold
 375 $|\text{ERR}(\mathbf{p}^{n+1}) - \text{ERR}(\mathbf{p}^n)| < \varepsilon$. As proposed by Petrov et al. (2025), the limited-memory Broyden-Fletcher-Goldfarb-Shanno method (Broyden, 1970; Byrd et al., 1995) with box constraints fits really well to the purpose and the convex nature of the problem. This method requires an initial guess and the minimum and maximum parameter values p_m^{\min} and p_m^{\max} to set up the box constraints. The search process is restricted to the defined hyper-rectangle, which ensures that the final result is physically meaningful. The complexity of gradient descent increases linearly with the dimensionality of the parameter space. In practice,
 380 an optimisation with 15–20 parameters is in the order of a few minutes only.

We successfully built a regression meta-model with over 15 parameters and ran multiple optimisation loops (see Sect. 3.4.2). As a result, we obtained several parameter sets derived from LiMMo as final contenders for the new, optimised ICON-CLM configuration.

2.4.2 Error norm

385 In the LiMMo framework, the error norm (single number) between the model output and observational data is calculated using the Root Mean Square Error (RMSE). The observational data are first interpolated onto the model’s output grid. Then, multi-year monthly averages were computed for both the model output and the observational time series.

To compute the error norm, we consider the horizontal model outputs $\text{MOD}_{i,j,k,n}$ for the variables v_n . The indices i and j represent the spatial coordinates on the horizontal grid, while k indicates the month. The observational data $\text{OBS}_{i,j,k,n}$ are
 390 stored in the same multi-year monthly mean manner on the model grid.

The spatially aggregated Root Mean Square Error, $\text{RMSE}_{k,n}$, for each month and variable is given by

$$\text{RMSE}_{k,n} = \sqrt{\frac{1}{N_x \cdot N_y} \sum_{i,j} (\text{MOD}_{i,j,k,n} - \text{OBS}_{i,j,k,n})^2}, \quad (5)$$

where $N_x \cdot N_y$ denotes the number of grid points on the horizontal plane of the simulation domain, excluding the boundary relaxation zones. For each variable and month, the intrinsic variability $\sigma_{k,n}$ is defined as the RMSE between some reference
 395 and its disturbance simulation. In our case, the disturbance is achieved by shifting the initial conditions back by one month:

$$\sigma_{k,n} = \sqrt{\frac{1}{N_x \cdot N_y} \sum_{i,j} (\text{MOD}_{i,j,k,n}^{\text{ref}} - \text{MOD}_{i,j,k,n}^{\text{dis}})^2}. \quad (6)$$

The error ERR_n for each variable is calculated as the time-averaged RMSE normalised by the intrinsic variability, defining the dimensionless signal-to-noise type measure of model prediction quality with respect to observations:

$$ERR_n = \frac{1}{N_t} \sum_k \frac{RMSE_{k,n}}{\sigma_{k,n}}, \quad (7)$$

400 where $N_t = 12$ represents the number of months. Finally, the total error norm, ERR , is defined as the weighted sum of the errors for each variable, which determines the aggregated quality of the model simulation for all the prognostic variables that have been considered:

$$ERR = \sum_n c_n \cdot ERR_n, \quad \sum_n c_n = 1. \quad (8)$$

The weights c_n are chosen by the user to reflect the relative importance of each variable, directly controlled by the optimisation aim (Fig. 1, 1d; see Sect. 3.4.2). The aim of LiMMo tuning is to minimise this error norm (Eq. 8) with respect to the model parameters.

2.5 Observational Datasets and analysed variables

The single-level 2D model variables considered in the evaluation and tuning procedure are listed in Table 2. We use the EURO-CORDEX naming convention (EURO-CORDEX, 2025) to label them. Multiple gridded data sets are used for ScoPI score analysis (see Sect. 2.6.1), LiMMo tuning (see Sect. 2.4.2), and/or comparison with station observations. We will use bold font to emphasise the model variables in the following text.

Table 2. List of considered model variables comprising the variable name according to the EURO-CORDEX convention, a short description, and the respective unit. If the variable is analysed or tuned against observations, the corresponding data source is provided and explained in the main text; '-' indicates that no comparison with observations was done. In addition, the weight of the variable in the ScoPi-score metric (Sect. 2.6.1) is given.

Name	Description	Unit	Observations	ScoPi-weight
clt	total cloud cover percentage	%	CERES	1
dtr	diurnal near-surface temperature range (2 m)	K	E-OBS	1
hfls_o	latent heat flux at water surface (positive up)	W m ⁻²	HOAPS	1
hfls_l	latent heat flux at land surface (positive up)	W m ⁻²	-	-
hfs	sensible heat flux at the surface (positive up)	W m ⁻²	-	-
pr_amount	total precipitation	kg m ⁻²	E-OBS + stations	-
prw	precipitable water	kg m ⁻²	ERA5	1
psl	mean sea level pressure	hPa	E-OBS/ERA5	0.5/1
rh	relative humidity	%	-	-
rlds	downwelling longwave radiation flux at the surface	W m ⁻²	-	-
rhus	upwelling longwave radiation flux at the surface	W m ⁻²	-	-
rsds	downward shortwave radiation at the surface	W m ⁻²	E-OBS + stations	1.5
rsus	upward shortwave radiation flux at the surface	W m ⁻²	-	-
sfcWind/ws	near-surface wind speed (10 m)	m s ⁻¹	E-OBS	1.5
tas	near-surface temperature (2 m)	K	E-OBS	0.66
tasmax	maximum near-surface temperature (2 m)	K	E-OBS	0.66
tasmin	minimum near-surface temperature (2 m)	K	E-OBS	0.66
z0	roughness length	m	-	-

For the evaluation of the model results, detailed comparisons against the gridded observational data set E-OBS version 29 (Cornes et al., 2018) were conducted. Daily data were retrieved on a regular grid with a spatial resolution of ~ 25 km. Additionally, satellite data are used for the 2003–2008 evaluation period, namely HOAPS 4.0 (Andersson et al., 2010, 2017) and CERES (NASA/LARC/SD/ASDC, 2019; Loeb et al., 2018) as monthly mean composites. The variables considered in the evaluation procedure are listed in Table 2.

Additionally, precipitation and radiation observations from weather stations in Germany (Deutscher Wetterdienst, 2025) and Poland (Polish weather service) for 2004 to 2008 were used for the evaluation of the surface energy budget components.

2.6 Evaluation Procedure and Considered Metrics

420 In a first instance, the evaluation is conducted point-by-point on the regular lon-lat grid of the selected observational data set for at least 5 years. Beforehand, simulation data were remapped to the observational grid using bilinear interpolation. The main metrics that we consider in our analyses are the following: mean error (mean BIAS), RMSE, Linear Correlation in time, and the Advanced (symmetric) Mean Squared Error Skill Score (AMSESS), defined after Winterfeldt et al. (2011), see Eq. 9.

$$\text{AMSESS} = \begin{cases} 1 - \sigma_{ts}^2 \cdot \sigma_{ref}^{-2} & \text{if } \sigma_{ts}^2 \leq \sigma_{ref}^2 \\ \sigma_{ref}^2 \cdot \sigma_{ts}^{-2} - 1 & \text{if } \sigma_{ts}^2 > \sigma_{ref}^2 \end{cases}, \quad (9)$$

425 where σ_{ts} and σ_{ref} are the mean squared differences of the test and reference simulations against observations, respectively. The AMSESS varies between -1 and 1, where positive (negative) values indicate improved (worsened) performance of the test simulation with respect to the reference.

We compare the model error against the observations of a given simulation and the respective reference runs for each variable and grid-box, based on the aforementioned metrics. The error of a given simulation against observations might be smaller or
430 larger than the one of the reference run. However, whether these smaller or larger errors are significant must be tested. In the next section, we present a method for making a statistically sound assessment of whether a given simulation is better or worse than the reference in the comparison against observations.

2.6.1 Significance tests and Score Points of evidence - ScoPi

For the significance tests and Score Points of evidence (ScoPi) we followed the approach introduced by Geyer (2026). The
435 ScoPi is calculated point-by-point, considering the 3-daily means or sums, respectively, of the given variables (Table 2). Given that the ERA5 data, used as boundary conditions for the conducted experiments, are ‘realistic’ reanalysis data, we assume that the model can adequately capture the variability of a given variable at synoptic time scales within a single grid cell. This enables, on the one hand, having a time series long enough for testing the robustness of the employed metrics using Monte-Carlo approaches. On the other hand, it allows for making the variables more Gaussian through averaging: this then allows
440 for the application of estimators such as the RMSE, which are better suited for normally distributed data (Hodson, 2022). For CERES cloud cover, monthly mean values are considered instead of 3-daily means, representing the original temporal resolution of the CERES data set. When applying the LiMMo, monthly mean values of the variables are used.

The ScoPi score is described in detail by Geyer (2026). It is dependent on the shares of grid points in a model sub-region, presenting a significant improvement or worsening in a metric for a variable with respect to the reference run. If the share of
445 grid points in a model region with a strong (not only moderate) significance F_{ss} is larger than 0.5, the score is enlarged by 0.5 as given in Eq. 10, F_{ms} denotes the shares with moderate significance.

$$\text{ScoPi} = \begin{cases} F_{ss} + 0.5 \cdot \text{sign}(F_{ss}) & \text{if } |F_{ss}| > 0.5 \\ F_{ms} & \text{otherwise} \end{cases} \quad (10)$$

The great advantage of the ScoPi score is its inherent standardisation for different types of variables. The values always range between -1.5 and 1.5. Therefore, the ScoPi score can be aggregated over different types of variables and metrics. The inspection
 450 of these values allows us to gain a comprehensive understanding of the reasons for possible improvement / worsening in the model performance for a given configuration. The ScoPi score is computed for each PRUDENCE region (see Fig. S1), for different metrics m , seasons s , and various atmospheric variables v . If the share of significant grid points in a sub-region is too small (lower than 0.4), the ScoPi score is not accounted for when aggregated. In this case, it is assumed that there is no noticeable large-scale change in the model results with respect to the reference. The aggregation with respect to a specific
 455 PRUDENCE region is done by calculating the sum over the ScoPi values for all seasons, metrics, and variables (Eq. 11). For integrating over several variables, different weights c_v are considered per variable, as given in Table 2. The resulting value is referred to as ScoPi_{region} .

$$\text{ScoPi}_{region}(r) = \sum_{v,m,s} c_v \text{ScoPi}_{v,m,s}(r) \mathbf{1}(|\text{ScoPi}_{v,m,s}(r)| > 0.4), \quad (11)$$

where $\mathbf{1}(|\text{ScoPi}_{v,m,s}(r)| > 0.4)$ is the indicator function giving 1 for ScoPis larger/smaller than 0.4/-0.4 and 0 elsewhere.

460 The threshold of 0.4 ensures that the majority of the locations in a specific region and for a specific model configuration show a significant improvement / worsening compared to the reference experiment. For instance, if at least 40 % of the grid points show significantly improved performance for simulation B with respect to reference A, the ScoPi score is 0.4, although 60 % of the grid points show no significant changes. The same is true if 60 % of the grid points show significant improvement and 20 % significant worsening.

465 $\text{ScoPi}_{simulation}$ is defined as a weighted sum across all PRUDENCE regions, incorporating additional regional weighting factors (Eq. 12). Each PRUDENCE region is assigned a specific weight, based either on its area or its distance from mid-Europe (domain A4 in Fig. S1). The corresponding weights are listed in Table 3.

$$\text{ScoPi}_{simulation} = \sum_r c_r \cdot \text{ScoPi}_{region}(r), \quad (12)$$

To calculate a $\text{ScoPi}_{simulation}$, it is a prerequisite that each contributing region is analysed with the same set of metrics and
 470 variables. Therefore, it is not possible to summarise regions' results for different variables, i.e., temperatures for land points of PRUDENCE regions and latent heat fluxes of sea points.

Table 3. ScoPi weights according to the region area (middle) or to distance from the domain centre (Germany) (right).

PRUDENCE Region	weight according to distance to Mid-Europe	weight based on area size
Alps	0.0576	0.2000
British Islands	0.0589	0.0212
East-Europe	0.2227	0.0802
France	0.0639	0.0230
Iberian Peninsula	0.1222	0.0440
Mediterranean	0.1168	0.0421
Mid-Europe	0.1094	0.5000
Scandinavia	0.2484	0.0895

The ScoPi is calculated in a first place considering the mean BIAS against observations for all of the given variables. Then, it is also applied to the other metrics mentioned above. When applying the error metric ‘linear correlation’, we used the method proposed by Zou (2007) and described in Geyer et al. (2025a) as a significance test for the differences between two
475 simulations. Tests with several metrics done by Geyer (2026) revealed that the ranking between the tested simulations remains stable in relation to the reference: the higher the ScoPi score, the better the overall performance of the tested simulation.

2.6.2 Sensitivity measure

To quantitatively compare the impact of different parameter changes on model results and to help in the selection of parameters, which are worth considering for further tuning, we introduce the sensitivity measure $\text{SENS}_{n,m}^{\text{seas}}$ for variable v_n on the change
480 of parameter p_m for a specific season (seas). Each sensitivity experiment simulates the change of only one parameter from the reference value p_m^{ref} by an increment of Δp_m . The definition of the sensitivity measure is comparable to the definition of the error norm with respect to observations: (Eq. 7):

$$\text{SENS}_{n,m}^{\text{seas}} = \frac{1}{N_{\text{seas}}} \cdot \sum_{k \in \text{seas}} \frac{1}{\sigma_{k,n}} \cdot \sqrt{\frac{1}{N_x \cdot N_y} \cdot \sum_{i,j} \left(\text{MOD}_{i,j,k,n}^{p_m=p_m^{\text{ref}}+\Delta p_m} - \text{MOD}_{i,j,k,n}^{p_m=p_m^{\text{ref}}} \right)^2}, \quad (13)$$

where N_{seas} is the number of months in a specific season, $\sigma_{k,n}$ is the intrinsic variability of variable v_n for the month number k
485 (Eq. 6), N_x, N_y are the number of grid points along the domain axes, $\text{MOD}_{i,j,k,n}$ is the ICON-CLM model output temporally averaged to monthly mean values for several years (i, j - spatial indices, k is the index of month, n is the index of model variable).

In addition, we applied a grid point mask to the model quantities before calculating the sensitivities, using only the grid points with available observations (E-OBS for all variables except **hfls_o**, and HOAPS for **hfls_o**). This shows the sensitivity
490 only for the relevant part of the model domain.

Within a physically meaningful range of parameters, the sensitivity can be treated as a signal-to-noise ratio. The signal is the RMS difference between the model outputs for the reference configuration and the configuration with the parameter disturbed. The noise is the intrinsic variability of the model. Therefore, statistically significant changes yield a sensitivity value greater than 1. We consider the model to be ‘sensitive’ to a parameter change for $\text{SENS}^{\text{seas}}$ values above 2.

495 **3 Results**

In the results section, we present the sensitivity study and parameter tuning outcomes for ICON-CLM. This section is organised according to the proposed RCM tuning strategy (Fig. 1). First, we determined the intrinsic variabilities of the model for the analysed variables (Sect.3.1). In Sect. 3.2, we investigate how key model quantities respond to changes in 27 tested model parameters. For those parameters that turned out to show a high sensitivity, we discuss 2D seasonal signals that provide valuable
500 insights into the model’s behaviour. In Sect. 3.3, we propose a new reference configuration that uses settings which were found to most effectively improve model quality during the sensitivity study, unless they must be changed for scientific reasons. We also examine the primary biases of the new reference configuration to observations to determine the tuning aim. In Sect. 3.4, the results of the expert- and meta-model-based tuning are presented. Finally, in Sect. 3.5, we carefully evaluate all configurations obtained. One optimum configuration is recommended with respect to simulation quality and computational efficiency, to be
505 used as the new recommended reference configuration for 12 km climate runs over Europe within the CLM-Community.

3.1 Intrinsic variability

One requirement of the tuning strategy is to determine the monthly mean intrinsic variability of the modelled quantities (see Fig. 1, 1b and Sect. 2.4.2), which are used to estimate the model sensitivity. The seasonal mean values are given in Table 4. These values are also used to determine uncertainty ranges during evaluation and tuning processes, as well as the minimum
510 range displayed in seasonal 2D bias plots.

Table 4. The seasonal values of intrinsic variability measure, computed as RMS difference between simulations C2I207 and C2I200 (see Eq. 6 and Table D1). The observation mask is applied to the model output (only the grid points where observations are available take part in the computation).

Variable	Unit	winter (DJF)	spring (MAM)	summer (JJA)	autumn (SON)
tas	K	0.23	0.13	0.12	0.09
tasmin	K	0.24	0.16	0.13	0.11
tasmax	K	0.22	0.14	0.17	0.12
pr_amount	mm day ⁻¹	0.137	0.224	0.265	0.151
rsds	W m ⁻²	1.89	3.11	3.06	1.36
hfls_o	W m ⁻²	1.26	1.01	0.79	0.99
hfls_l	W m ⁻²	0.62	1.35	2.69	1.16
sfcWind/ws	m s ⁻¹	0.048	0.058	0.05	0.035
psl	hPa	0.185	0.189	0.141	0.099
clt	%	0.926	1.201	1.009	0.673

3.2 Parameter testing for ICON in Climate Mode

During the parameter testing phase (stage 2 of the RCM tuning strategy, see loop 2b-2e in Fig. 1), we divided all model runs into two groups: Table 5 and Table 6 provide an overview of the parameter changes tested and how the change signals, i.e., the impacts of the parameter adjustments or changes, were calculated. In this section, we investigate these signals for those model quantities, i.e., model outputs, that show the largest sensitivity to parameter changes. The first group consists mainly of the external input data sets and parameters related to the configurations of the soil and vegetation, cloud, and convection parameterisations (see Table 5) used for the definition of the new reference. In the second group, we tested the sensitivity of disturbed values of continuous parameters (Table 6) for later use in either the expert tuning mode or the LiMMo optimisation (see Sect. 3.4).

Table 5. Parameters tested for the definition of a new reference, the selection is based on expert knowledge. ‘reference values’ indicate the settings of the reference experiment. The meaning of the abbreviated parameter values marked with an asterisk ‘*’ is explained in Table A2. The ‘signal’ column denotes the two simulation IDs (without ‘C2I’ prefix) that are used to estimate the impact of parameter changes. These IDs are documented in Table C1. Parameters in a ‘typewriter’ font are ICON namelist parameters, and parameters in ‘**bold**’ correspond to multiple parameters changed simultaneously.

name of parameter (-set)	reference value	test value	signal
lterra_urb	.false.	.true.	103 – 101
AEROSOL	Tegen*	MACv2-SP*	105 – 101
ecrad_llw_cloud_scat	.false.	.true.	107 – 101
GSCP	1-ice*	2-ice*	108 – 101
czbot_w_so	2.5	4.5	127 – 128
lsgs_cond	.true.	.false.	109 – 101
DT_PHY	dt1*	dt2*	110 – 101
lstoch_sde	.false.	.true.	114 – 101
inwp_cldcover	1	3	117 – 109
itype_z0	2	3	122 – 101
zml_soil	zml1*	zml2*	128 – 101
itype_hydmmod	0	1	129 – 101
CLOUD-PAR	cloud1*	cloud2*	130 – 101
SOIL-DATA	FAO*	HWSD v2.0*	232 – 230
AEROSOL-CLOUD-FB	ac-fb0*	ac-fb1*	241 – 240
ORO+TUNING	GLOBE*	MERIT*	206 – 200

Table 6. As Table 5, but for parameters tested during the sensitivity study. Values marked with ‘*’ are explained in Table A2. The parametrisation of `allow_overcast` (ao, aoa, aoac) is explained in Eq. 3.

	ref value	test value	signal
<code>start date</code>	1979/01	1978/12	207 – 200
<code>tune_box_liq</code>	0.05	0.07	203 – 200
<code>tune_box_liq_asy</code>	3.25	4.00	202 – 200
ALLOW_OVERCAST-PAR (ao, aoa, aoac)	(1.0,-,-)	(0.9,-,-)	222c – 208c
ALLOW_OVERCAST-PAR(m) (ao, aoa, aoac)	(0.9,-,-)	(0.9,1.0,aoac*)	285c – 284c
<code>tkhmin, tkmmin</code>	0.6, 0.75	0.30, 0.375	235 – 230
<code>rat_sea</code>	0.70	0.40	214c – 217c
<code>rlam_heat</code>	10.00	6.25	205 – 200
<code>rat_lam</code>	1.00	0.80	220c – 217c + 208c – 200c
<code>cr_bsmin</code>	110	150	204 – 200
<code>tune_albedo_wso(1)</code>	0.00	0.10	$0.5 \cdot (287c + 289c) - 290c$
<code>tune_albedo_wso(2)</code>	0.00	-0.10	287c – 289c
<code>rsmin_fac</code>	1.00	1.20	286c – 285c

520 To systematically assess the impact of parameter changes on model quantities, we present the sensitivity measure values (see Eq. 13 in Sect. 2.6.2) for the winter and summer seasons in Fig. 2. The sensitivity tables show the sensitivities of the main surface model quantities (see Table 2) with respect to the modifications of the model parameters given in Table 5 and Table 6. The parameters corresponding to the update of external datasets are shown separately in the upper panels of Fig. 2 as they are used for scientific reasons despite their sensitivity values.

525 We found no significant sensitivity in winter or summer for the following parameters: `lterra_urb`, **AEROSOL-CLOUD-FB**, `ecrad_llw_cloud_scatter`, `czbot_w_so`, `lsgs_cond`, `zml_soil`, `cr_bsmin`, `tune_albedo_wso(2)`, and `rsmin_fac`. Hence, we only discuss these parameters briefly and classify them as ‘not sensitive parameters’. The remaining parameters tested exhibit a sensitivity around twice the intrinsic variability or larger, especially during the summer, and are classified as ‘sensitive parameters’.

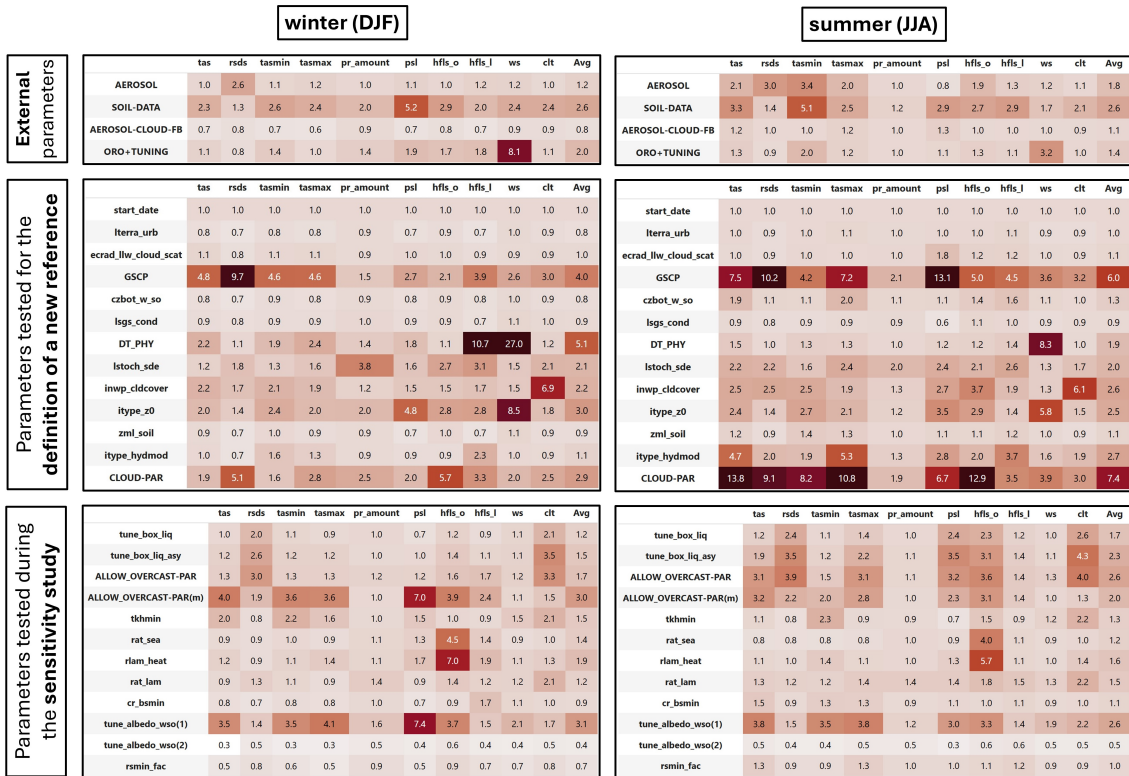


Figure 2. Mean seasonal sensitivities of the ICON-CLM to changes in tested parameters. In each table, the rows represent the model parameters and the columns the model quantities, where the last column ‘Avg’ gives the average value. The tables on the left show the sensitivity values for the winter (DJF) season. The tables on the right show the sensitivity values for the summer (JJA) season. Sensitivities are shown for the external parameters (top row, see Table 5), for parameters tested for the definition of a new reference (centre row, see Table 5), and for the parameters tested during the sensitivity study (bottom row, see Table 6). The sensitivity measure is defined in Eq. 13. The intensity of the background increases with values (the same scaling for all tables).

530 For the remainder of this section, the impacts of changed sensitive parameters are systematically presented: Sect. 3.2.1 discusses the impact of changing external datasets. Sect. 3.2.2 presents parameters of surface and subsurface processes. Sect. 3.2.3 investigates the parameters controlling planetary boundary layer, mixing, and convection-related processes. Sect. 3.2.4 presents the signals for parameters of microphysics and cloud cover diagnostics.

3.2.1 External parameters

535 External parameters are static or monthly varying fields prescribed ‘externally’ to the model and describe the physical properties of the environment. We replaced data sets of lower quality and/or resolution with those of higher quality and/or resolution. In the following, we discuss the impact of the parameter modification on model results. Where the simulation quality is discussed, we use E-OBS data as an observational reference. The sensitivities of the model to changes of the external parameters in winter

and summer (see average values in Fig. 2) are large for soil type ('Avg' sens: DJF = 2.6, JJA = 2.6) and orography data ('Avg' sens: DJF = 2.0, JJA = 1.4), and minor for natural and anthropogenic aerosol ('Avg' sens: DJF = 1.2, JJA = 1.8), and aerosol-cloud-feedback ('Avg' sens: DJF = 0.8, JJA = 1.1). The summer **tasmin** is thereby the most sensitive variable. A configuration with the higher-quality external parameters is used later on as a new reference, C2I250c, for the parameter tuning.

Soil Data (test: HWSD v2.0*, reference: FAO*): For the soil type distribution sensitivity experiment, we replaced the default FAO soil dataset (Food and Agriculture Organization of the United Nations, 2003) by the Harmonised World Soil Data Base version 2.0 (HWSD v2.0; FAO and IIASA, 2023), see Fig. 3 a and b. The HWSD v2.0 data have a much smaller typical length scale (4 km to 7 km) in comparison with FAO (10 km to 50 km) and show a higher frequency of sandy loam than loam soil types (Fig. 3 c).

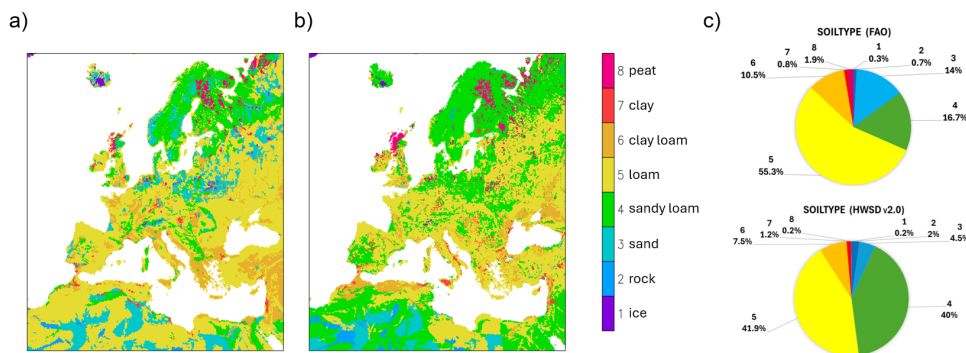


Figure 3. Default (operational) soil-type distribution based on the FAO (a) and HWSD v2.0 (b) datasets. The Pie chart (c) gives the portions of the spatial extent for soil types [in percent] shown in a and b.

Figure 4 shows the impact of the systematic shift to more 'sandy loam' soils on **tas**, **hfss**, and **hfls** in summer. Additionally, Fig. S2 gives the surface air pressure and the relation of sensible to latent heat flux (Bowen ratio). The shift increases the daily maximum temperature **tasmax** in central to eastern Europe and **tasmin** over the southern Iberian Peninsula and in northern Africa by up to 1 K. The change in **tasmin** is highly correlated with the Bowen ratio, in particular in regions with low **hfls**. The change in **tasmax** is strongly correlated with the absolute sensible heat flux **hfss**, in particular in central to eastern Europe and the Hungarian basin. Here we find a small change in the Bowen ratio since the latent heat flux is relatively high in these regions. Approximately, we find a change of temperature with forcing $dT/dF \simeq 0.1 \text{ K m}^2 \text{ W}^{-1}$.

A similar effect we found in Morocco and Algeria for soil types change from loam to loamy clay in the north. Consistently

herewith, in areas of the Mediterranean region, where loamy clay is changed to loam (Adriatic coast, Po valley, Greece, and Turkey), we found the opposite in summer: an increase of **hfls** and a decrease of Bowen ratio. Interestingly, the same effect is found in regions of a change from loamy clay to clay (Sicily). In these regions, the loamy clay holds more plant-available water than clay and loam during the summer. While clay has a high total water holding capacity, a significant portion of that water is held very tightly and is hardly available for plant transpiration. The loamy soils are already dry in summer since the water evaporated and/or drained in previous months.

A similar phenomenon can be found for the shift from sand or loam to sandy loam in the region of northern Germany, Denmark, and Poland. Here, ‘sandy loam’ exhibits the highest **hfls**.

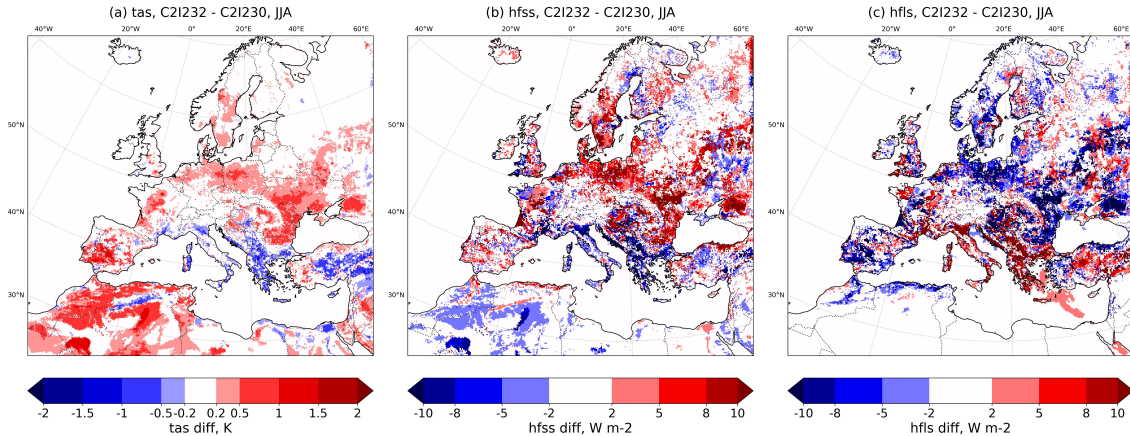


Figure 4. Sensitivity of ICON-CLM with respect to soil type distribution determined from HWSD v2.0 (test) and FAO (reference), *soil_data*. Mean differences for JJA 1980–1984 between test and reference as defined in Table 6 in column ‘signal’ for **tas** (left), **hfss** (center), and **hfls** (right).

Orography data and related model tuning (test: MERIT*, reference: GLOBE*): Using the updated model orography data set is accompanied by applying a set of revised tuning parameters for the sub-grid scale orography scheme (see settings of C2I206 in Table D1). Figure 5a shows the **z0** of the GLOBE dataset based orography, while Fig. 5b indicates a strong increase in **z0** over Sweden and north-eastern Russia when using orography data based on the Multi-Error-Removed Improved Terrain Digital elevation model (MERIT). The main effect is a reduction of **sfcWind** (10m wind speed) (Fig. 6) by 0.5 m s^{-1} to 1.0 m s^{-1} on average due to a combined effect of subgrid-scale orography scheme and the direct effect of increased surface roughness, this means a reduction of the model bias compared to E-OBS (Fig. 6). The changes of subgrid slopes by using MERIT orography do not affect the **sfcWind**.

The reduction in **sfcWind** over Africa can be attributed to the adjustment of the tuning parameter values of the gravity wave and subgrid-scale orography scheme (see C2I206 and C2I200 in Table D1). As there is a lack of observational data in this area, it remains unclear whether this change represents an improvement or not.

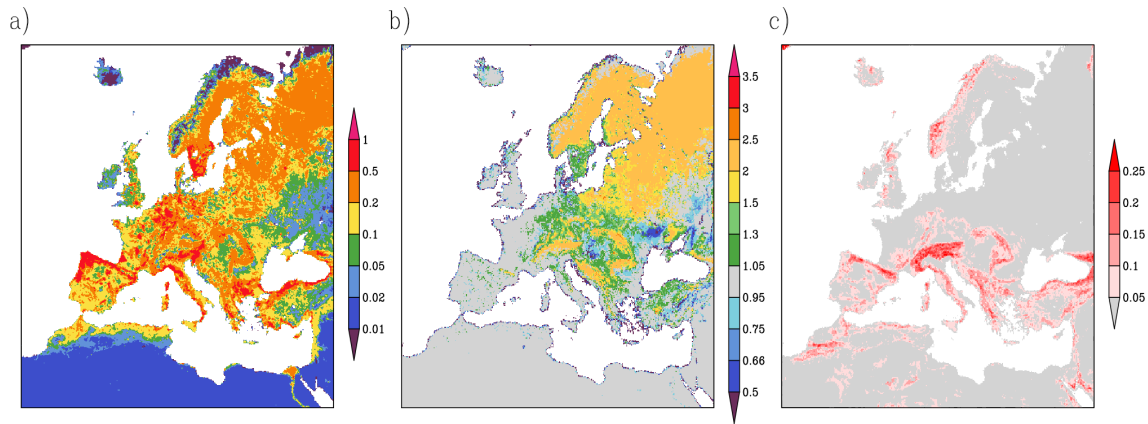


Figure 5. Surface roughness z_0 [m] of GLOBE (a), ratio between z_0 of MERIT and GLOBE (b), and deviations of subgrid slopes, where $0.1 \cong 9^\circ$ (c). White colour is used for water grid points, where z_0 is modulated by the wave height.

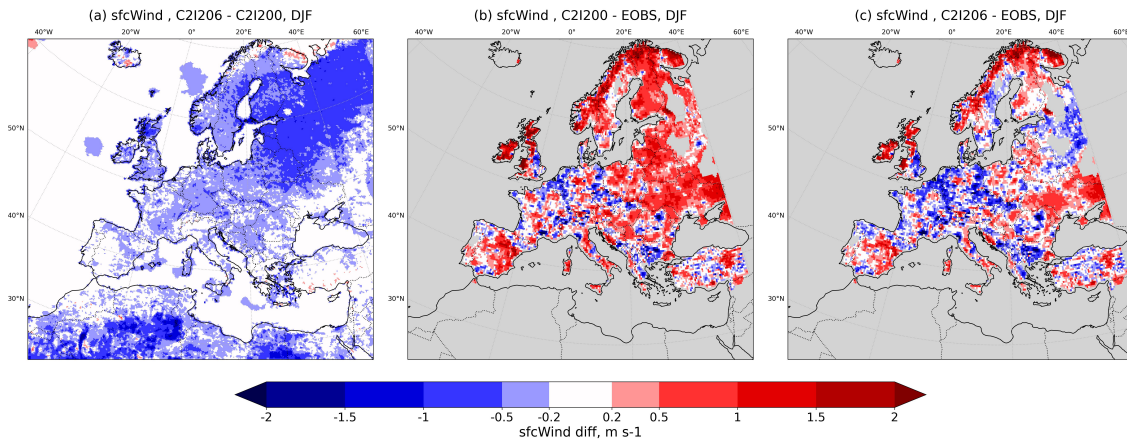


Figure 6. Sensitivity and Bias of ICON-CLM with respect to orography data from MERIT (test) and GLOBE (reference), and orography tuning. Mean differences of **sfcWind** for DJF for 1980–1984 between test and reference (a) as defined in Table 6 in column ‘signal’, reference and E-OBS (b), and test and E-OBS (c).

575 **Natural and anthropogenic transient Aerosol irad_aero (test: MACv2-SP*, reference: Tegen*):** For CMIP6-CORDEX, it is recommended (even mandatory for EURO-CORDEX, Katragkou et al., 2024) to use transient anthropogenic aerosols. Thus, as the reference experiment was set up with the standard Tegen aerosols used for NWP, which are constant in time (with a mean annual cycle), the impact of the transient aerosols prescribed by the MACv2-SP climatology was tested. The Tegen climatology is representative for the early to mid-90s, which is a period when anthropogenic emissions over Europe are already
 580 reduced compared to the 80s, for which the experiments were conducted. Thus, the transient MACv2-SP climatology contains realistically higher Aerosol optical depth (AOD) values for the 80s.

The sensitivity of the climatology for **AOD** and related meteorological quantities is largest in summer (Fig. 7). The respective sensitivity for winter is shown in Fig. S4. In summer, the differences in AOD (Fig. 7 a) are strongly correlated with **rsds** differences (Fig. 7 b). There is nearly no impact on **clt** (Fig. 7 f). AOD is increased and shortwave radiation is reduced over Europe by approximately 10 W m^{-2} . Consistently, a cooling of **tasmax** by 0.5 K is found in Europe.

In northern Africa and the eastern Mediterranean, the AOD signal is highly correlated with **rsds** but neither with **tasmin** nor with **tasmax** (Fig. 7 c and d). The latter are highly correlated with the downwelling longwave radiation **rlds** increase of 10 W m^{-2} to 20 W m^{-2} (Fig. 7 e). Increased **rlds** can partly be explained by increased cloud cover at night. However, the cloud cover difference is small and cannot be detected below 500 hPa, so the effect on thermal radiation is minor. Kinne (2019b) clearly shows a warming due to direct radiative effects of the MACv2 aerosol over northern Africa and Arabia. The explanation is that the ‘mineral dust aerosol particles in those regions are relatively large, elevated (off the ground) and absorbing’. With that, mineral dust can ‘contribute to a significant greenhouse effect’. However, it is debatable if MACv2 overestimates the increase of longwave radiation as it neglects the natural variability of mineral dust both in terms of variability of particle sizes and mineralogical composition, which can have a considerable influence (e.g. Sicard et al., 2014; Gao et al., 2026, and the references therein).

In winter, the impact of AOD on **rsds** is much weaker in Europe than in summer. A weak cooling is found in southern and eastern Europe in **tasmax** and **tasmin** (Fig. S4).

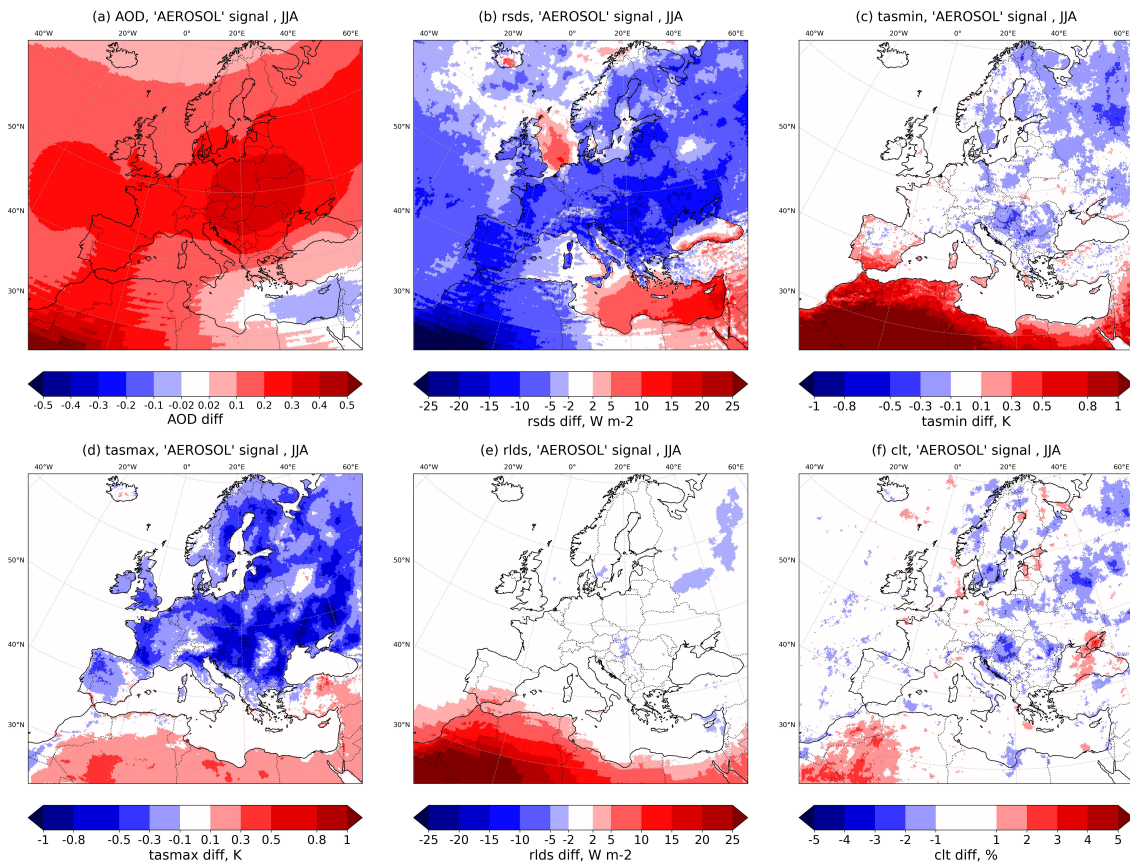


Figure 7. Mean differences (JJA 1980–1984) of Aerosol Optical Depth AOD (a), *rlds* (b), *tasmin* (c), *tasmax* (d), *rlds* (e) and *clt* (f) for the test with transient aerosol data (MACv2-SP, C2I105) minus the reference with Tegen aerosols (C2I101), cf. Table C1.

However, for the new treatment of the indirect aerosol effect (*aerosol-cloud-fb*, *icpl_aero_gscp*=3), we only found a mean sensitivity of (‘Avg’ sens: DJF = 0.8, JJA = 1.1). The values are similar for all variables. Thus, the impact is not significant.

3.2.2 Parameters of surface and subsurface processes

In this section, we discuss ICON-CLM sensitivities to parameter changes of surface and subsurface processes (see Table 5 and Table 6). Those parameters that do not exhibit a signal-to-noise ratio (i.e., sensitivity) significantly higher than one are introduced only shortly hereafter, but the results of the tests are neither shown nor further discussed.

The change of the scaling factor of minimum resistance to plant transpiration *rsmín_fac* from 1.0 to 1.2 exhibits a mean sensitivity of (‘Avg’ sens: DJF = 0.7, JJA = 1.0).

We tested the increase of bare soil minimum resistance to turbulent fluxes `cr_bsm` in (C2I111–C2I200) from 110 to 150 s m^{-1} . The results are similar to those found for `rsmin_fac` increase and exhibit a mean sensitivity of (‘Avg’ sens: DJF = 0.9, JJA = 1.1).

610 The factor `rat_lam` is scaling the resistance to turbulent latent heat flux over land in comparison with that over ocean surfaces. For the change from 1.0 to 0.8, we found a sensitivity for `clt` of (‘clt’ sens: DJF = 2.1, JJA = 2.2) and (‘Avg’ sens: DJF = 1.2, JJA = 1.5). Due to the definition of the signal as a linear combination of four simulations (see Table 6), the noise level is twice the noise level used for the definition of the sensitivity in Table 4. Considering the higher noise level of `rat_lam` test results, the results can be regarded as not significant.

615 **itype_z0 (test:3, reference:2):** A change of the parameter value for `itype_z0` from 2 to 3 results in an increase of surface roughness `z0` in mountainous regions. For `itype_z0=2`, `z0` is determined from land-cover-related roughness considering tile-specific land use class. For `itype_z0=3`, additionally, the subgrid-scale orography is considered. We found a mean sensitivity of (‘Avg’ sens: DJF = 3.0, JJA = 2.5) resulting from high sensitivities of mean sea level pressure `psl` and wind speed `ws`. The impact of the change on `tas`, `pr_amount`, and `sfcWind` is shown in Fig. 8. A systematic effect is found for
620 the wind speed, which is reduced in mountainous regions. Additionally, the effects on `psl` and the turbulent fluxes `hfls` and `hfss` are shown in Fig. S5. The impact on `psl` is up to 0.3 hPa and thus negligible. In winter, the `hfls` is increased and `hfss` is decreased slightly in mountainous regions. In summer, the `hfss` is systematically decreased by up to 10 W m^{-2} in mountainous regions in the Mediterranean while causing a decrease in `tas` by up to 0.5 K.

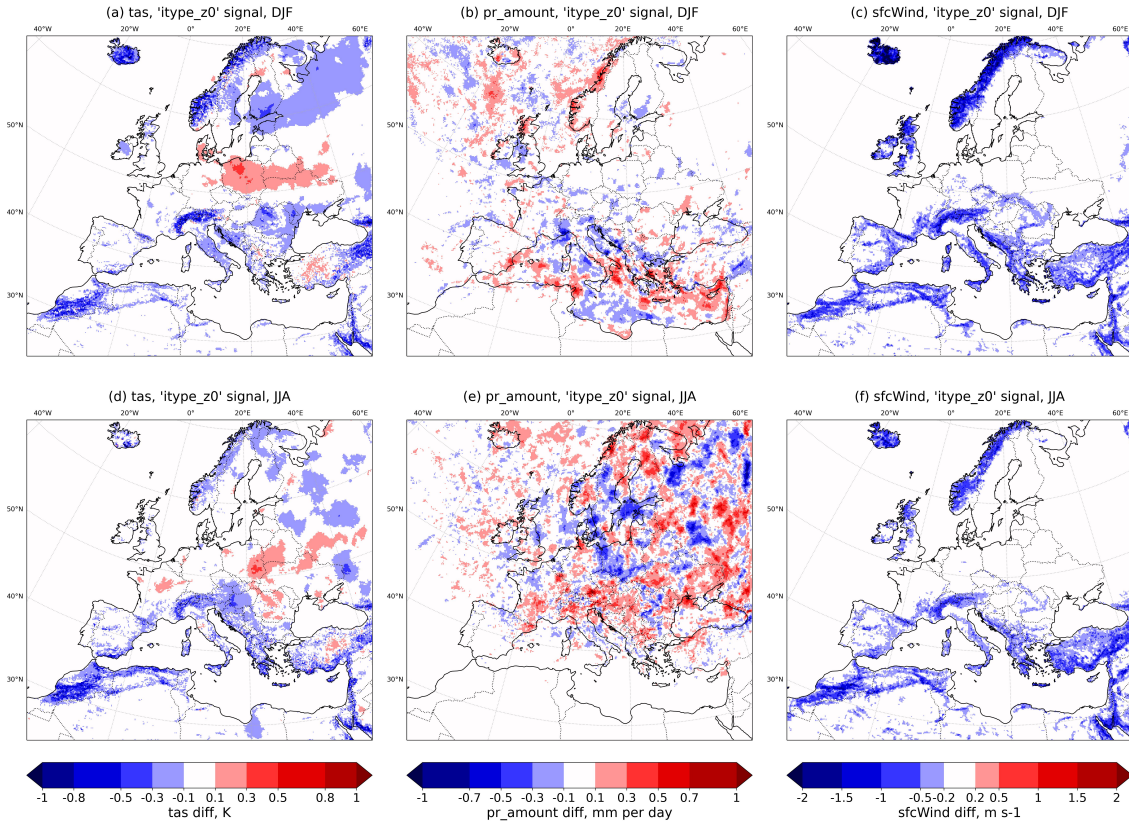


Figure 8. Mean differences (1980–1984) of **tas** (a, d), **pr_amount** (b, e), and **sfcWind** (c, f) in winter (DJF, top) and summer (JJA, bottom) for the type of roughness length data *itype_z0*.

r_{lam_heat} (test: 6.25, reference: 10): The parameter is the scaling factor of turbulent heat flux resistance at the surface (see also Table 1). For the change of the scaling factor of resistance to turbulent heat fluxes **r_{lam_heat}** from 10 to 6.25, we found a sensitivity for **hfls_o** (**‘hfls_o’** sens: DJF = 7.0, JJA = 5.7) and (**‘Avg’** sens: DJF = 1.9, JJA = 1.6) on average. The decrease of **r_{lam_heat}** leads to a strong increase of **hfls_o** over the Mediterranean Sea and the Atlantic Ocean in winter. In summer, the effect is reduced in the Atlantic but remains high in the Mediterranean Sea (Fig. 9 left).

The impact on **tas**, **pr_amount**, and **rlds** is shown in Fig. S6. We found an increase of **tas** over the entire domain by 0.3 K in winter and not in summer. This occurs, since the two effects of increased latent heat flux on the cloud cover, as later discussed in detail in Sect. 3.4.1, result in a winter increase of long wave downward radiation **rlds** due to an increase of low cloud cover. In summer, the reduction of short wave and increase in long wave are small and similar.

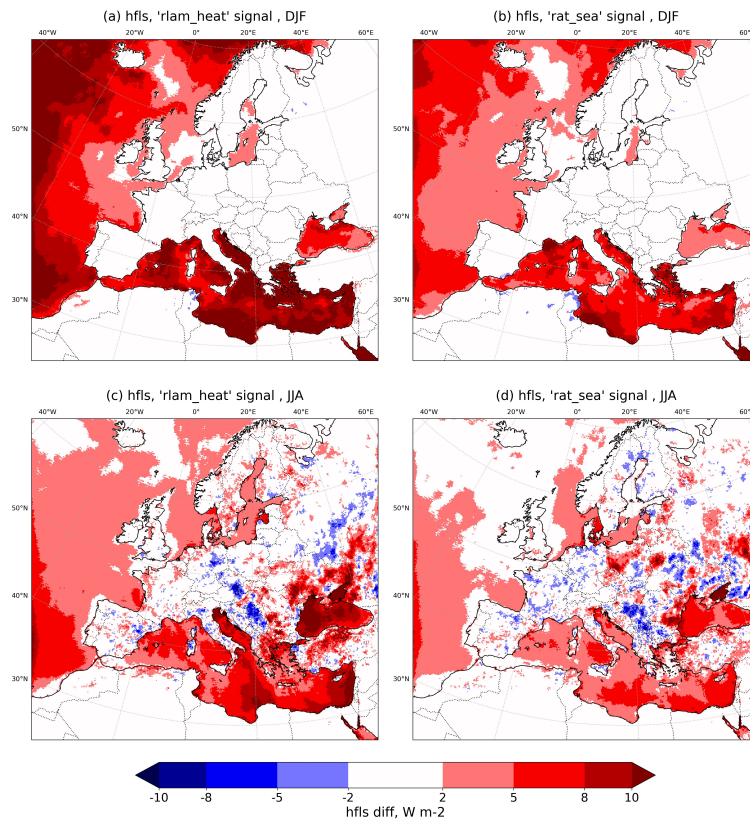


Figure 9. Mean differences (1980–1984) of **hfls** for reduced resistance to turbulent heat fluxes `rlam_heat` (left, a, c), reduced resistance to turbulent heat fluxes over water `rat_sea` (right, b, d), DJF (top), JJA (bottom).

rat_sea (test: 0.4, reference: 0.7): The scaling factor of resistance to turbulent heat fluxes over the sea surface `rat_sea` is reducing the resistance over water in comparison with land surfaces. We found high sensitivities for **hfls_o** of (`hfls_o` sens: DJF = 4.5, JJA = 4.0) and (`Avg` sens: DJF = 1.4, JJA = 1.2) on average, which is similar to `rlam_heat`. Figure 9, right, shows the impact of increased resistance on **hfls**, which is spatially very similar distributed to the effect of reduced `rlam_heat`. The impact on **tas**, **pr_amount** and **rlds** is shown in Fig. S7 as for `rlam_heat`.

tune_albedo_wso (1) and tune_albedo_wso (2) (test: 0.1/-0.1, reference: 0.0/0.0): The albedo correction, now as a modification of the official ICON release source code available (Sect. 2.2.2), for dry soils (`tune_albedo_wso (1) = 0.1`) is changing the albedo by up to 0.1 if the upper soil layer is dry. For **tas** we found a sensitivity of (`tas` sens: DJF = 3.5, JJA = 3.8) and of (`Avg` sens: DJF = 3.1, JJA = 2.6) on average. Figure 10 shows a decrease of **tasmin**, **tasmax** in summer of 0.5 K to 1.5 K in the Mediterranean due to an increase of short wave outgoing radiation flux at the surface **rsus** of 10 W m⁻² to 20 W m⁻². Additionally, Fig. S8 shows a slight decrease of **pr_amount** and **hfls** in JJA in central to northern Europe due to increased **rsus**, which is an indirect effect.

645 The albedo correction for wet soils ($tune_albedo_wso(2) = -0.1$) is changing the albedo by up to -0.1 if the upper soil layer is wet. It exhibits a very weakly significant impact on the reflected solar radiation in the southern part of the domain in summer and no significant impact on the other surface energy budget components, nor on **tas**.

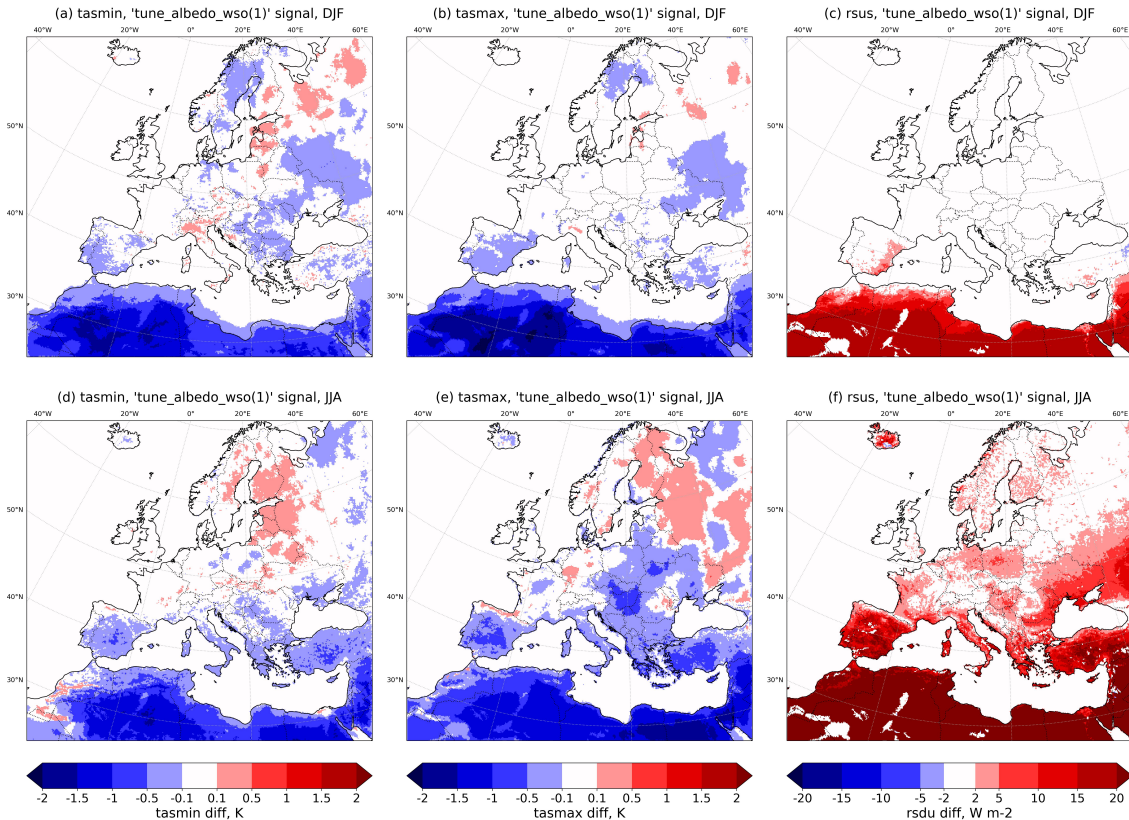


Figure 10. As Fig. 8 but for **tasmin**, **tasmax** and **rsus** and increased albedo for dry soils near surface $tune_albedo_wso(1)$.

itype_hydmmod (test: 1, reference: 0): The new parameterisation of horizontal transport of subsurface water due to gravitation $itype_hydmmod=1$ shows high sensitivities for summer **tasmax** ('tasmax' sens: DJF = 1.3, JJA = 5.3), for latent
650 heat flux over land **hfls_1** and ('hfls_1' sens: DJF = 2.3, JJA = 3.7) and ('Avg' sens: DJF = 1.2, JJA = 2.7) on average. The impact on **tas**, **pr_amount** and **hfls** is shown in Fig. S9. It exhibits a warming over mountains and a cooling in water down-
flow regions due to a decrease/increase in **hfls**, e.g., in the Alpine region and the Po valley, respectively, and in particular in the dry summer season. This is consistent with the physical expectation as the lateral redistribution of water results in a changed
evaporative fraction affected by surface and subsurface heterogeneities and orography.

655 In northern Africa, there is an increase of **hfls** of 3 W m^{-2} to 5 W m^{-2} . We hypothesise that this is due to the reduced vertical gravitation flux in this parameterisation.

Unfortunately, this parameterisation was not included in the officially released model version used for configuration optimisation in this study, so it was not considered further.

3.2.3 Parameters of planetary boundary layer, mixing, and convection-related processes

660 **DT_PHY (test: dt2*, reference: dt1*)**: The frequency of calling of the convection, radiation, subgrid-scale orography drag, and gravity wave drag parameterisations might have a systematic impact on the simulation results if the time increment ΔT is too large. However, the computing time is increasing with decreasing ΔT . This test investigated the opportunity of larger ΔT values. The sensitivity found for **DT_PHY** is for **sfcWind** ('ws' sens: DJF = 27, JJA = 8.3) and ('Avg' sens: DJF = 5.1, JJA = 1.9) on average. The dependency of the solution on the time step (see Fig. S10) indicates the need for the shorter time step.
665 Consistently herewith, the analysis of the results showed that the longer time step corrupts the development of gravity waves, so the larger ΔT is not used.

tkhmin and tkmmin (test: 0.3/0.375, reference: 0.6/0.75): For the change of minimum turbulent transport coefficients for heat and momentum τ_{khmin} , τ_{kmmin} we found a sensitivity for **tasmin** of ('tasmin' sens: DJF = 2.2, JJA = 2.3) and ('Avg' sens: DJF = 1.5, JJA = 1.3) on average. Reducing the minimum vertical transport reduces the mixing in a stable atmosphere.
670 Stable conditions occur particularly in winter and at night. This reduces the sensible heat flux at the surface, thereby increasing cooling during the night. In cloudy conditions, it helps to dissolve the low cloud cover, which exists over too long time spans otherwise.

Figure S11 shows the impact of the reduction of the parameter values on **tasmin**, **hfss**, and **clt**. We find a reduction to **tasmin** by 1 K in winter and 0.5 in summer, and no significant impact on precipitation. In winter, the downward positive sensible heat
675 flux **hfss** is reduced by 2 W m^{-2} in stable stratification, in particular in snow-covered regions and in the desert. In summer, this effect is weaker. The cloud cover and the longwave downward radiation are slightly increased, but do not have a dominant impact on the near-surface temperature. However, the overall effect decreases the simulation quality, and thus, these parameter value changes have not been considered in the new reference, and they are not used as optimisation parameters.

lstoch_sde (test: 1, reference: 0): The stochastic shallow convection scheme (`lstoch_sde=.true.`) aims at pa-
680 rameterising the shallow convection in simulations resolving deep convection, i.e., at horizontal grid sizes smaller than 20 km. It has to be used together with setting both `lrestune_off` and `lmflimiter_off` to 'True'. The parameter sensitivity for **pr_amount** of ('pr_amount' sens: DJF = 3.8, JJA = 2.0), for **hfls_l** of ('hfls_l' sens: DJF = 3.1, JJA = 2.6) and ('Avg' sens: DJF = 2.1, JJA = 2.0) on average.

Figure 11 shows the impact on **tas**, **pr_amount**, and **rsds**. The **pr_amount** in winter is strongly decreased due to flow
685 disturbances at the inflow boundary, at coastlines, and at some of the mountain chains, in particular when the wind speeds are high. The precipitation is increased inland, indicating a potentially strong relation to sea breeze circulations. In summer, mainly the mountainous **pr_amount** is increased by enhanced shallow convection. Herewith, **rsds** is consistently reduced by 5 W m^{-2} to 10 W m^{-2} over large parts of the domain in summer.

An unexpected effect is the reduction in **tas** in the north-east of the domain. A more detailed inspection revealed a reduction
690 of **rlds** due to increased mixing.

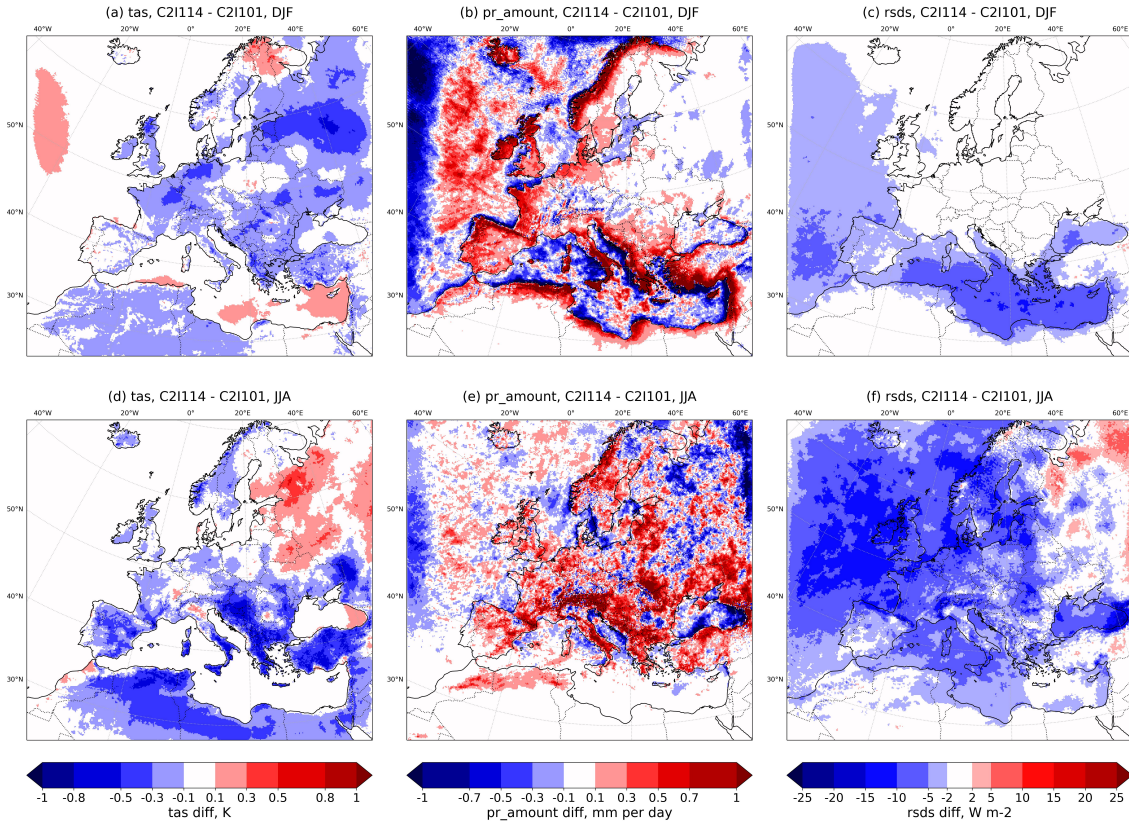


Figure 11. As Fig. 8 but for **tas**, **pr_amount**, and **rsds** and for the application of the stochastic shallow convection scheme (`lstoch_sde=.true.`).

3.2.4 Parameters of microphysics and cloud cover diagnostic

The parameterisations of precipitation and cloud cover diagnostics described in Sect. 2.2.1 have a direct impact on the irradiance at the surface **rsds** and **rlds**. The most important ICON parameters are considered in this study.

Grid Scale Precipitation (GSCP) (test: 2-ice*, reference: 1-ice*): The 1-moment scheme (mass; `inwp_gscp=1`) with two categories of ice (cloud ice, snow) is tested with new ice nucleation (`inwp_gscp=3`). We tested it together with recommended configuration settings (see C2I108 in Table C1). Overall, we found high sensitivity on `inwp_gscp` change (‘Avg’ sens: DJF = 4.0, JJA = 6.0) and especially high values for **rsds** (‘rsds’ sens: DJF = 9.7, JJA = 10.2).

As shown in Fig. S12, the new ice nucleation generates much higher **pr_amount** at the eastern outflow boundary and in mountainous regions in summer. The strong increase in **rsds** values in winter in the Mediterranean (up to 15 W m^{-2}) and over the North Atlantic and northern Europe (up to 40 W m^{-2}) in winter leads to an increase in **tas** of up to 0.8 K in winter and 1 K in summer in the corresponding regions. Additionally, we found a distinct reduction of **tas** in the north-eastern part of the domain in winter, where the **pr_amount** is not systematically influenced. This indicates an increase in cloud base height,

resulting in reduced **rlds**. Due to the reduction of the overall simulation quality, the scheme tested is not used in the new 12 km grid reference (see also Fig. 15).

705 **inwp_cldcover** (test: 1, reference: 3): The subgrid-scale cloud cover scheme is a parameterisation of the cloud cover due to vertical mixing processes (convection, turbulence) if the **rh** is below 100%. Here, the impact of the scheme, already available in the COSMO model (`inwp_cldcover=3`), is investigated in comparison with the reference (`inwp_cldcover=1`) cloud cover diagnostics. The latter is used in the radiation scheme and has no direct impact on precipitation. We found a sensitivity for **clt** of ('clt' sens: DJF = 6.9, JJA = 6.1) and ('Avg' sens: DJF = 2.2, JJA = 2.6) on average.

710 The impact on **tas**, **rsds**, and **rlds** is shown in Fig. 12. We found a **rsds** change of -3 W m^{-2} and -5 W m^{-2} in winter and summer, respectively, due to increased cloud cover, together with an **rlds** increase of up to 10 W m^{-2} and 6 W m^{-2} in winter and summer, respectively. This resulted in an increase in radiative forcing and an increase in **tas** over North Europe by up to 1 K in winter and over land in summer by approximately 0.3 K.

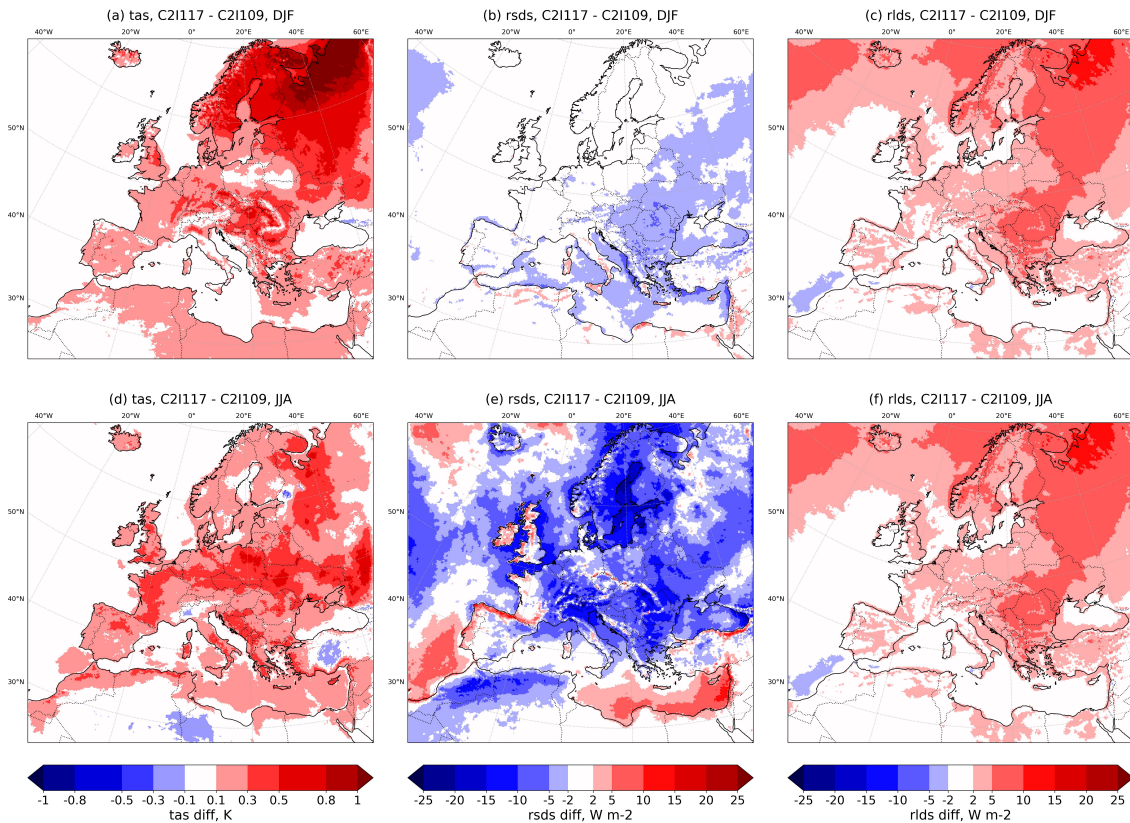


Figure 12. As Fig. 8 but for `inwp_cldcover=3` and for **tas** (a, d), **rsds** (b, e), and **rlds** (c, f).

The results in radiation components show an increase in **clt** and a reduction of the cloud bottom height, in particular in winter, and the relevance of the diagnostic cloud cover for tuning of the surface forcing.

The process-specific subgrid-scale cloud cover diagnostics and their tuning parameters (`allow_overcast`, `tune_box_liq`, `tune_box_liq_asy` and others, see Sect. 2.2.1), were introduced for the new scheme in ICON (`inwp_cldcover=1`); they are not available for the old scheme from the COSMO model (`inwp_cldcover=3`). This study, therefore, uses the latest tuning options of the new subgrid-scale cloud cover scheme.

720 **allow_overcast** (**test:** 0.9, **reference:** 1.0): The shape factor `allow_overcast` of the quadratic dependence of subgrid-scale cloud cover on **rh** is a parameter of the cloud cover scheme `itype_cldcover=1`. We found a sensitivity for **clt** of ('clt' sens: DJF = 3.3, JJA = 4.0) and ('Avg' sens: DJF = 1.7, JJA = 2.6) on average.

As mentioned in Sect. 2.2.3, smaller values of `allow_overcast` result in higher subgrid-scale cloud cover. Figure 13 shows the sensitivity of reducing `allow_overcast` from 1.0 to 0.9.

725 Figure 13 c and f show an increase of total cloud cover, in particular in summer and over the sea, where the cloudiness is mainly partial. During winter, a decrease in **rsds** (Fig. S13) is found over land in central and southern Europe, and an increase of 3 W m^{-2} in downward longwave radiation over northern and central Europe, which results in an increase of up to 0.5 K in **tas** in snow-covered regions.

While over the Mediterranean and southern Europe, the radiative forcing effect is close to zero, over northern Europe, the 730 daily mean **tas** (Fig. 13) is increased by up to 0.5 K and **tasmin** by up to 1 K. During winter, the sunshine duration is short in northern Europe. Consequently, the prevailing effect is an increase in the long-wave radiation absorbed by the surface (see Fig. S13).

The increase in **clt** can be explained by frequent cyclonic synoptic situations leading to overcast (total cloud cover of 1). In these situations, a reduction of `allow_overcast` can lead to an increase of **clt** at additional model levels, in particular 735 for low clouds, reducing the bottom cloud height and making the existing cloudy layer optically more opaque. However, it can not lead to an increase in the **clt** greater than 1. This argument may explain the low sensitivity of the **clt** to the change in `allow_overcast` in northern Europe in winter, an increase of **rlds**, and a strong increase of **tas**, in particular in snow-covered regions.

Figure 13 shows that the increase in **clt** in summer is much higher than in winter, resulting in a **rsds** reduction of 20 W m^{-2} 740 in summer and of 10 W m^{-2} in winter and over the entire northern part of the domain and in relatively small changes in **rlds** (see Fig. S13). Figure 13 d consistently shows a reduction in **tas** of about 0.3 K to 0.5 K in particular during the day. This is shown by the reduction of **tasmax** of up to 1 K.

An inflow boundary effect can be found in **pr_amount** in winter and summer (Fig. 13 b and e). Since the cloud cover diagnostics are not used in the microphysics scheme, this effect is probably caused by a feedback of reduced reflected shortwave 745 radiation on precipitable water.

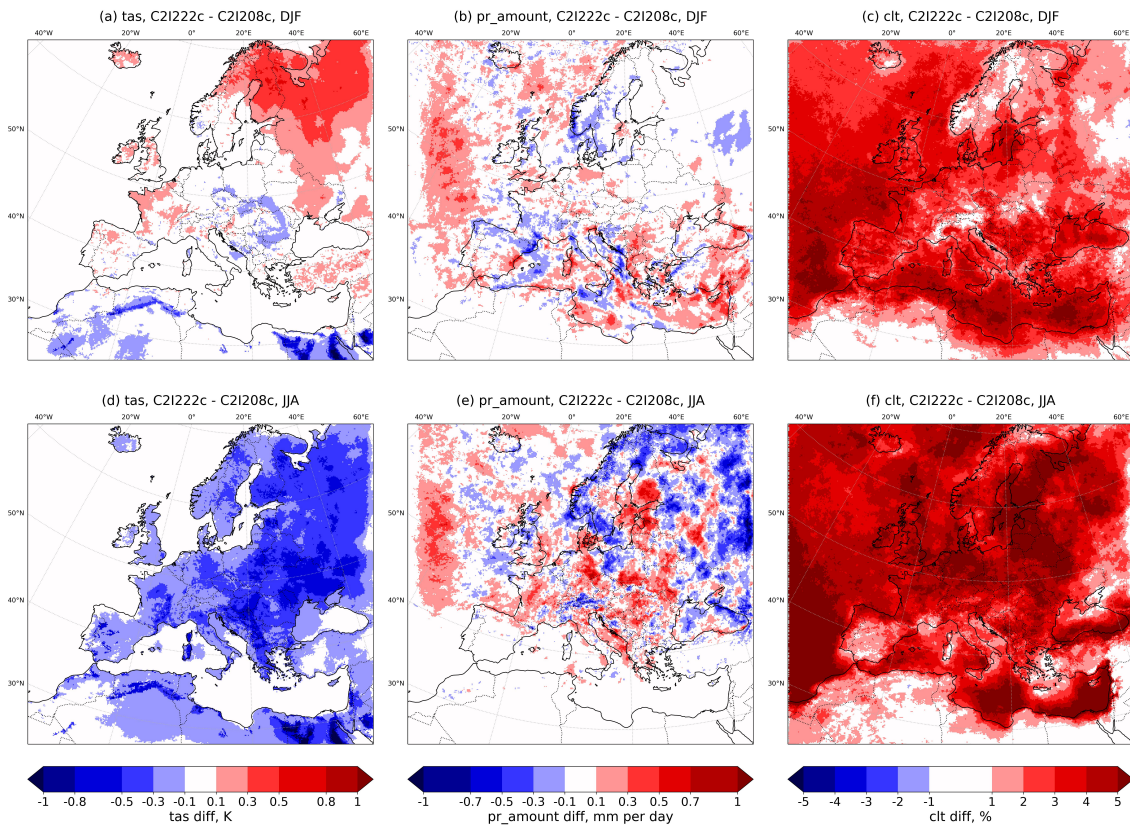


Figure 13. As Fig. 8 but for reduced `allow_overcast` and `tas` (a, d, left), `pr_amount` (b, e, center) and `clt` (c, f, right).

`tune_box_liq` (test: 0.07, reference: 0.05): The increase of the range of relative humidity `tune_box_liq` around 100% from 0.05 to 0.07, within which the cloud cover is increasing from 0 to 1 (see Eq. 2), exhibits the highest sensitivity for `clt` (DJF = 2.1, JJA = 2.6). The mean sensitivities ‘Avg’ are (DJF = 1.2, JJA = 1.7). This increases the subgrid-scale cloud cover and reduces `rsds`.

750 The effect of increasing `tune_box_liq` is very similar to that of reducing `allow_overcast` to 0.9 but weaker, in particular in summer. While the effect of reducing `allow_overcast` is reflected in the appearance of full overcast areas, strongly influencing insolation, the effect of increasing `tune_box_liq` is reflected in a slight increase of partial cloudiness areas (see Fig. 14 c and Fig. 13 f) with a weaker effect on insolation and thus on `tas` (see Fig. 14 a and Fig. 13 d). For comparison, Fig. S14 shows `tasmax`, `rsds` and `rlds` in winter and summer.

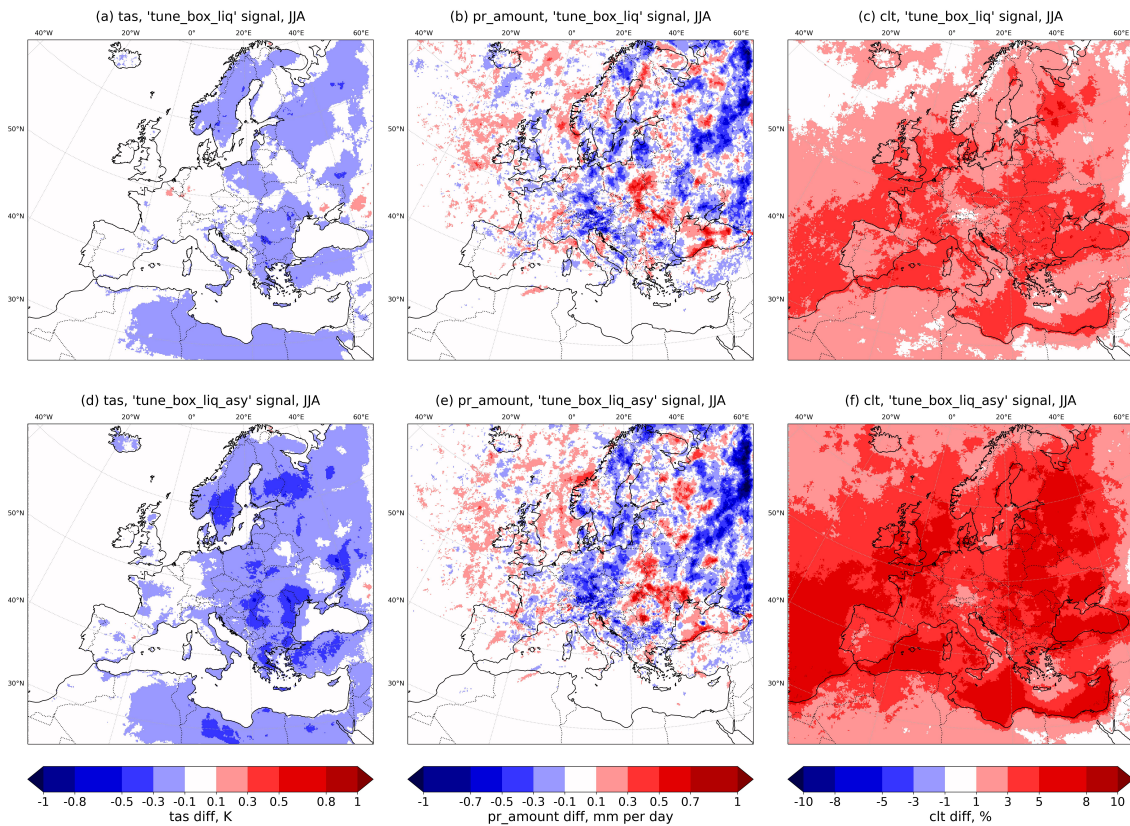


Figure 14. As Fig. 13 but for reduced `tune_box_liq` (top) and increased `tune_box_liq_asy` (bottom) and JJA only.

755 **`tune_box_liq_asy` (test: 4.0, reference: 3.25):** For the scaling factor determining the asymmetry term of the cloud cover for over- and undersaturation `tune_box_liq_asy`, we found a sensitivity for `clt` of ('`clt`' sens: DJF = 3.5, JJA = 4.3) and ('`Avg`' sens: DJF = 1.5, JJA = 2.3) on average.

The effect of increasing `tune_box_liq_asy` is very similar to that of reducing `allow_overcast` and increasing `tune_box_liq`. There is an increase in `clt` (see Fig. 14) and a reduction of `rsds` (see Fig. S15, center). As expected (see
 760 Sect. 2.2.3), the effect of increasing `tune_box_liq_asy` is stronger than the effect of increasing `tune_box_liq`, leading to a larger increase of partial cloudiness. The comparison of the results shown in Fig. 13, Fig. S13, Fig. 14, and Fig. S15 show that the effects of decreasing `allow_overcast` and increasing `tune_box_liq_asy` are of similar magnitude in `tas`, `rsds` and `rlds`. However, the spatial structures are different and accumulate to significantly different patterns in `tas`, `tasmax` and `tasmin`.

765 3.3 New reference configurations, their quality and the inferred tuning aim

The original reference configuration (C2I101) has been further developed based on a series of test simulations of parameter settings used in climate mode of the COSMO model, of new external parameters, and of the ICON model developments

described in Sect. 3.2. The new expert decision based reference configuration is used in the C2I200 and C2I200c simulations and is given in Table D1.

770 Figure 15 summarises the evaluation results for each parameter tested (see Table 5) in terms of the index ScoPi for the PRUDENCE regions (RCM tuning strategy stage 2, step 2d). It shows that, in particular, the parameter change of AEROSOL-SP (C2I105), of parameter lstoch_sde (C2I114) and of inwp_cldcover (C2I117) improve the model quality.

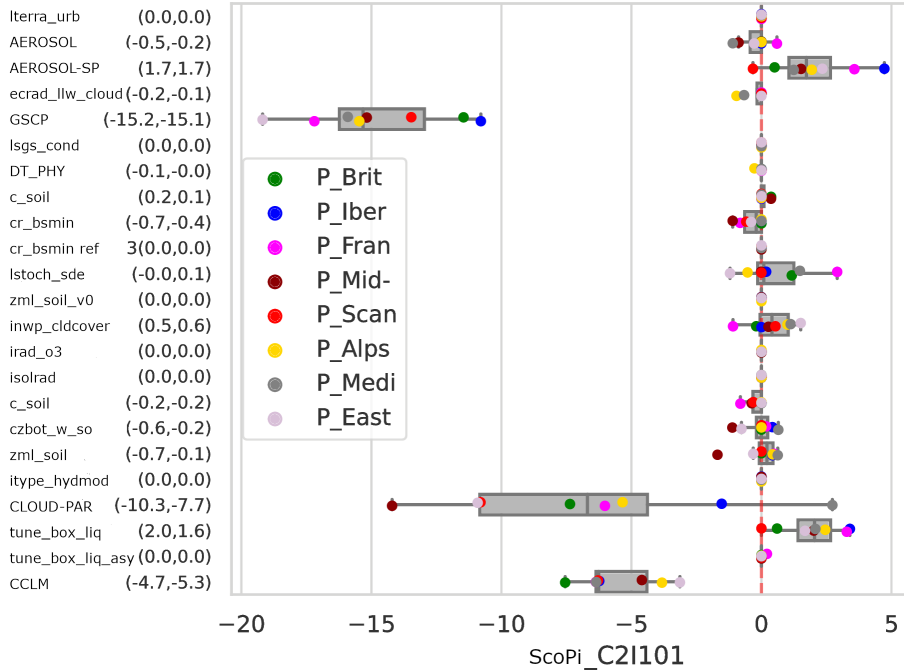


Figure 15. ScoPi_{region} based on the differences in the mean BIAS of all variables in Table 2 between the observations and each simulation of Table C1, against the ones of the reference simulation C2I101. The colours indicate the eight PRUDENCE analysis regions. The numbers given on the y-axis labels in brackets are the ScoPi_{simulation}. The values represent the averages over all eight PRUDENCE regions, weighted by the distance to Mid-Europe, one of the main areas of interest (first value), and by their area (second value), respectively (see Table 3). Higher ScoPi values mean that the test simulation is more consistent with the selected observations than the reference simulation.

The expert decision to use a test parameter value in the new reference is based on scientific arguments (Fig. 1, 2g). Here is a breakdown of some decisions for the new intermediate reference configuration C2I200, as a basis for further tuning:

775 The urban parameterisation (lterra_urb) is not used since the evaluation data used do not consider the urban effect. The new aerosol climatology MACv2-SP is used since it exhibits highly positive ScoPi, and the quality of the data has been shown independently to be higher than for the Tegen aerosol data. The parameterisation of long-wave radiation scattering by clouds (ecrad_llw_cloud_scat) shows no impact on the results and is not used. The enhanced precipitation scheme by two ice phases is not used since it increases the computing time by 30% and shows highly negative ScoPi. A higher

780 depth of hydrologically active soil (czbot_w_so) is used since it is well tested in climate mode in the COSMO model,

preventing extremely low summer latent heat flux, and shows neutral ScoPi results. The subgrid-scale condensational heating in the atmosphere due to the non-convective part of diagnosed cloud water (`lsgs_cond`) is not used since the sensitivity is low. Lower frequency of execution of convection, radiation, SSO, and gravity wave drag parameterisation is rejected since it negatively affects some results significantly. The stochastic differential equation for subgrid scale cloud cover (`lstoch_sde`)
785 is not used since it does not result in a positive ScoPi score. The COSMO sub-grid scale cloud scheme does not show significant improvements (`inwp_cldcover`) and is not used. The same applies to the consideration of subgrid scale orography in the roughness length (`itype_z0`). The distribution of soil layers (`zml_soil`) using 10 instead of 8 soil layers is used since it is well tested in the climate mode with the COSMO model and does not show a negative impact on the ICON results. The parameterisation of horizontal subsurface water fluxes (`itype_hydm0d`) shows a significant impact on **tas** in a physically
790 reasonable way, but it is not used since the parameterisation is not available in the released ICON model version. The new cloud cover diagnostics parameters exhibit negative ScoPi and are not used in the new reference. They are tuned independently by expert analysis and LiMMo tuning. These scientific arguments are resulting in a new reference configuration evaluated as C2I200c.

In addition to the parameters considered in C2I200c, further new external parameters have been investigated and considered
795 in the second new reference configuration C2I250c introduced by expert decision: The HWSD v2.0 soil data have a higher spatial resolution than the previously used FAO data and are regarded as having a higher quality over Europe. They are less sandy, and using them reduces the summer cold bias. The usage of MODIS cloud condensation nuclei number allows the consideration of the aerosol-cloud feedback in the ICON model. The higher-resolution MERIT orography increases the surface roughness in North-East Europe. Together with the corresponding parameter tuning, it reduces the positive wind speed bias in
800 this region.

In the following, we discuss the quality of the evaluation simulation C2I200c and define a model tuning aim addressed by expert and LiMMo tuning. The quality problems found in the evaluation simulation C2I250c are similar, and they are not shown additionally.

Figure 16 shows the quality of the reference simulation C2I200c. From winter to summer, we found a pronounced negative
805 bias for **tas** and a positive one for **rsds**, which are contradictory signals, and this complicates the expert tuning. The precipitation biases are small, except for spring, where dry biases dominate the eastern half of the domain and for some coastal regions, where wet biases are found.

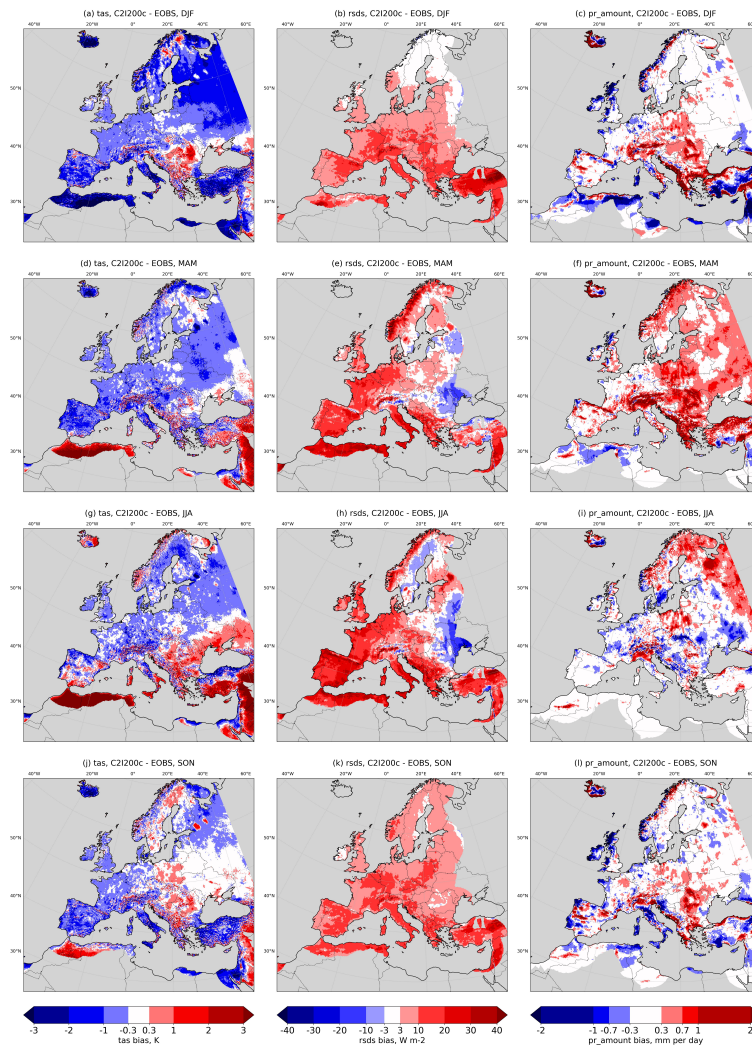


Figure 16. Mean seasonal biases (2003–2008) of **tas** (left), **rsds** (centre), **pr_amount** (right) for revised reference configuration C2I200c compared to E-OBS data for DJF (top), MAM (2nd row), JJA (3rd row), and SON (bottom).

Figure 17 shows a detailed analysis of **pr_amount** in comparison with station observations for Germany and Poland. The annual cycle (Fig. 17a) exhibits an overestimation of around 10 % and 15 %, respectively, for most of the months. The mean diurnal cycle (Fig. 17c) shows a strong overestimation of the late night to noon precipitation and a too early precipitation maximum. In Germany, the morning minimum is not simulated at all. The histogram shown in Fig. 17d shows an overestimation of low (< 2 mm h⁻¹) and underestimation of high to extreme events. The annual cycle of **rsds** in Germany and Poland confirms the positive bias already found in the comparison with E-OBS data (Fig. 17 b).

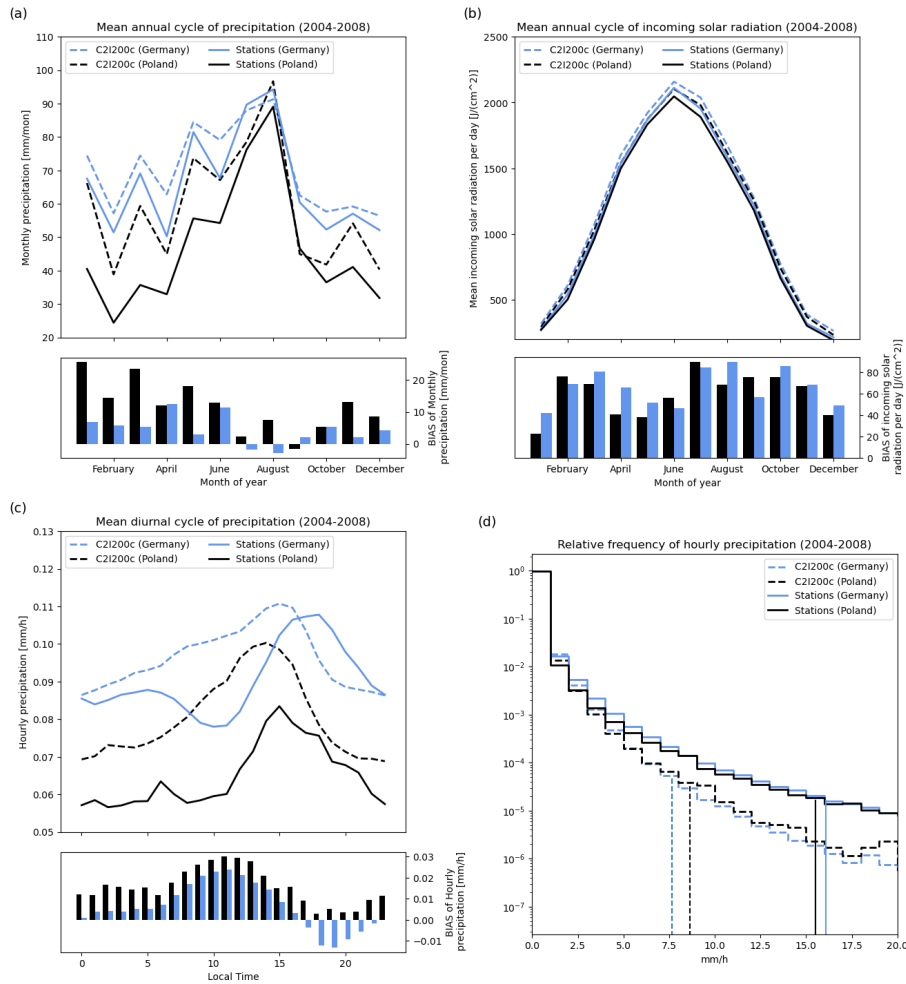


Figure 17. Annual cycle of **pr_amount** and **rsds** (2004–2008) for C2I200c in comparison to station data in Germany and Poland station data (top), diurnal cycle of **pr_amount** (bottom, left), and relative frequency distribution of hourly precipitation (bottom, right). Vertical lines denote the 99.99th percentile. The number of stations for **rsds** is 23 for Poland and 34 for Germany; for **pr_amount** it is 54 for Poland and 1009 for Germany.

The comparison of latent heat flux over the ocean **hfls_o** with satellite data set HOAPS in DJF and JJA (Fig. S20) shows a strong overestimation almost everywhere in all seasons. The only exception is the eastern Mediterranean in summer, where an underestimation was found.

The results reveal that **tas** is underestimated even though the forcing, represented by **rsds**, is overestimated. Addressing these biases is regarded as a challenging and relevant first aim of tuning the 12 km configuration in the EURO-CORDEX domain.

Furthermore, the results exhibit an overestimation of the latent heat flux over water, an overestimation of coastal precipitation, in particular at inflow positions, and a nearly correct amount of seasonal precipitation over most continental regions. Reducing the overestimation of **hfls_o** without increasing the seasonal precipitation bias is identified as a second tuning aim.

A further improvement of the diurnal cycle and extreme precipitation is regarded as hardly possible at 12 km model grid resolution.

3.4 Parameter tuning

825 In Sect. 3.2, the simulation results for the external and the main tested model parameters have been discussed. In Sect. 3.3, the change of 15 parameter values in the reference configuration has been discussed, and six have been updated to be used in the new reference.

In this section, we present the results of the tuning of the remaining 12 parameters given in Table 6. We apply the commonly used method of expert tuning and, for the first time in a real climate case study, the LiMMo tuning method (Petrov et al., 2025).

830 3.4.1 Expert tuning

The task of expert tuning is to find an optimised model configuration based on the test simulation results for the tuning parameters and values given in Table 6. The procedure applied was as follows. Each expert was invited to suggest an Expert configuration. After discussion of all Expert configurations based on a comparison of the model bias, parameter sensitivities and configuration changes suggested, ten of the Expert configurations have been simulated and evaluated using the test simulation
835 and evaluation procedure. The configurations C2I266c to C2I272c given in Table 7 are five of these configurations. New Expert configurations were suggested, aiming at further optimising the best configuration found, which was C2I268c. The configurations C2I277c to C2I280c are four of the final configurations simulated and evaluated. However, the improvements found have not been significant, so that C2I268c was identified as the optimised Expert configuration. It yielded the highest ScoPi values in comparison with the reference C2I200c and did not include any extreme namelist parameter values.

840 The configuration of C2I268c is using a combination of three test simulations for individual parameters:
allow_overcast=0.9 (see Fig. 13 and Fig. S13), rlam_heat=6.25 (see Fig. S6), tune_albedo_wso= (0.1, -0.1)
(see Fig. S8). Reducing allow_overcast directly increases the low cloud cover and thus decreases the **rsds** in winter in mid to southern Europe by 3 W m^{-2} (in winter the cloud cover is already high) and in summer in northern to mid Europe by 12 W m^{-2} . It increases the incoming long wave radiation as well, in particular in northern Europe in winter by 5 W m^{-2} ,
845 resulting in a warming in northern to mid Europe in DJF by 0.3 K. In summer, the increase of cloud cover and the resulting reduction of **rsds** is dominating the reduction in **tas**. This is combined with the heat flux resistance parameter rlam_heat reduction by 30%. The latter increases **hfls** and **hfss** over water in winter and summer (see Fig. 9 a and c for **hfls**). The dominating effect is an increased low cloud cover and the associated increase of incoming long wave radiation and **tas** in the entire domain in winter (Fig. S6 c and a). In summer, the change in **rsds** and **tas** is close to zero. These two parameter changes
850 reduce **rsds** and increase **tas** in winter in northern Europe. The third important change is that of the albedo. The dry soil albedo increase is decreasing the absorption of **rsds** in the Mediterranean, in particular in summer, resulting in a summer cooling. The wet soil albedo decrease has no significant impact on the results.

Table 7. Expert Configurations. Rows – tuning parameters (see Table 6), columns – the simulation IDs without ‘C2I’ prefix (see Table D1). The ‘best’ optimised Expert configuration C2I268c is emphasised with **bold**. The settings marked with ‘*’ are given in Table A2. The missing values are equal to the corresponding values in the reference simulation C2I250c.

simulation ID parameter	250c	266c	267c	268c	271c	272c	277c	278c	279c	280c
tune_box_liq	0.05	0.07								
tune_box_liq_asy	3.25	4.0								
ao	1.0		0.9	0.9	0.9	0.9	0.9	0.9	0.9	0.9
aoac (with aoa=1.0)	-					t1*	t2*	t2*	t2*	t4*
rat_sea	0.8	0.7	0.7		0.7	0.7				
rlam_heat	10.0	5.0	5.0	6.25	6.25	5.0	6.25	6.25	6.25	6.25
rat_lam	1.0	1.2	1.2			1.2				
tune_albedo_wso(1)	0.0	0.1	0.1	0.1		0.1	0.1	0.1	0.1	0.1
tune_albedo_wso(2)	0.0	-0.1	-0.1	-0.1		-0.1	-0.1	-0.1	-0.1	-0.1
rsmin_fac	1.0							1.5	1.3	

An intercomparison of the Expert configurations given in Table 7 shows that most of the configurations C2I266c to C2I272c are using albedo tuning for dry/wet soils. The result of C2I271c was the only one not showing a clear reduction of the summer warm bias in northern Africa and the eastern Mediterranean. This justified the albedo tuning. The configuration C2I266c is the only one using tune_box_liq and tune_box_liq_asy instead of allow_overcast together with different values for other parameters than in C2I268c. These values for other parameters together with allow_overcast=0.9 can be found in C2I267c and C2I272c.

The main differences between C2I272c and C2I268c are the values for rlam_heat=5 instead of 6.25 and rat_sea=0.7 instead of 0.8. An inspection of the evaluation results for C2I268c (see Fig. S16 and Fig. S19) and C2I272c reveals very similar summer and winter tas and winter rsds biases. The rsds summer values are slightly higher in C2I272c.

The evaluation of C2I266c and C2I272c (Fig. 18) indicates a slightly smaller bias in winter rsds in C2I266c. In summer, the biases for the Iberian Peninsula and northern Africa are similar. In C2I266c, a strong decrease of rsds is found in the central to eastern part of the domain. This indicates that the increase of tune_box_liq and tune_box_liq_asy by 40% and 25%, respectively, is generating too high cloud cover in some subregions of the domain.

The results of C2I266c to C2I272c lead to the selection of C2I268c as the new reference for further expert tuning. The configurations C2I277c to C2I280c comprise different annual cycles (aoac[m]) added to the allow_overcast mean value, as well as scaling factors for latent heat flux over land rat_lam and/or for minimum plant transpiration resistance rsmin_fac. These are used to further reduce the cold bias in tasmx (see Fig. S18), the positive bias of rsds in winter and the complex positive/negative bias in summer (see Fig. S19). However, the small improvements achieved did not justify using

questionable parameter settings like the annual cycle `aoac` or strong deviations from parameter values used in operational NWP (`rsmin_fac=1.5`, `rat_lam=1.2`).

875 A final evaluation of additional model variables for the Expert configurations revealed a strong overestimation of the latent heat flux over water by `C2I268c` and by the other Expert configurations in comparison with the reference `C2I200c` (see Fig. 22).

880 The discussion demonstrates typical potential and drawbacks of expert tuning. On the one hand, it enables a definition of a new configuration by the combination of a small number of test simulation results and a small number of model variables very efficiently. On the other hand, two important drawbacks can be highlighted. First, model variables, which are not in the focus of interest, are typically neglected. Second, optimal parameter values cannot be determined, they can only be estimated. To find the optimal values, many more simulations would be necessary to consider cross-dependencies of parameterisations.

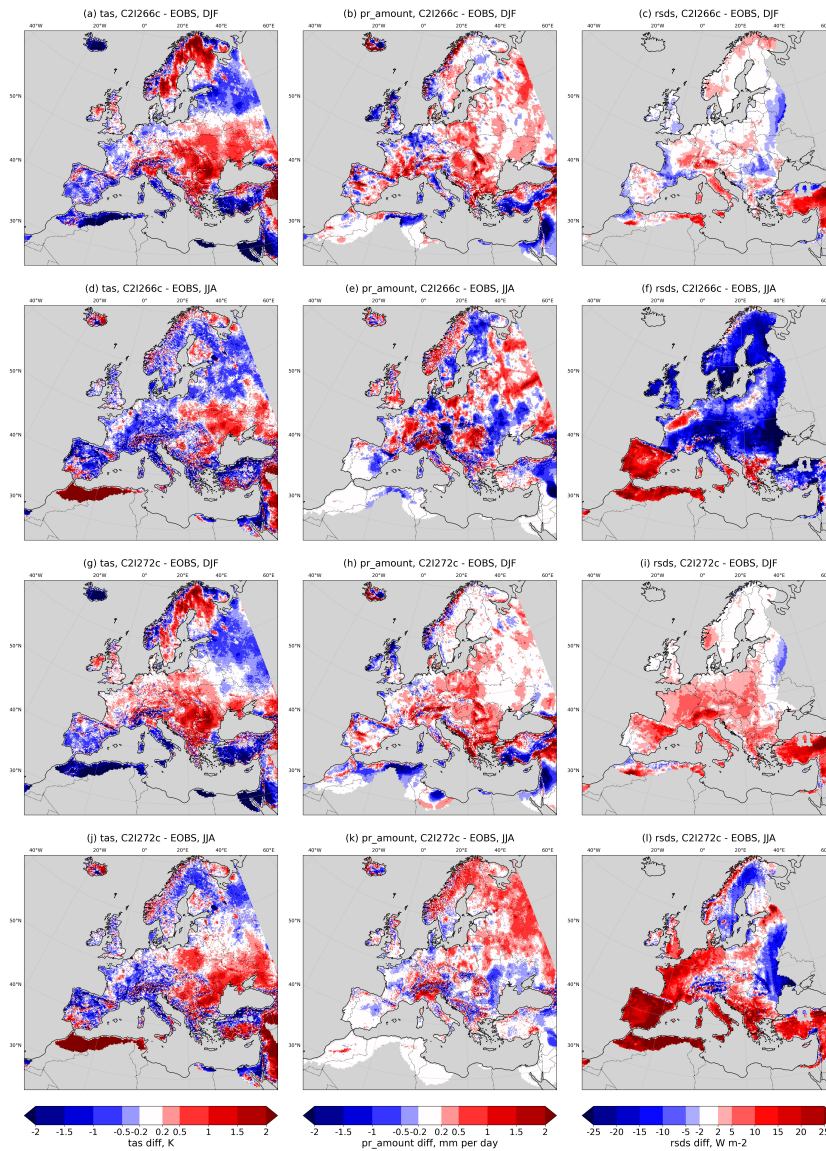


Figure 18. Expert tuning results: Seasonal mean differences in **tas**, **pr_amount**, and **rsds** for winter (DJF) and summer (JJA) for the simulations C2I266 and C2I272 to E-OBS.

3.4.2 LiMmo tuning

This section provides the settings used to configure the LiMmo framework. For detailed information on the LiMmo method, please refer to Sect. 2.4.

We selected the following list of parameters for the LiMmo tuning (check Table 6 to see the description of parameters): `allow_overcast` parameters `ao` and `aoa`, `tune_albedo_wso(1)`, `tune_albedo_wso(2)`, `rlam_heat`,

rat_sea, rat_lam, rsmin_fac, tune_box_liq, and tune_box_liq_asy. Most of these parameters show high sensitivity (see Fig. 2), while tune_albedo_wso(2) signal is very weak. We decided to keep the latter under consideration for consistency, although we do not expect it to significantly affect the results.

As reference simulation, which defines the shift tensor of regression approximation (see Eq. 4), we used C2I250c (see 890 Table D1), since it provides acceptable quality while incorporating the most up-to-date external data sets that we would like to use in the end. Moreover, C2I250c is the simulation of the revised reference configuration (see Sect. 3.3 and compare Fig. 1, 2g).

To define the error norm that is minimised by the gradient method, we have tested two sets of weights for the model quantities, presented in Table 8. These weights are applied to define the quality measure of the configuration (error norm), 895 given in Eq. 8, and have the unit sum. The main difference between the two sets of weights is the reduced weight of **hfls_o** in the second case. The residual 0.05 was added to **rsds**. As we will demonstrate later, this seemingly small adjustment has a strong impact on the LiMMo optimised configuration obtained.

Table 8. Weights of the model variables in the LiMMo optimisation. The columns are named after the model quantities (see Table 2).

variable weights	tas	rsds	tasmin	tasmax	psl	pr_amount	hfls_o
high hfls_o weight	0.15	0.1	0.15	0.15	0.15	0.2	0.1
low hfls_o weight	0.15	0.15	0.15	0.15	0.15	0.2	0.05

As mentioned in Sect. 2.4, the optimisation process (gradient descent) is restricted to the parameter space limited by **MIN** and **MAX** boundaries for each parameter. These values, along with the initial guess, are listed in Table 9. These values were 900 chosen after extensive consultations with ICON developers and experienced users, to ensure the physical consistency of the optimised parameter values. In Table 9, we also present the resulting values for the two sets of weights from Table 8.

Table 9. Limit, initial, and optimal values of the model parameters in the LiMMo optimisation. **MIN** - minimal parameter values, **INI** - initial parameter values in optimisation, **MAX** - maximal parameter values. Also, the resulting values of optimisation for ‘high **hfls_o** weight’ (simulated as C2I291c) and ‘low **hfls_o** weight’ (simulated as C2I294c) from Table 8 are presented in corresponding columns. The settings marked with ‘*’ are given in Table A2.

parameter name	MIN	INI	MAX	optimised, high hfls_o weight (C2I291c)	optimised, low hfls_o weight (C2I294c)
ao	0.8	0.9	1.0	0.934	0.913
aoa (with aoac fixed to t4*)	0.0	1.0	1.5	0.836	1.098
tune_albedo_wso(1)	0.0	0.1	0.15	0.047	0.052
tune_albedo_wso(2)	-0.15	-0.1	0.0	-0.102	-0.097
rlam_heat	5.0	6.25	12	9.66	7.1
rat_sea	0.4	0.8	1.5	1.06	0.9
rat_lam	0.7	1.0	1.3	1.03	1.03
rsmin_fac	0.7	1.0	1.5	1.34	1.36
tune_box_liq	0.04	0.05	0.1	0.066	0.061
tune_box_liq_asy	2.5	3.25	4.5	3.17	3.23

3.5 Optimised model configuration assessment

In this section, we assess the results of simulations using optimised ICON-CLM configurations by comparison with observations for key model quantities, with special emphasis on the tuning aim (reduction of **tas** cold bias and overestimation of **rsds**). The simulation quality for optimised configurations is shown in comparison with the reference simulation C2I200c. The optimised configurations investigated are the new reference configuration C2I250c obtained by expert judgement, the configuration (C2I268c) obtained by expert tuning and two LiMMo optimised configurations. C2I291c is obtained using a high weight for latent heat flux over water **hfls_o** and configuration C2I294c is obtained using a low weight of **hfls_o** (Table 8 in the error norm (Eq. 8)). Since the optimised configurations are based on the setup of C2I250c, a comparison between C2I268c, C2I291c, and C2I294c against C2I250c shows the impact of parameter tuning.

The presentation of the results is grouped into sections, corresponding to the main measures of model quality in this study: the ScoPi scores (Sect. 3.5.1), the seasonal Root Mean Square Error (Sect. 3.5.2), and the 2D seasonal BIAS plots (Sect. 3.5.3). Finally, we select the best configuration that we suggest to all users of ICON-CLM and for the production of EURO-CORDEX regional climate projections in Sect. 3.6.

3.5.1 ScoPi analysis

In Fig. 19 we present the ScoPi scores for the revised reference simulation (C2I250c), the simulation (C2I268c) using the expert tuning, and the simulations C2I291c and C2I294c) using the LiMMo optimised configuration. The score is a

measure of increase/decrease of the simulation quality with respect to the reference simulation C2I200c. The scores for the (land) PRUDENCE regions are shown in Fig. 19 on the left, and the scores for the water sub-regions considering **hfls_o** are shown on the right.

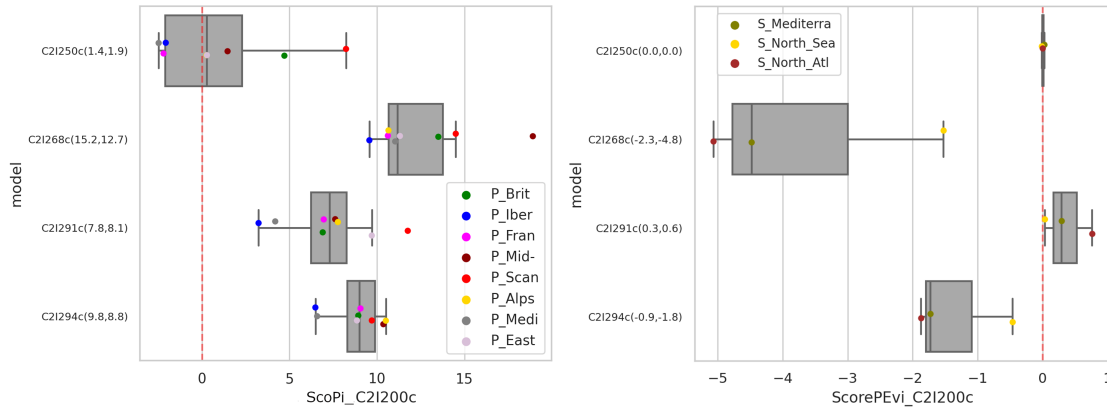


Figure 19. ScoPi_{region} based on the differences in the mean BIAS of all variables labelled with ScoPi weights in Table 2 defined for land points (left) and for ocean points, where only **hfls_o** contributes (right) between the observations and each simulation considered in the final decision (C2I250c, C2I268c, C2I291c, C2I294c), against the simulation C2I200c. The colours indicate the different CORDEX regions. The numbers given on the y-axis labels in brackets are the ScoPi_{simulation}. The values represent the averages over all eight regions weighted by the distance to Mid-Europe (first value), and by their area (second value) respectively (see Table 3). For the additional details see Sect. 2.6.1

The ScoPi of the revised reference C2I250c suggests that the changes in external data sets and updates in model versions do not influence the mean model quality but have impacts on the regional distribution of the biases for the land quantities only.

The expert and LiMMo tuned configurations reveal relatively high positive ScoPi values, indicating significant improvements in simulation quality. The best performing simulation for the land quantities is the expert tuned configuration C2I268c (11.5 points), followed by the LiMMo tuned configuration C2I294c with low weight for **hfls_o** (9 points) and C2I291c with high weight for **hfls_o** (7 points). The improvements are found for all PRUDENCE regions with the weakest ScoPis over the Iberian Peninsula.

The LiMMo tunings C2I291c and C2I294c do not achieve the same model quality as expert tuning C2I268c with respect to ScoPi over land (Fig. 19, left). This, however, is not showing that the expert tuning outperforms LiMMo tuning. It shows that the additional constraint of LiMMo tuning, the reduction of the bias of latent heat flux bias over water (**hfls_o**) is reducing the quality over land, as shown by ScoPi considering land points only. However, the analysis of **hfls_o**-based ScoPi reveals the weak performance in simulating latent heat flux with C2I268c and C2I294c.

3.5.2 Seasonal RMSE analysis

Figure 20 shows the time mean spatial RMSE with respect to observations and all variables considered in the LiMMo optimisation separately for the winter (a), the summer (b) and for all months (c). The values are normalised by the RMSE of C2I200c and shown as percentages. The intrinsic uncertainties of the model (see Eq. 6 and Table 4) are given as vertical whiskers. This allows to assess the statistical significance of the tuning.

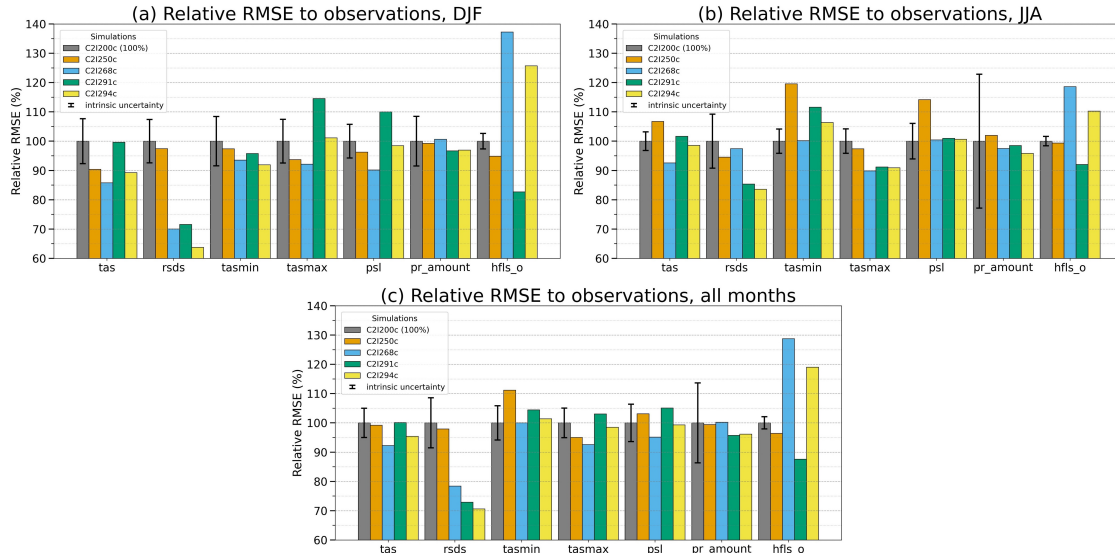


Figure 20. The Root Mean Square (RMS) difference between the model output and observations for different optimised ICON-CLM configurations averaged for (a) winter (DJF), (b) summer (JJA), and (c) all months in the climatological year. RMSE values are displayed for different model quantities (horizontal axis). The vertical whisker reflects the model’s intrinsic uncertainty (Eq. 6, mean values for selected months). All RMSE values and intrinsic uncertainties are normalised to the RMSE for the initial configuration (first bar – C2I200c) for each model quantity. The absolute values of the RMSEs for the C2I200c are shown vertically to the left of the first bar for each model variable. Bars for all model quantities used in LiMMo tuning (see Table 2) are displayed.

First, we could not find a significant change in precipitation RMSE for any of the optimised configurations (see Fig. 20, c for **pr_amount**). The changes of **pr_amount** in both winter and summer RMSE are also below the level of significance (see Fig. 20 a and b for **pr_amount**). This can be explained by the relatively low sensitivity of **pr_amount** to parameter changes considered (see Fig. 2, column **pr_amount**). The initial configuration C2I200c has decent precipitation quality because a similar configuration is used for NWP. Therefore, the precipitation quality of the optimised configurations can be regarded as satisfactory.

Second, the expert optimised configuration C2I268c shows statistically significant improvement of RMSE for **tas** and **tasmx** in winter and summer. The LiMMo optimised configuration C2I294c (low weight of **hfls_o**, see Table 8) also reduces the RMSE significantly for **tas** in winter and for **tasmx** in summer. The second LiMMo configuration C2I291c (high weight

of **hfls_o**, see Table 8) exhibits a different result. In winter, the **tasmax** RMSE is significantly increased. In summer, it is significantly reduced. For **tasmin**, the opposite holds - there is a slight decrease in winter and a significant increase in summer. The slightly reduced quality (5%–10% higher RMSE in comparison with C2I294c) of summer **tasmin** and winter **tasmax** affects climatologically relevant quantities like the number of tropical nights and frost days. This can be accepted for regional climate applications, considering the significant improvement in winter **tasmin** and summer **tasmax**, improving the quality of winter cold nights and summer hot days. It allows for keeping or even improving the predictability of cold events in winter and heat waves in summer, which are usually of the main interest for the risk assessments.

Third, Fig. 20 shows significant and strong differences in **rsds** and **hfls_o** (for optimised configuration with respect to C2I200c). The results are similar for C2I200c and C2I250c. Thus, updating the external parameters has a minor impact on these quantities. A large and significant decrease of up to 30% in **rsds** RMSE was found for the expert (C2I268c) and LiMMo-optimised (C2I291c, C2I294c) configurations with 30% to 35% in winter for all three and about 15% to 20% in summer for the LiMMo configurations only.

Fourth, the **rsds** RMSE reductions in C2I268c and C2I294c are accompanied by a significant and strong increase of the **hfls_o** RMSE (30% to 40% in winter and 10% to 20% in summer). The C2I291c configuration, however, is the only one showing a significant and strong reduction of **hfls_o** RSME in both seasons (~17% in winter and ~7% in summer).

3.5.3 2D seasonal BIAS analysis

In the current section, we show the seasonally averaged 2-dimensional bias plots for the most significant changes identified in the RMSE analysis (see Fig. 20 in Sect. 3.5.2).

First, we compare the 2-dimensional biases of summer **tasmin** and winter **tasmax** for configurations C2I200c, C2I250c, and C2I291c in the Fig. 21 to ensure that there are no severe violations of the model quality by the configuration changes in these quantities. The update of the external data sets leads to an overall positive temperature shift in summer **tasmin** (Fig. 21 b vs. a). The LiMMo tuning slightly reduces the summer **tasmin** bias, especially in central Europe and northern Africa (Fig. 21 c vs b), but the bias still remains overall positive and larger than in the original setup (Fig. 21 c vs. a). The positive temperature shift is visible for winter **tasmax** as well (Fig. 21 e vs. d), slightly reducing the negative bias. However, the LiMMo tuning reverses this improvement, leading to a slightly stronger negative bias (Fig. 21 f vs. d). This degradation is mainly confined to the northern African region. Overall, the quality of the summer **tasmin** and winter **tasmax** can be regarded as similar in C2I291c and C2I200c, especially for the target region of central Europe.

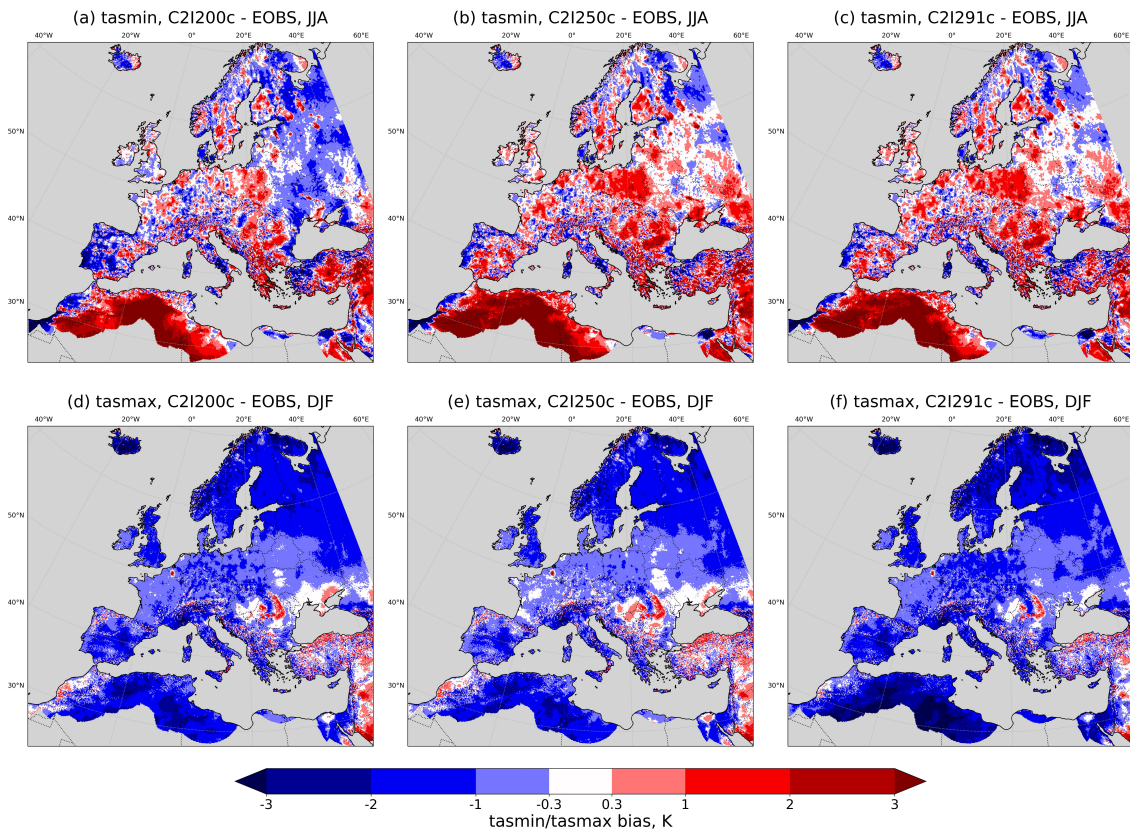


Figure 21. Seasonal biases (2003–2008) for summer **tasmin** (top) and winter **tasmax** (bottom) for configurations C2I200c, C2I250c and C2I291c compared to E-OBS.

Second, in Fig. 22 we present the summer **rsds** and winter **hfls_o** biases for C2I200c, C2I268c, and C2I291c. The LiMMo parameter tuning clearly reduces the positive **rsds** bias over central and western Europe while slightly increasing it in Eastern Europe (Fig. 22 c vs. a). The expert tuning results in an enhanced negative bias over central and eastern Europe (Fig. 22 b vs. a), while slightly reducing the positive bias in Western Europe. Along with the ambiguous performance for **rsds**, we observe a strong degradation of winter **hfls_o** of 10 W m^{-2} in the Expert configuration C2I268c (Fig. 22 e vs. d). The LiMMo configuration C2I291c provides clearly reduced bias in the Atlantic and Mediterranean (Fig. 22 f vs. d).

A comprehensive analysis of seasonal 2D biases for **tas**, **tasmin**, **tasmax**, **rsds**, **hfls_o**, **pr_amount** and **psl** is provided in the supplementary materials (see Sect. S5).

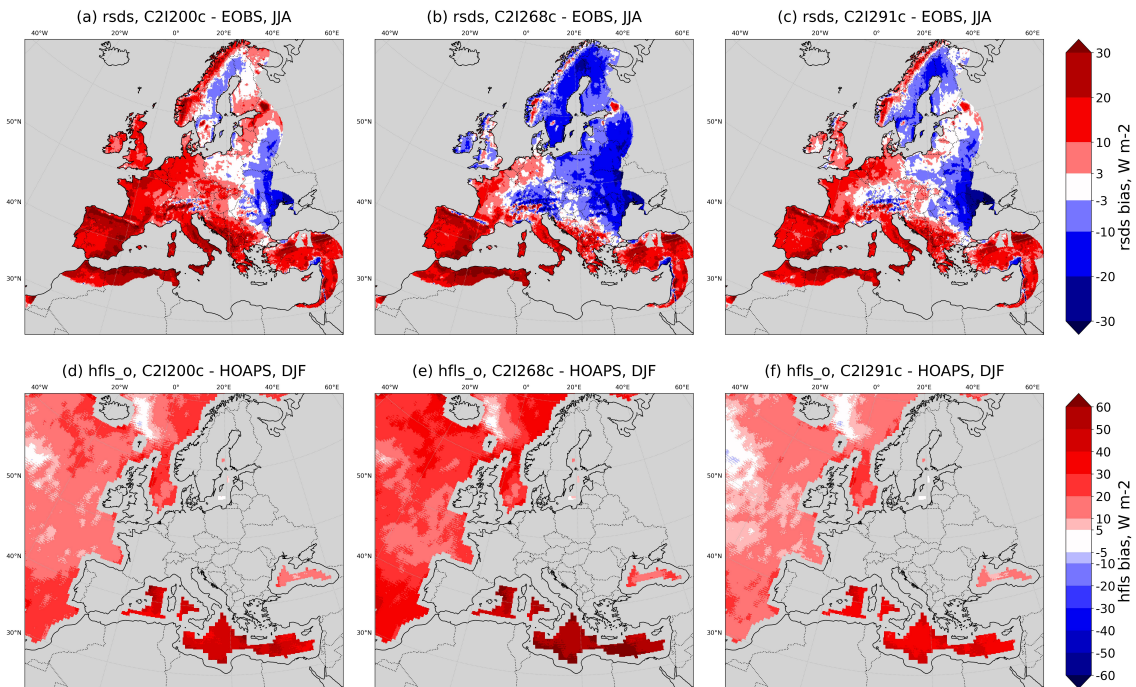


Figure 22. Seasonal biases (2003–2008) for summer **rsds** (top) and winter **hfls_o** (bottom) for configurations C2I200c, C2I268c and C2I291c compared to E-OBS and HOAPS, respectively.

3.6 Recommended optimised configuration

The evaluation results show that the optimised configuration C2I268c, obtained by expert tuning, and C2I291c and C2I294c, obtained by LiMMo tuning, exhibit a significant reduction of overestimation of incoming solar radiation at the surface, i.e., they reach one of the tuning aims. Additionally, the configuration C2I268c shows a significant reduction of **tas** bias. However, the Expert configuration C2I268c and the LiMMo configuration C2I294c with low weight of **hfls_o** exhibit a much increased **hfls_o** bias (+25 %, Fig. 20 c) in comparison with C2I200c. The LiMMo configuration C2I291c is the only one which reveals major improvements in incoming short wave radiation at the surface **rsds** (30 % reduction of **rsds** RMSE, Fig. 20 c) and latent heat flux over the ocean **hfls_o** (12 % reduction of **hfls_o** RMSE, Fig. 20 c). This improvement is accompanied by a statistically significant worsening of **tasmax** in the winter season only (+15 % in winter **tasmax** RMSE, Fig. 20 a).

In expert tuning, five parameters were tuned. In LiMMo tuning, ten parameters were tuned. A comparison of the tuned parameter values from the optimised expert and LiMMo configurations (Table 10) reveals differences higher than 10 % of the parameter value in the cloud condensation parameter `tune_box_liq`, in resistance parameters of turbulent fluxes over land (`rlam_heat`) and oceans (`rat_sea·rlam_heat`), in the factor of minimum stomata resistance to transpiration (`rsmin_fac`) and in the correction of dry soil albedo (`tune_albedo_wso(1)`).

The parameter sensitivities given in Figure 2 indicate that the reduction of the error in **hfls_o** is related to `rat_sea·rlam_heat`. Since the value 5 is found to be a lower limit of physically meaningful values, the value 9.7 in C2I291c can be

regarded as physically well justified. The parameter `tune_box_liq` has a much smaller sensitivity than `tune_box_liq_asy` and `allow_overcast`, and thus it can be regarded as less important. The stomata resistance factor exhibits no sensitivity, and its increase by 30 % is thus physically acceptable as well. The albedo increase for dry soils is found half size in LiMMo in comparison with the optimised Expert configuration and thus physically even more acceptable.

All in all, the LiMMo configuration is closer to the reference configuration and physically more reliable than the optimised Expert configuration. This confirms the evaluation results. Therefore, we recommend using the LiMMo tuned configuration C2I291c with the high weight of `hfls_o`.

For climate change applications, we recommend using the urban parametrisation `terra_urb` additionally. Urban areas contribute only marginally to regional means and do not affect the consistency with E-OBS, as inner city stations are excluded there. But the parameterisation is important to capture the urban heat island effects.

Table 10. Reference simulations and all configurations used in the final decision making. Rows: tuning parameters (see Table 5 and Table 6); columns: simulation IDs (see Table D1). The settings marked with ‘*’ are given in Table A2. If the value in a cell is missing, it is replaced with its neighbouring value to the left.

	C2I100c	C2I200c	C2I250c	C2I268c	C2I291c	C2I294c
configuration description	initial reference	first revised reference	second revised reference	expert tuning	LiMMo tuning high <code>hfls_o</code> weight	LiMMo tuning low <code>hfls_o</code> weight
AEROSOL	Tegen*	MACv2-SP*				
<code>czbot_w_so</code>	2.5	4.5				
<code>zml_soil</code>	<code>zml1</code> *	<code>zml2</code> *				
SOIL-DATA	FAO*		HWSD v2.0*			
AEROSOL-CLOUD-FB	<code>ac-fb0</code> *		<code>ac-fb1</code> *			
ORO+TUNING	GLOBE*		MERIT*			
<code>tune_box_liq</code>	0.05				0.066	0.061
<code>tune_box_liq_asy</code>	3.25				3.17	3.23
(<code>ao</code> , <code>aoa</code> , <code>aoac</code>)	(1.0,-,-)			(0.9,-,-)	(0.934, 0.836, t4*)	(0.913, 1.098, t4*)
<code>rat_sea</code>	0.4	0.8			1.06	0.9
<code>rlam_heat</code>	10.0			6.25	9.66	7.1
<code>rat_lam</code>	1.0				1.03	1.03
<code>tune_albedo_wso(1)</code>	0.0			0.1	0.047	0.052
<code>tune_albedo_wso(2)</code>	0.0			-0.1	-0.102	-0.097
<code>rsmin_fac</code>	1.0				1.34	1.36

4 Summary and Conclusions

In this paper, we introduce a strategy and concrete procedures for tuning regional climate models. The generic framework was used to derive an optimised configuration for the ICON model in climate limited-area mode (ICON-CLM) for the CORDEX pan-European model domain at 12 km (EUR-12) grid resolution. The RCM tuning strategy presented here is a significantly improved procedure compared to the one previously used for the COSMO-CLM. This tuning strategy comprised parameter testing, revision of the reference configuration by expert judgement, configuration optimisation using expert tuning and an assessment of the optimised configurations using the ScoPi measure (Geyer, 2026). In the present study, this was extended by the application of the novel Linear Meta-model (LiMMo) tuning framework. It adds value to the overall procedure as it can be seamlessly combined with, or used instead of, expert tuning. Furthermore, it can substantially extend the optimisation space by optimising a large number of parameters, since the number of the simulations required for the LiMMo tuning is equal to the number of tuned parameters plus three.

Aside from an optimised model configuration, targeted to a specific optimisation goal, we present and discuss the model parameter sensitivities, which are the basis of the optimisation procedure.

Following the tuning strategy, the results of its application to ICON-CLM can be summarised as follows:

First, the tuning aim was determined from the reference simulation assessment. The analysis revealed a 1.5 K cold bias in 2m-temperature, an overestimation of incoming surface solar radiation by more than 10 W m^{-2} , and an overestimation of latent heat flux over the ocean surface by more than 15 W m^{-2} in spatial and yearly means. The reduction of these biases was determined to be the tuning aim.

Second, new external data sets for soil type (HWSD v2.0), orography (MERIT), and transient aerosols (MACv2-SP) have been incorporated for the first time. The revised reference configuration (by expert judgement) became the basis for the further testing of model parameters.

Third, the sensitivity of model results on parameters of cloud cover dependency on atmospheric water content, of vertical mixing, convection, and of surface fluxes were investigated. Two new parameters of soil moisture dependence of surface albedo and two of plant transpiration and evaporation have been tested. The test simulation results have been evaluated for key model quantities: **tas**, **tasmin**, **tasmax**, **rsds**, **pr_amount**, **hfls_o**, and **psl**. The discussion of the model response revealed sometimes counter-intuitive, but physically consistent model behaviour. The majority of parameters have been shown to have a model sensitivity that is significantly higher than the intrinsic model variability.

Third, we determined an optimised configuration by expert tuning. Hereby up to six out of twelve sensitive tuning parameters have been adjusted, which have been found to exhibit a sensitivity correlated with substantial parts of the model bias. The optimised Expert configuration has been shown to reduce errors by 8 % for **tas** and **tasmax**, 20 % for **rsds**, and to increase **hfls_o** errors by 30 %.

Fourth, we applied LiMMo tuning, which is based on a linear emulator of monthly mean values and optimisation of the error norm consisting of weighted signal-to-noise ratios for model variables. We considered the results of tuning twelve sensitive

model parameters using two sets of weights for model variables in LiMMo. The ICON-CLM simulations with LiMMo-derived configurations confirmed the bias reductions found by the meta-model.

The optimisation of all twelve tuning parameters in LiMMo tuning allowed us to find a configuration with a smaller error norm than in expert tuning. However, the model error reduction remained limited to a few variables (30 % reduction of **rsds** and 15 % reduction of **hfls_o** yearly mean RMSE). This indicates that a further error reduction might be impossible only by existing parameter tuning without further model development.

The LiMMo configuration, which was obtained for the low weight of **hfls_o**, shows a quality similar to that found by expert tuning. The LiMMo configuration for a high weight of **hfls_o** reduces the error norm of incoming solar radiation by 30 % and of latent heat flux over water by 15 % while keeping the simulation quality of temperature, pressure, and precipitation similar to the reference (insignificantly worse). This also demonstrates the possibility of controlling the tuning result by the user. The method's linear computational complexity allows it to be extremely efficient, yielding results in just a few minutes. This is one of the strengths, combined with the relatively small number of simulations needed.

We consider a combination of expert tuning, a step-wise improvement of reference configurations, in combination with LiMMo (fine-tuning) as a best practice RCM tuning strategy.

The new ICON-CLM configuration for climate mode applications with a spatial resolution of 12 km over the European region, as determined by the hybrid expert-LiMMo tuning, is already in use, e.g., by the CLM-Community for WCRP CORDEX-CMIP6 EURO-CORDEX climate change simulations.

Appendix A: Namelist parameter descriptions

Table A1: Description of namelist parameters changed in the optimisation process; the full list of namelist parameters for ICON can be accessed at https://gitlab.dkrz.de/icon/icon-model/-/tree/release-2025.04-public/doc/Namelist_overview (last access: 3 June 2025).

Namelist Parameter	Values	Description
acor_st1-st2	0.0, 0.1	Bare soil albedo correction for (low,high) soil water content w_{so} ($< 0.01, > 0.02$) and soil types st1 to st2 (4:sandy-loam, 5:loam, 6: loamy clay)
allow_overcast	1.0, 0.6, 0.87, 0.88, 0.9, 0.909	Tuning factor for the dependence of liquid cloud cover on relative humidity. This is an unphysical ad-hoc parameter to improve the cloud cover in the Mediterranean
allow_overcast_yc	ao_yc	Monthly values for allow_overcast settings

Namelist Parameter	Values	Description
c_soil	1.0, 0.75, 1.25, 2.0	Surface area density of the (evaporative) soil surface; allowed range: 0 – 2
cr_bsmin	110, 50, 150	Minimum bare soil evaporation resistance (see Schulz and Vogel 2020) Note: c_soil and c_soil_urb are ignored in this case
crsmin	250	Minimum transpiration resistance
czbot_w_so	2.5, 4.5	Thickness of the hydrological active soil layer
dt_conv	300, 600	Time interval of convection call.
dt_rad	900, 2400	Time interval of radiation call.
dt_sso	600, 1200	Time interval of sso call.
dt_gwd	600, 1200	Time interval of gwd call.
ecrad_llw_cloud_scatter	.false., .true.	Long-wave cloud scattering.
irad_aero	6, 18	18: MACv2 aerosols, simple plume anthropogenic plus Stenchikov's volcanic aerosols are used
icalc_reff	0, 100	0: No calculation; 100: Consistent with current microphysics (it sets icalc_reff = inwp_gscp)
icpl_aero_conv	1, 0	0: off 1: simple coupling between autoconversion and Tegen aerosol climatology; requires irad_aero=6
icpl_aero_gscp	0, 1, 3	0: off; 1: simple coupling between autoconversion and Tegen aerosol climatology; 3: use cloud-droplet number climatology from the external parameter file. External parameter files containing cloud-droplet number climatology can be generated with extpar code from version rc_5.14
icpl_rad_reff	1, 0	0: No coupling. The calculation of the effective radius happens at the radiation interface. 1: Radiation uses the effective radius defined by icalc_reff. All hydrometeors are combined in a frozen and a liquid phase.
inwp_cldcover	1, 3	1: diagnostic cloud cover (by Martin Koehler); 3: clouds from COSMO SGS cloud scheme
inwp_gscp	1, 3	1: hydei (COSMO-EU microphysics, 2-cat ice: cloud ice, snow) 3: as 1, but with new ice nucleation scheme by Koehler

Namelist Parameter	Values	Description
irad_o3	79, 5	79: Blending between GEMS and MACC ozone climatologies (from IFS) for run_nml/forcing = 3 (NWP); MACC is used over Antarctica; 5: 3-dim concentration, time dependent, monthly means from yearly files bc_ozone_<year>.nc
isolrad	1, 2	1: Use SSI values from Coddington et al. (2016) (inwp_radiation=1) or scale SSI values to Coddington et al. (2016) values (inwp_radiation=4) 2: SSI from an external file containing monthly mean time series (inwp_radiation=4)
itype_evsl	4, 5	4: Resistance-based formulation by Schulz and Vogel (2020); 5: same as 4, but uses the minimum evaporation resistance (default set by cr_bsmin) instead of c_soil for tuning; the namelist parameter c_soil is ignored in this case and a value of 2 is used internally
itype_hydmmod	.false., .true.	.true.: horizontal transport of water in the soil due to gravitation Schlemmer et al. (2018)
itype_z0	2, 3	2: land-cover-related roughness based on tile-specific land use class 3: land-cover-related roughness based on tile-specific land use class, including contribution from sub-scale orography
lcalib_clcov	.true., .false.	Apply calibration of layer-wise cloud cover diagnostics over land in order to improve scores against SYNOP reports
lrestune_off	.false., .true.	.true.: switches off resolution-dependent tuning of shallow convection parameters
lstoch_sde	.false., .true.	.true.: activate stochastic differential equation (SDE) shallow convection scheme to be used in conjunction with lrestune_off=.T. and lmflimiter_off=.T.
lmflimiter_off	.false., .true.	.true.: disables mass flux limiter by setting it to high values that are rarely reached by shallow convection
lsgs_cond	.true., .false.	.true.: Apply sub-grid scale condensational heating related to the non-convective part of diagnosed cloud water. Requires inwp_cldcover=1
lstomata	.true., .false.	.true.: use map of minimum stomatal resistance; .false.: use constant value of 150 s/m.

Namelist Parameter	Values	Description
lterra_urb	.false., .true.	If .true., activate urban model TERRA_URB by Wouters et al. (2016)
pp_sso	1, 2	1: Postprocess SSO standard deviation and slope over glaciers based on the ratio between grid-scale and subgrid-scale slope: both quantities are reduced if the subgrid-scale slope calculated in extpar largely reflects the grid-scale slope. 2: Optimised tuning for MERIT orography data: the reduction is also applied at non-glacier points in the Arctic, and the adjustment of the SSO standard deviation to orography smoothing is turned off.
rlam_heat	10.0, 2.5, 3.0, 4.0, 5.0, 6.25, 7.1, 9.66	Scaling factor of the laminar boundary layer for heat (scalars). The larger rlam_heat, the larger is the laminar resistance.
rat_lam	0.9, 1.0, 1.03, 1.2, 1.3	The larger rat_lam, the larger is the laminar resistance to turbulent heat fluxes over land
rat_sea	0.8, 0.4, 0.664, 0.7, 0.8, 0.9, 1.06, 1.6	Ratio of laminar scaling factors for scalars over sea and land. The larger rat_sea, the larger the laminar resistance for the sea surface compared to the land surface.
rsmin_fac	1.0, 1.3, 1.34, 1.36	Scaling factor of resistance of plant transpiration
tkhmin	0.6, 0.9	Scaling factor for minimum vertical diffusion coefficient (proportional to $Ri^{-2/3}$) for heat and moisture
tkmmin	0.75, 0.375, 1.125	Scaling factor for minimum vertical diffusion coefficient (proportional to $Ri^{-2/3}$) for momentum
tune_albedo_wso	(0,0), (0.1,-0.1), (0.1,0), (0,-0.05), (0.047,-0.102), (0.052,-0.097), (0.047,-0.102)	Bare soil albedo correction for soil type 3–6 (sand, sandy-loam, loam, clay-loam) and soil water content $w_{so} > 0.02$ (wet) soil water content $w_{so} < 0.01$ (dry) respectively.
tune_box_liq_asy	2.0, 3.17, 3.25, 4.0	Asymmetry factor for liquid cloud cover diagnostic
tune_box_liq	0.05, 0.07, 0.061, 0.066	Box width for liquid cloud diagnostic in cloud cover scheme
tune_gfrcrit	0.425, 0.35	Critical Froude number (controls depth of blocking layer)
tune_grcrit	0.25, 0.5	Critical Richardson number (controls onset of wave breaking)
tune_gkdrag	0.075, 0.08	Gravity wave drag constant

Namelist Parameter	Values	Description
tune_gkwake	1.5, 0.65	Low level wake drag constant (adapted for change from GLOBE to MERIT)
tune_gust_diag	1, 2	Method of SSO blocking correction used in the gust diagnostics 1: Use level above 'SSO envelope top' for gust enhancement over mountains; 2: Use 'SSO envelope top' level for gust enhancement over mountains, combined with an adjusted non-linearity factor (recommended for global configurations with MERIT orography)
tune_minss0	10, 1	Minimum SSO standard deviation for which SSO scheme is applied
tune_blockred	100, 1.5	Multiple of SSO standard deviation above which blocking tendency is reduced
zml_soil	zml1, zml2 as defined in Table 5	Soil full layer depths

Table A2. Description of the parameter settings abbreviated in Table 5, Table 6, Table 7, Table 9 and Table 10.

Acronym	Table	Description
Tegen	5,10	Tegen external data, <code>irad_aero=6</code> , <code>icpl_aero_conv=1</code> , <code>icpl_aero_gscp=1</code>
MACv2-SP	5,10	MACv2 external data, <code>irad_aero=18</code> , <code>icpl_aero_conv=0</code> , <code>icpl_aero_gscp=0</code>
1-ice	5	<code>inwp_gscp=1</code> , <code>icalc_reff=0</code> , <code>icpl_rad_reff=0</code>
2-ice	5	<code>inwp_gscp=3</code> , <code>icalc_reff=100</code> , <code>icpl_rad_reff=1</code>
dt1	5	<code>dt_conv=300</code> , <code>dt_rad=900</code> , <code>dt_sso=600</code> , <code>dt_gwd=600</code>
dt2	5	<code>dt_conv=600</code> , <code>dt_rad=2400</code> , <code>dt_sso=1200</code> , <code>dt_gwd=1200</code>
zml1	5,10	soil levels: 0.005, 0.02, 0.06, 0.18, 0.54, 1.62, 4.86, 14.58
zml2	5,10	soil levels: 0.005, 0.025, 0.07, 0.16, 0.34, 0.7, 1.42, 2.86, 5.74, 11.5
cloud1	5	<code>allow_overcast=1.0</code> , <code>tune_box_liq_asy=3.25</code> , <code>max_calib_clcl=4.0</code>
cloud2	5	<code>allow_overcast=0.6</code> , <code>tune_box_liq_asy=2.0</code> , <code>max_calib_clcl=2.2</code>
FAO	5,10	The FAO – external soil database
HWSD v2.0	5,10	The Harmonised World Soil Database v2.0 (HWSD v2.0) – external soil database
GLOBE	5,10	GLOBE orography data, <code>tune_gkwake=1.5</code> , <code>tune_gfrcrit=0.425</code> , <code>tune_gkdrag=0.075</code> , <code>itune_gust_diag=1</code> , <code>tune_grcrit=0.25</code> , <code>tune_minssso=10</code> , <code>tune_blockred=100</code> , <code>pp_sso=1</code>
MERIT	5,10	MERIT orography data, <code>tune_gkwake=0.65</code> , <code>tune_gfrcrit=0.35</code> , <code>tune_gkdrag=0.08</code> , <code>itune_gust_diag=2</code> , <code>tune_grcrit=0.5</code> , <code>tune_minssso=1</code> , <code>tune_blockred=1.5</code> , <code>pp_sso=2</code>
ac_fb0	5,10	<code>icpl_aero_gscp=0</code> , <code>icalc_reff=0</code>
ac_fb1	5,10	<code>icpl_aero_gscp=3</code> , <code>icalc_reff=100</code>
aoac	6	The annual cycle of <code>allow_overcast</code> monthly deviations from the mean: (-0.02, -0.06, -0.03, 0.02, 0.05, 0.02, 0.02, 0.02, -0.02, -0.04, -0.04, -0.03)
t1	7	The annual cycle of <code>allow_overcast</code> monthly deviations from the mean: (-0.02, -0.02, -0.02, -0.02, 0.05, 0.05, 0.05, 0.05, 0.05, -0.02, -0.02, -0.02)
t2	7	The annual cycle of <code>allow_overcast</code> monthly deviations from the mean: (-0.02, -0.06, -0.03, 0.02, 0.05, -0.02, 0.0, 0.02, -0.02, -0.04, -0.04, -0.03)
t4	7,9,10	The annual cycle of <code>allow_overcast</code> monthly deviations from the mean: (-0.02, -0.06, -0.03, 0.02, 0.05, 0.02, 0.02, 0.02, -0.02, -0.04, -0.04, -0.03)

Appendix B: Additional technical information on experiment setups

Table B1. Overview of periods used for simulation, analysis, and optimisation.

SimulationID period for	C2IXXX	C2IXXXc
simulation	01.1979–12.1984	01.2002–12.2008
optimisation	01.1980–12.1984	01.2003–12.2008
analysis	01.1980–12.1984	01.2003–12.2008

Table B2. Overview of used model versions.

model version	simulation	comment
release icon-2.6.6	C2I100 to 122, C2I130	
release icon-2.6.6_v01	C2I127 to 128, C2I200 to 207	release + bug fix for soil levels
release icon-2.6.6_v02	C2I129	release + groundwater scheme (Schlemmer et al., 2018)
release icon-2.6.6_v03	C2I208 (c) to 223c	release + internal parameter settings;
release icon-2024.01_v01	C2I230 to 239	release + bug fix for soil levels
icon-nwp:master of 19/02/2024	C2I240 to 241	master including Modis CDNC
icon-nwp:icon-nwp-master-20240219_clm	C2I245 to 281	master + <i>acor</i> + <i>rsmín_fac</i>
icon-nwp:master of 07/06/2024	C2I284c to 294	master including <i>tune_albedo_wso</i> + <i>rsmín_fac</i>
release icon-2024.07	C2I300c to 301c	

Table C1: Description of changes in the model setup of different experiments to define a new reference compared to the initial reference experiment C2I101.

ID	Namelist Parameter	Value in C2I101	Tested Value	Description
C2I103	lterra_urb	false	true	lterra_urb test
C2I105	irad_aero	6	18	MACv2
	icpl_aero_conv	1	0	+ simple plume
	icpl_aero_gscp	1	0	aerosol test
C2I107	ecrad_llw_cloud_scat	false	true	ecrad_llw_cloud_scat test
C2I108	inwp_gscp	1	3	new
	icalc_reff	0	100	ice nucleation
	icpl_rad_reff	0	1	scheme test
C2I109	lsgs_cond	true	false	lsgs_cond test
C2I110	dt_conv	300	600	frequency of sgs physics test
	dt_rad	900	2400	
	dt_sso	600	1200	
	dt_gwd	600	1200	
C2I111	itype_evsl	4	4	c_soil test
	c_soil	1.25	0.75	
C2I112	itype_evsl	4	5	cr_bsmin test
	cr_bsmin	NA	50	
C2I113	itype_evsl	4	5	cr_bsmin ref
	cr_bsmin	NA	110	
	c_soil	1.25	NA	
C2I114	lstoch_sde	false	true	lstoch_sde test
	lrestune_off	false	true	
	lmflimiter_off	false	true	

ID	Namelist Parameter	Value in C2I101	Tested Value	Description
C2I117	inwp_cldcover	1	3	cloud cover scheme test
	lsgs_cond	true	false	
C2I118	irad_o3	79	5	use transient ozone
C2I119	isolrad	1	2	use transient irradiance
C2I121	itype_evsl	4	4	
	c_soil	1.25	2	
C2I122	itype_z0	2	3	itype_z0 test
C2I127	zml_soil	zml1	zml2	zml_soil test
	czbot_w_so	2.5	4.5	
	zml1 [m]	0.005, 0.02, 0.06, 0.18, 0.54, 1.62, 4.86, 14.58		
	zml2 [m]	0.005, 0.025, 0.07, 0.16, 0.34, 0.7, 1.42, 2.86, 5.74, 11.5		
C2I128	zml_soil	zml1	zml2	zml_soil test
C2I129	itype_hydm0d	–	1	test of the Schlemmer et al. (2018) groundwater scheme
	extpar	–	maxOro	
C2I130	allow_overcast	1.0	0.6	cloud
	tune_box_liq_asy	3.25	2.0	parameter
	max_calibfac_clcl	4.0	2.2	test

Appendix D: Further sensitivity test experiments and simulations with configurations by expert and LiMMo tuning

Table D1: Description of changes in the model setup of further sensitivity studies and the configurations proposed by expert and LiMMo tuning with respect to their reference experiment.

ID	Namelist Parameter	Value in C2I101	Tested Value	Description
-----------	-------------------------------	------------------------	---------------------	--------------------

ID	Namelist Parameter	Value in C2I101	Tested Value	Description
	lcalib_clcov	true	false	
	irad_aero	6	18	
	icpl_aero_conv	1	0	
C2I200	icpl_aero_gscp	1	0	new
C2I200c	irad_o3	79	5	reference
	isolrad	1	2	
	czbot_w_so	2.5	4.5	
	zml_soil	zml1	zml2	

ID	Namelist Parameter	Value in C2I200	Tested Value	Description
C2I201	allow_overcast	1.0	0.9	
C2I202	tune_box_liq_asy	3.25	4	tune_box_liq_asy test
C2I203	tune_box_liq	0.05	0.07	tune_box_liq test
	itype_evsl	4	5	
C2I204	c_soil	1.25	NA	cr_bsmin test
	cr_bsmin	NA	150	
C2I205	rlam_heat	10	6.25	rlam_heat test
	Orography	GLOBE	MERIT	
	tune_gkwake	1.5	0.65	
	tune_gfrcrit	0.425	0.35	
	tune_gkdrag	0.075	0.08	
C2I206	itune_gust_diag	1	2	MERIT orography + tuning test
	tune_grcrit	0.25	0.5	
	tune_minssso	10	1	
	tune_blockred	100	1.5	
	pp_sso	1	2	
C2I207	experimentStartDate	1979/01/01	1978/12/01	intrinsic variability run

ID	Namelist Parameter	Value in C2I200	Tested Value	Description
C2I208 C2I208c	acor	-0.06	0.1	acor test
C2I211	lstomata	.true.	.false.	
	crsmin	map	250	
	itype_evsl	4	5	
	cr_bsmin	NA	110	
	c_soil	1.25	NA	
C2I211c	lstomata	.true.	.false.	
	crsmin	map	250	
C2I214c	rlam_heat	10	5	rat_sea
	rat_sea	0.8	0.4	reference
	acor_5-6)	(0,0)	(0.1,-0.06)	
C2I217c	rlam_heat	10	5	rat_sea test
	rat_sea	0.8	0.7	rlam_heat and
	acor_5-6	(0,0)	(0.1,-0.06)	rat_lam reference
C2I219c	rlam_heat	10	5	
	rat_sea	0.8	0.7	
	rat_lam	1	0.9	
C2I220c	rlam_heat	10	5	
	rat_sea	0.8	0.4	rat_lam test
	rat_lam	1	0.8	
C2I222c	allow_overcast	1.0	0.9	allow_overcast test
C2I223c	rlam_heat	10	5	
	rat_sea	0.8	0.7	
	rat_lam	1	1.3	
C2I230	model version	2.6.6	2024.01_v01	tkhmin+tkmmin and soil data ref
C2I232	soil data	FAO	HWSD2v2	HWSD2v2 test

ID	Namelist Parameter	Value in C2I200	Tested Value	Description
C2I234	rlam_heat	10	5	
	rat_sea	0.8	1.6	
C2I235	tkhmin	0.6	0.3	tkhmin+tkmmin
	tkmmin	0.75	0.375	test
C2I237	Soil initialisation	ref	clim	
C2I238	tkhmin	0.6	0.9	
	tkmmin	0.75	1.125	
C2I240	Model Version			Aerosol-Cloud feedback reference
C2I241	icpl_aero_gscp	0	3	Aerosol-Cloud
	icalc_reff	0	100	Feedback test
C2I245	acor_4-6	(0,0)	(0.1,-0.1)	
C2I250c	soil moisture init	ref	clim	
	soil data	FAO	HWSD v2.0	
	orography+tuning	GLOBE	MERIT	
	icpl_aero_gscp	0	3	
	icalc_reff	0	100	
ID	Namelist Parameter	Value in C2I250c	Tested Value	Description
C2I262c	allow_overcast	1.0	0.9	
	rlam_heat	10	3.0	
	rat_sea	0.8	0.7	
	acor_4-6	(0,0)	(0.1,-0.1)	
C2I266c	tune_box_liq_asy	3.25	4.0	
	rlam_heat	10	5	
	rat_sea	0.8	0.7	
	rat_lam	1.0	1.2	
	acor_4-6	(0,0)	(0.1,-0.1)	

ID	Namelist Parameter	Value in C2I250c	Tested Value	Description
C2I268c	allow_overcast	1.0	0.9	
	rlam_heat	10	6.25	
	acor	(0,0)	(0.1,-0.1)	
C2I270c	allow_overcast	1.0	0.9	
	rlam_heat	6.25	4.00	
	acor	(0,0)	(0.1,-0.1)	
C2I271c	allow_overcast	1.0	0.9	
	rlam_heat	10	6.25	
C2I284c	allow_overcast	1.0	0.9	allow_overcast_yc + tune_albedo_wso reference
	rlam_heat	10	6.25	
	tune_albedo_wso	(0,0)	(0.1,-0.1)	
	icpl_aero_gscp	3	0	
C2I285c	allow_overcast	1.0	0.9	allow_overcast_yc test + rsmin_fac reference
	allow_overcast_yc4	0.0	1.0	
	rlam_heat	10	6.25	
	tune_albedo_wso	(0,0)	(0.1,-0.1)	
C2I287c	allow_overcast	1.0	0.9	tune_albedo_wso(1) reference + tune_albedo_wso(2) test
	allow_overcast_yc4	0.0	1.0	
	rlam_heat	10	6.25	
	tune_albedo_wso	(0,0)	(0.1,-0.1)	
	rsmin_fac	1.0	1.3	
C2I288c	allow_overcast	1.0	0.9	tune_albedo_wso(1)
	rlam_heat	10	6.25	reference
C2I289c	allow_overcast	1.0	0.9	tune_albedo_wso(1) test
	allow_overcast_yc4	0.0	1.0	
	rlam_heat	10	6.25	
	tune_albedo_wso	(0,0)	(0.1,0)	
	rsmin_fac	1.0	1.3	

ID	Namelist Parameter	Value in C2I250c	Tested Value	Description
C2I290c	allow_overcast	1.0	0.9	
	allow_overcast_yc4	0.0	1.0	
	rlam_heat	10	6.25	
	tune_albedo_wso	(0,0)	(0,-0.05)	
	rsmin_fac	1.3	1.3	
C2I291c	C2I250c +	-	-	
	allow_overcast_yc	-	-	
	tune_albedo_wso	-	(0.047, -0.102)	
	tune_box_liq_asy	3.25	3.17	
	tune_box_liq	0.05	0.066	
	rat_sea	0.8	1.06	
	rlam_heat	10	9.66	
	rat_lam	1.0	1.03	
	rsmin_fac	1.0	1.34	
C2I294c	C2I250c +	-	-	
	allow_overcast_yc	-	-	
	tune_albedo_wso	-	(0.052, -0.097)	
	tune_box_liq_asy	3.25	3.23	(similar
	tune_box_liq	0.05	0.061	to
	rat_sea	0.8	0.9	C2I268c)
	rlam_heat	10	7.10	
	rat_lam	1.0	1.03	
	rsmin_fac	1.0	1.36	
C2I301c	setup as C2I291c but adaptation of tune_albedo_wso			
	lterra_urb	.false.	.true.	

Code and data availability. The ICON release icon-2024.07 (<https://doi.org/10.35089/WDC/IconRelease2024.07>, ICON partnership (DWD, MPI-M, DKRZ, KIT, C2SM), 2024) was used for the final configuration. Earlier and intermediate model versions used for individual model

experiments during the tuning phase are made available on demand, but results can be reproduced with the later model version within the
1065 range of model intrinsic variability.

The execution of the job workflow was managed using SPICE - Starter Package for ICON-CLM Experiments, specifically the version 2.3 released in February 2025 (<https://zenodo.org/records/10047046>, Geyer et al., 2025a), which is publicly available on Zenodo. The LiMMo framework is publicly available on Zenodo (<https://doi.org/10.5281/zenodo.14662292>, Petrov and Will, 2025).

The used external data, see Sect. 2.3.1 and Sect. 2.3.3 and the discussed variables of all test simulations are published in the Long-Term
1070 Archive of the Deutsche Klimarechenzentrum (DKRZ), see (https://www.wdc-climate.de/ui/entry?acronym=DKRZ_LTA_1155_dsg0002,
Geyer et al., 2025b). The ERA5 reanalysis data in model conformal format are publicly available at DKRZ's S3 storage (https://docs.dkrz.de/doc/datastorage/minio/storage_access.html, Geyer, 2025). The sensitivity analysis was done by using LiMMo (see Fig. 2, https://codebase.helmholtz.cloud/udag-hereon/limmo-3km/-/blob/limmo_12km_manuscript/all_params_sensitivity.ipynb?ref_type=heads&plain=0). For the
analysis and evaluation of the simulations the EvaSuite (<https://doi.org/10.5281/zenodo.17130605>) was used, the plotting was done with
1075 PlotSmart (https://gitlab.dkrz.de/g260232/plotsmart/-/tree/main/copat2_manuscript?ref_type=heads) and separate scripts (<https://doi.org/10.5281/zenodo.18078427>).

Author contributions. The paper writing was done by AW, BG, and SPe with contributions from HH, VM, SSi, ER, SH. The figure production was done by DL, SPe, SSi, CP, BG, MS, HH. The result analysis and discussion and proof reading were done by all co-authors. The simulations were done by AW, BG, KK, PL, CP, AC, HF, KG, HH, MK, VM, SPe, SSi, and MS. The development of LiMMo was done by
1080 SPe, AW, and BG. The model development was done by AW, PK, VM, plotting routine development by SPe, EC and the data management by BG, AW, SPe, HF. The preparation of the external data was done by SSi, VM, SH, BG. The conceptualisation, methodology, management of the collaboration were done by BG, AW, SPe, KK, ER; BG, AW, SPe, KK; BG, ER, CS, respectively.

Competing interests. The contact author has declared that none of the authors has any competing interests. The funders had no role in the design of the study; in the collection, analysis, or interpretation of the data; in the writing of the manuscript; or in the decision to publish the
1085 results.

Acknowledgements. We acknowledge the DKRZ for the use of resources in terms of granted computing time and storage capacity (project bg1155). Additionally, we used data from the DKRZ /pool/data section provided by the CLM Community. We acknowledge the ESA GlobCover 2009 Project providing the data set on their website (http://due.esrin.esa.int/page_globcover.php). We gratefully acknowledge the Polish weather service IMGW-PIB (Instytut Meteorologii i Gospodarki Wodnej - Państwowy Instytut Badawczy) for providing precipitation
1090 and radiation data. We also thank Philipp Heinrich for his technical support during the preparation of the manuscript. Muhammed Karadan, Divyaja Lawand, Sergei Petrov, Christopher Purr, Martina Schubert-Frisius, Shweta Singh acknowledge the financial support of the German Federal Ministry of Research, Technology and Space in the project 'Updating the data basis for adaptation to climate change in Germany (UDAG)' (grant no. 01LP2326D). Moreover, HT is thankful for the computational resources granted by the John von Neumann Institute for Computing (NIC) on the supercomputer JURECA at the Jülich Supercomputing Centre (JSC) through the grant JJSC39.

1095 **References**

- Anders, I., Brienen, S., Demuzere, M., Bucchignani, E., Ferrone, A., Geyer, B., Keuler, K., Lüthi, D., Mertens, M., Osterried, K., Panitz, H.-J., Saeed, S., Sørland, S. L., and Schulz, J.-P.: Evaluation Report COSMO-CLM5.0, <https://doi.org/10.5281/zenodo.14515358>, 2024.
- Andersson, A., Fennig, K., Klepp, C., Bakan, S., Graßl, H., and Schulz, J.: The Hamburg Ocean Atmosphere Parameters and Fluxes from Satellite Data - HOAPS-3, *Earth System Science Data*, v.2, 215-234 (2010), 3, <https://doi.org/10.5194/essd-2-215-2010>, 2010.
- 1100 Andersson, A., Graw, K., Schröder, M., Fennig, K., Liman, J., Bakan, S., Hollmann, R., and Klepp, C.: Hamburg Ocean Atmosphere Parameters and Fluxes from Satellite Data - HOAPS 4.0, https://doi.org/10.5676/EUM_SAF_CM/HOAPS/V002, 2017.
- Avgoustoglou, E., Carmona, I., Voudouri, A., Levi, Y., Will, A., and Bettems, J.-M.: Calibration of COSMO model in the Central-Eastern Mediterranean area adjusted over the domains of Greece and Israel, *Atmospheric Research*, 279, 106362, <https://doi.org/10.1016/j.atmosres.2022.106362>, 2022.
- 1105 Bechtold, P., Köhler, M., Jung, T., Doblas-Reyes, F., Leutbecher, M., Rodwell, M. J., Vitart, F., and Balsamo, G.: Advances in simulating atmospheric variability with the ECMWF model: From synoptic to decadal time-scales, *Quarterly Journal of the Royal Meteorological Society*, 134, 1337–1351, <https://doi.org/10.1002/qj.289>, 2008.
- Bellprat, O., Kotlarski, S., Lüthi, D., and Schär, C.: Objective calibration of regional climate models, *Journal of Geophysical Research: Atmospheres*, 117, <https://doi.org/10.1029/2012JD018262>, 2012.
- 1110 Bellprat, O., Kotlarski, S., Lüthi, D., Elía, R., Frigon, A., Laprise, R., and Schär, C.: Objective Calibration of Regional Climate Models: Application over Europe and North America, *Journal of Climate*, 29, 819–838, <https://doi.org/10.1175/jcli-d-15-0302.1>, 2016.
- Bennartz, R. and Rausch, J.: Global and regional estimates of warm cloud droplet number concentration based on 13 years of AQUA-MODIS observations, *Atmospheric Chemistry and Physics*, 17, 9815–9836, <https://doi.org/10.5194/acp-17-9815-2017>, 2017.
- Broyden, C. G.: The Convergence of a Class of Double-Rank Minimization Algorithms 2. The New Algorithm, *IMA Journal of Applied Mathematics*, 6, 222–231, <https://doi.org/10.1093/imamat/6.3.222>, 1970.
- 1115 Byrd, R. H., Lu, P., Nocedal, J., and Zhu, C.: A Limited Memory Algorithm for Bound Constrained Optimization, *SIAM Journal on Scientific Computing*, 16, 1190–1208, <https://doi.org/10.1137/0916069>, 1995.
- Campanale, A., Adinolfi, M., Raffa, M., Schulz, J.-P., and Mercogliano, P.: Investigating urban heat islands over Rome and Milan during a summer period through the TERRA_URB parameterization in the ICON model, *Urban Climate*, 60, 102335, <https://doi.org/10.1016/j.uclim.2025.102335>, 2025.
- 1120 Checa-Garcia, R.: CMIP6 Ozone forcing dataset: supporting information, <https://doi.org/10.5281/zenodo.1135127>, 2018.
- Coddington, O., Lean, J. L., Pilewskie, P., Snow, M., and Lindholm, D.: A Solar Irradiance Climate Data Record, *Bulletin of the American Meteorological Society*, 97, 1265 – 1282, <https://doi.org/10.1175/BAMS-D-14-00265.1>, 2016.
- CORDEX: CORDEX experiment design for dynamical downscaling of CMIP6 (Version v2)., <https://doi.org/10.5281/zenodo.15268192>, 2025.
- 1125 Cornes, R., van der Schrier, G., van den Besselaar, E., and Jones, P.: An ensemble version of the E-OBS temperature and precipitation data sets, *Journal of Geophysical Research: Atmospheres*, 123, 9391–9409, <https://doi.org/10.1029/2017jd028200>, 2018.
- Deutscher Wetterdienst: Klimadaten zum direkten Download, https://opendata.dwd.de/climate_environment/CDC/observations_germany/climate/hourly/, 2025.
- 1130 DWD: DAS-Basisdienst ‘Klima und Wasser’, https://www.das-basisdienst.de/DAS-Basisdienst/DE/home/home_node.html, accessed: 2025-09-16, 2023.

- EURO-CORDEX: List of published parameters, <https://confluence.ecmwf.int/display/CKB/CORDEX:+Regional+climate+projections#CORDEX:Regionalclimateprojections-Listofpublishedparameters>, 2025.
- European Space Agency and Université Catholique de Louvain: GlobCover 2009 Project (GlobCover2009_V2.3), http://due.esrin.esa.int/page_globcover.php, land cover dataset produced by ESA and UCLouvain, 2010.
- 1135 Eyering, V., Bony, S., Meehl, G. A., A., S. C., Stevens, B., Stouffer, R. J., and E., T. K.: Overview of the Coupled Model Intercomparison Project Phase 6 (CMIP6) experimental design and organization, *Geoscientific Model Development*, 9, 1937–1958, <https://doi.org/10.5194/gmd-9-1937-2016>, 2016.
- FAO and IIASA: Harmonized World Soil Database Version 2.0, Rome and Laxenburg, <https://doi.org/10.4060/cc3823en>, 2023.
- 1140 Fiedler, S., Stevens, B., Gidden, M., Smith, S. J., Riahi, K., and van Vuuren, D.: First forcing estimates from the future CMIP6 scenarios of anthropogenic aerosol optical properties and an associated Twomey effect, *Geoscientific Model Development*, 12, 989–1007, <https://doi.org/10.5194/gmd-12-989-2019>, 2019.
- Food and Agriculture Organization of the United Nations: Digital Soil Map of the World, FAO, Land and Water Division, ISBN 978-92-3-103889-1, cD-ROM; cartographic material; original scale 1:5,000,000, 2003.
- 1145 Früh, B.: Aktualisierung der Datengrundlage für die Anpassung an den Klimawandel in Deutschland, https://www.dwd.de/DE/forschung/projekte/udag/udag_node.html, accessed: 2025-09-16, 2023.
- Gao, C., Zhang, X., Yang, H., Huang, L., Zhao, H., Zhang, S., and Xiu, A.: The role of dust mineral composition in atmospheric radiation and pollution in North China: new insights from EMIT and two-way coupled modeling, *Atmospheric Chemistry and Physics*, 26, 3765–3781, <https://doi.org/10.5194/acp-26-3765-2026>, 2026.
- 1150 Geyer, B.: ERA5 reanalysis data, converted to ICON-CLM input format, s3 storage address: 3dkrz/pd1309/forcings/reanalyses/ERA5, 2025.
- Geyer, B.: A novel evaluation metric to determine an optimal regional climate model configuration applied for COSMO-CLM 6.0, *Earth and space science*, <https://doi.org/placeholder>, 2026.
- Geyer, B., Churiulin, E., Jähn, M., Brienens, S., Truhetz, H., Poll, S., and Rockel, B.: SPICE (Starter Package for ICON-CLM Experiments), <https://doi.org/10.5281/zenodo.10047046>, last access: Aug. 2025, 2025a.
- 1155 Geyer, B., Will, A., Keuler, K., Campanale, A., Feldmann, H., Goergen, K., Ho-Hagemann, H., Karadan, M., Ludwig, P., Maurer, V., Petrov, S., Poll, S., Pothapakula, P., Purr, C., Russo, E., Schubert-Frisius, M., Singh, S., and Sulis, M.: COPAT2 - ICON-CLM test simulations towards the optimal setup of ICON-CLM-2024.07, https://www.wdc-climate.de/ui/entry?acronym=DKRZ_LTA_1155_dsg0002, 2025b.
- Gregoire, L., Valdes, P., Payne, A., and Kahana, R.: Optimal tuning of a GCM using modern and glacial constraints, *Climate Dynamics*, 37, 705–719, <https://doi.org/10.1007/s00382-010-0934-8>, 2011.
- 1160 Grosvenor, D. P., Sourdeval, O., Zuidema, P., Ackerman, A., Alexandrov, M. D., Bennartz, R., Boers, R., Cairns, B., Chiu, J. C., Christensen, M., Deneke, H., Diamond, M., Feingold, G., Fridlind, A., Hünerbein, A., Knist, C., Kollias, P., Marshak, A., McCoy, D., Merk, D., Painemal, D., Rausch, J., Rosenfeld, D., Russchenberg, H., Seifert, P., Sinclair, K., Stier, P., van Diedenhoven, B., Wendisch, M., Werner, F., Wood, R., Zhang, Z., and Quaas, J.: Remote Sensing of Droplet Number Concentration in Warm Clouds: A Review of the Current State of Knowledge and Perspectives, *Review of Geophysics*, 56, 409–453, <https://doi.org/10.1029/2017rg000593>, 2018.
- 1165 Gryspeerdt, E., McCoy, D. T., Crosbie, E., Moore, R. H., Nott, G. J., Painemal, D., Small-Griswold, J., Sorooshian, A., and Ziemba, L.: The impact of sampling strategy on the cloud droplet number concentration estimated from satellite data, *Atmospheric Measurement Techniques*, 15, 3875–3892, <https://doi.org/10.5194/amt-15-3875-2022>, 2022.
- Hersbach, H., Bell, B., Berrisford, P., Hirahara, S., Horányi, A., Muñoz-Sabater, J., Nicolas, J., Peubey, C., Radu, R., Schepers, D., Simmons, A., Soci, C., Abdalla, S., Abellan, X., Balsamo, G., Bechtold, P., Biavati, G., Bidlot, J., Bonavita, M., De, Giovanna, D., Dahlgren,

- 1170 P., Dee, D., Diamantakis, M., Dragani, R., Flemming, J., Forbes, R., Fuentes, M., Geer, A., Haimberger, L., Healy, S., J., Robin, J., Hólm, E., Janisková, M., Keeley, S., Laloyaux, P., Lopez, P., Lupu, C., Radnoti, G., de, Patricia, d., Rozum, I., Vamborg, F., Villaume, S., and Thépaut, J.-N.: The ERA5 global reanalysis, *Quarterly Journal of the Royal Meteorological Society*, 146, 1999–2049, <https://doi.org/10.1002/qj.3803>, 2020.
- Ho-Hagemann, H. T. M., Maurer, V., Poll, S., and Fast, I.: Coupling the regional climate model ICON-CLM v2.6.6 to the Earth system
1175 model GCOAST-AHOI v2.0 using OASIS3-MCT v4.0, *Geoscientific Model Development*, 17, 7815–7834, <https://doi.org/10.5194/gmd-17-7815-2024>, 2024.
- Hodson, T. O.: Root-mean-square error (RMSE) or mean absolute error (MAE): when to use them or not, *Geoscientific Model Development*, 15, 5481–5487, <https://doi.org/10.5194/gmd-15-5481-2022>, 2022.
- Hogan, R. J. and Bozzo, A.: A Flexible and Efficient Radiation Scheme for the ECMWF Model, *Journal of Advances in Modeling Earth
1180 Systems*, 10, 1990–2008, <https://doi.org/10.1029/2018ms001364>, 2018.
- Hourdin, F., Mauritsen, T., Gettelman, A., Golaz, J.-C., Balaji, V., Duan, Q., Folini, D., Ji, D., Klocke, D., Qian, Y., Rauser, F., Rio, C., Tomassini, L., Watanabe, M., and Williamson, D.: The Art and Science of Climate Model Tuning, *Bulletin of the American Meteorological Society*, 98, 589 – 602, <https://doi.org/10.1175/BAMS-D-15-00135.1>, 2017.
- Hourdin, F., Ferster, B., Deshayes, J., Mignot, J., Musat, I., and Williamson, D.: Toward machine-assisted tuning avoiding the underestimation
1185 of uncertainty in climate change projections, *Science Advances*, 9, eadf2758, <https://doi.org/10.1126/sciadv.adf2758>, 2023.
- ICON partnership (DWD, MPI-M, DKRZ, KIT, C2SM): ICON release 2024.07, <https://doi.org/10.35089/WDCC/ICONRELEASE2024.07>, 2024.
- Inness, A., Flemming, J., Suttie, M., and Jones, L.: GEMS data assimilation system for chemically reactive gases, <https://doi.org/10.21957/jdo65q77d>, 2009.
- 1190 Inness, A., Blechschmidt, A.-M., Bouarar, I., Chabrilat, S., Crepulja, M., Engelen, R. J., Eskes, H., Flemming, J., Gaudel, A., Hendrick, F., Huijnen, V., Jones, L., Kapsomenakis, J., Katragkou, E., Keppens, A., Langerock, B., de Mazière, M., Melas, D., Parrington, M., Peuch, V. H., Razinger, M., Richter, A., Schultz, M. G., Suttie, M., Thouret, V., Vrekoussis, M., Wagner, A., and Zerefos, C.: Data assimilation of satellite-retrieved ozone, carbon monoxide and nitrogen dioxide with ECMWF’s Composition-IFS, *Atmospheric Chemistry and Physics*, 15, 5275–5303, <https://doi.org/10.5194/acp-15-5275-2015>, 2015.
- 1195 Jungclaus, J. H., Lorenz, S. J., Schmidt, H., Brovkin, V., Brüggemann, N., Chegini, F., Crüger, T., De-Vrese, P., Gayler, V., Giorgetta, M. A., Gutjahr, O., Haak, H., Hagemann, S., Hanke, M., Ilyina, T., Korn, P., Kröger, J., Linardakis, L., Mehlmann, C., Mikolajewicz, U., Müller, W. A., Nabel, J. E. M. S., Notz, D., Pohlmann, H., Putrasahan, D. A., Raddatz, T., Ramme, L., Redler, R., Reick, C. H., Riddick, T., Sam, T., Schneck, R., Schnur, R., Schupfner, M., von Storch, J.-S., Wachsmann, F., Wieners, K.-H., Ziemann, F., Stevens, B., Marotzke, J., and Claussen, M.: The ICON Earth System Model Version 1.0, *Journal of Advances in Modeling Earth Systems*, 14, e2021MS002 813,
1200 <https://doi.org/10.1029/2021ms002813>, 2022.
- Katragkou, E., Sobolowski, S. P., Teichmann, C., Solmon, F., Pavlidis, V., Rechid, D., Hoffmann, P., Fernandez, J., Nikulin, G., and Jacob, D.: Delivering an Improved Framework for the New Generation of CMIP6-Driven EURO-CORDEX Regional Climate Simulations, *Bulletin of the American Meteorological Society*, 105, E962–E974, <https://doi.org/10.1175/BAMS-D-23-0131.1>, 2024.
- Kinne, S.: The MACv2 aerosol climatology, *Tellus B: Chemical and Physical Meteorology*, pp. 1–21,
1205 <https://doi.org/10.1080/16000889.2019.1623639>, 2019a.
- Kinne, S.: Aerosol radiative effects with MACv2, *Atmospheric Chemistry and Physics*, 19, 10 919–10 959, <https://doi.org/10.5194/acp-19-10919-2019>, 2019b.

- Loeb, N. G., Doelling, D. R., Wang, H., Su, W., Nguyen, C., Corbett, J. G., Liang, L., Mitrescu, C., Rose, F. G., and Kato, S.: Clouds and the Earth's Radiant Energy System (CERES) Energy Balanced and Filled (EBAF) Top-of-Atmosphere (TOA) Edition-4.0 Data Product, *Journal of Climate*, 31, 895–918, <https://doi.org/10.1175/jcli-d-17-0208.1>, 2018.
- 1210 Lott, F. and Miller, M. J.: A new subgrid-scale orographic drag parametrization: Its formulation and testing, *Quarterly Journal of the Royal Meteorological Society*, 123, 101–127, <https://doi.org/10.1002/qj.49712353704>, 1997.
- Matthes, K., Funke, B., Andersson, M. E., Barnard, L., Beer, J., Charbonneau, P., Clilverd, M. A., Dudok de Wit, T., Haberreiter, M., Hendry, A., Jackman, C. H., Kretzschmar, M., Kruschke, T., Kunze, M., Langematz, U., Marsh, D. R., Maycock, A. C., Misios, S., Rodger, C. J., Scaife, A. A., Seppälä, A., Shangguan, M., Sinnhuber, M., Tourpali, K., Usoskin, I., van de Kamp, M., Verronen, P. T., and Versick, S.: Solar forcing for CMIP6 (v3.2), *Geoscientific Model Development*, 10, 2247–2302, <https://doi.org/10.5194/gmd-10-2247-2017>, 2017.
- 1215 Maurer, V., Düsterhöft-Wriggers, W., Beddig, R., Meyer, J., Hinrichs, C., Ho-Hagemann, H., Staneva, J., Ehlers, B.-M., and Janssen, F.: Evaluation of coupled and uncoupled ocean-ice-atmosphere simulations using icon_2024.07 and NEMOv4.2.0 for the EURO-CORDEX domain, *EUGsphere*, 2025, 1–48, <https://doi.org/10.5194/egusphere-2025-3407>, 2025.
- 1220 Mauritsen, T. and Roeckner, E.: Tuning the MPI-ESM1.2 Global Climate Model to Improve the Match With Instrumental Record Warming by Lowering Its Climate Sensitivity, *Journal of Advances in Modeling Earth Systems*, 12, e2019MS002037, <https://doi.org/10.1029/2019MS002037>, 2020.
- Mauritsen, T., Stevens, B., Roeckner, E., Cruieger, T., Esch, M., Giorgetta, M., Haak, H., Jungclaus, J., Klocke, D., Matei, D., Mikolajewicz, U., Notz, D., Pincus, R., Schmidt, H., and Tomassini, L.: Tuning the climate of a global model, *Journal of Advances in Modeling Earth Systems*, 4, <https://doi.org/10.1029/2012MS000154>, 2012.
- 1225 Mironov, D.: Parameterization of lakes in numerical weather prediction. Description of a lake model., Tech. rep., Deutscher Wetterdienst, https://doi.org/10.5676/DWD_pub/nwv/cosmo-tr_11, 2008.
- Mironov, D., Ritter, B., Schulz, J.-P., Buchhold, M., Lange, M., and Machulskaya, E.: Parameterisation of sea and lake ice in numerical weather prediction models of the German Weather Service, *Tellus A: Dynamic Meteorology and Oceanography*, 64, 17330, <https://doi.org/10.3402/tellusa.v64i0.17330>, 2012.
- 1230 Müller, W. A., Früh, B., Korn, P., Potthast, R., Baehr, J., Bettems, J.-M., Bölöni, G., Brienen, S., Fröhlich, K., Helmert, J., Jungclaus, J., Köhler, M., Lorenz, S., Schneidereit, A., Schnur, R., Schulz, J.-P., Schlemmer, L., Sgoff, C., Pham, T. V., Pohlmann, H., Vogel, B., Vogel, H., Wirth, R., Zaehle, S., Zängl, G., Stevens, B., and Marotzke, J.: ICON: Towards vertically integrated model configurations for numerical weather prediction, climate predictions and projections, *Bams*, <https://doi.org/10.1175/bams-d-24-0042.1>, 2025.
- 1235 NASA/LARC/SD/ASDC: CERES Energy Balanced and Filled (EBAF) TOA Monthly means data in netCDF Edition4.1, https://doi.org/10.5067/terra-aqua/ceres/ebaf-toa_13b004.1, 2019.
- Neelin, J., Bracco, A., Luo, H., McWilliams, J., and Meyerson, J.: Considerations for parameter optimization and sensitivity in climate models, *Proceedings of the National Academy of Sciences of the United States of America*, 107, 21349–54, <https://doi.org/10.1073/pnas.1015473107>, 2010.
- 1240 Orr, A., Bechtold, P., Scinocca, J., Ern, M., and Janiskova, M.: Improved Middle Atmosphere Climate and Forecasts in the ECMWF Model through a Nonorographic Gravity Wave Drag Parameterization, *Journal of Climate*, 23, 5905–5926, <https://doi.org/10.1175/2010jcli3490.1>, 2010.
- Petrov, S. and Will, A.: LiMMo (Linear Meta-Model optimization for regional climate model), <https://doi.org/10.5281/ZENODO.14662291>, 2025.

- 1245 Petrov, S., Will, A., and Geyer, B.: Linear Meta-Model optimization for regional climate models (LiMMo version 1.0), *Geoscientific Model Development*, 18, 6177–6194, <https://doi.org/10.5194/gmd-18-6177-2025>, 2025.
- Pham, T. V., Steger, C., Rockel, B., Keuler, K., Kirchner, I., Mertens, M., Rieger, D., Zängl, G., and Früh, B.: ICON in Climate Limited-area Mode (ICON release version 2.6.1): a new regional climate model, *Geoscientific Model Development*, 14, 985–1005, <https://doi.org/10.5194/gmd-14-985-2021>, 2021.
- 1250 Prill, F., Reinert, D., Rieger, D., and Zängl, G.: Working with the ICON Model, Tech. rep., Deutscher Wetterdienst, https://doi.org/10.5676/dwd_pub/nwv/icon_tutorial2024, 2024.
- Raschendorfer, M.: The New Turbulence Parameterization of LM. COSMO Newsletter No. 1, Consortium for Small-Scale Modelling, Tech. rep., Consortium for Small-Scale Modelling, <http://www.cosmo-model.org>, 2001.
- Rieger, D.: ecRad in ICON Implementation Overview, Tech. rep., Deutscher Wetterdienst, [https://doi.org/10.5676/DWD pub/nwv/icon_004](https://doi.org/10.5676/DWD_pub/nwv/icon_004),
1255 2019.
- Schaaf, C. and Wang, Z.: MODIS/Terra+Aqua BRDF/Albedo Daily L3 Global - 500m V061, <https://doi.org/10.5067/MODIS/MCD43A3.061>, 2021.
- Schär, C., Leuenberger, D., Fuhrer, O., Lüthi, D., and Girard, C.: A New Terrain-Following Vertical Coordinate Formulation for Atmospheric Prediction Models, *Monthly Weather Review*, 130, 2459–2480, [https://doi.org/10.1175/1520-0493\(2002\)130<2459:antfvc>2.0.co;2](https://doi.org/10.1175/1520-0493(2002)130<2459:antfvc>2.0.co;2),
1260 2002.
- Schlemmer, L., Schär, C., Lüthi, D., and Strebel, L.: A Groundwater and Runoff Formulation for Weather and Climate Models, *Journal of Advances in Modeling Earth Systems*, 10, 1809–1832, <https://doi.org/10.1029/2017ms001260>, 2018.
- Schrodin, R. and Heise, E.: The Multi-Layer Version of the DWD Soil Model TERRA_LM, Tech. rep., Consortium for Small-Scale Modelling, <http://www.cosmo-model.org>, 2001.
- 1265 Schrum, C.: Coastal Futures, <https://www.coastalfutures.de>, accessed: 2025-09-16, 2021.
- Schulz, J.-P.: Introducing sub-grid scale orographic effects in the COSMO model, in: COSMO Newsletter No. 9, edited by Schättler, U., Montani, A., and Milelli, M., pp. 29–36, Deutscher Wetterdienst, Offenbach am Main, Germany, -URL <https://www.cosmo-model.org/content/model/documentation/newsLetters/newsLetter09>, 2008.
- Schulz, J.-P. and Vogel, G.: Improving the processes in the land surface scheme TERRA: Bare soil evaporation and skin temperature, *Atmosphere*, 11, 513, <https://doi.org/10.3390/atmos11050513>, 2020.
- 1270 Schulz, J.-P., Vogel, G., Becker, C., Kothe, S., Rummel, U., and Ahrens, B.: Evaluation of the ground heat flux simulated by a multi-layer land surface scheme using high-quality observations at grass land and bare soil, *Meteorologische Zeitschrift*, 25, 607–620, <https://doi.org/10.1127/metz/2016/0537>, 2016.
- Schulz, J.-P., Mercogliano, P., Adinolfi, M., Apreda, C., Bassani, F., Bucchignani, E., Campanale, A., Cinquegrana, D., Lucia, C. D., Dumitrache, R., Fedele, G., Garbero, V., Interewicz, W., Iriza-Burca, A., Jaczewski, A., Khain, P., Levi, Y., Maco, B., Mandal, A., Milelli, M., and the COSMO PP CITTA' team: A new urban parameterisation for the ICON atmospheric model, EMS Annual Meeting 2022, Ems2022-501, <https://doi.org/10.5194/ems2022-501>, 2022.
- 1275 Seifert, A.: A Revised Cloud Microphysical Parameterization for COSMO-LME, <http://www.cosmo-model.org/content/model/documentation/newsLetters/newsLetter07/default.htm>, 2008.
- 1280 Sicard, M., Bertolín, S., Mallet, M., Dubuisson, P., and Comerón, A.: Estimation of mineral dust long-wave radiative forcing: sensitivity study to particle properties and application to real cases in the region of Barcelona, *Atmospheric Chemistry and Physics*, 14, 9213–9231, <https://doi.org/10.5194/acp-14-9213-2014>, 2014.

- Sieck, K.: NUKLEUS - Nutzbare Lokale Klimainformationen für Deutschland, <https://www.fona.de/de/massnahmen/foerdermassnahmen/RegIKlim/nukleus.php>, accessed: 2025-09-16, 2020.
- 1285 Sieck, K., Pinto, J. G., Geyer, B., Keuler, K., Beier, C., Braun, C., Ehmele, F., Feldmann, H., Frisius, T., Heinrich, P., Hundhausen, M., Petrik, R., and Trachte, K.: NUKLEUS - A First Kilometre Scale Multi-model Climate Ensemble for Germany: Evaluation, *Geoscientific Model Development*, submitted, 2026.
- Stenchikov, G. L., Kirchner, I., Robock, A., Graf, H.-F., Antuna, J. C., Grainger, R. G., Lambert, A., and Thomason, L.: Radiative forcing from the 1991 Mount Pinatubo volcanic eruption, *J. Geophys. Res.: Atmos.*, 103, 13 837–13 857, 1998.
- 1290 Stevens, B., Giorgetta, M., Esch, M., Mauritsen, T., Crueger, T., Rast, S., Salzmann, M., Schmidt, H., Bader, J., Block, K., Brokopf, R., Fast, I., Kinne, S., Kornblueh, L., Lohmann, U., Pincus, R., Reichler, T., and Roeckner, E.: Atmospheric component of the MPI-M Earth System Model: ECHAM6, *Journal of Advances in Modeling Earth Systems*, 5, 146–172, <https://doi.org/10.1002/jame.20015>, 2013.
- Stevens, B., Fiedler, S., Kinne, S., Peters, K., Rast, S., Müsse, J., Smith, S. J., and Mauritsen, T.: MACv2-SP: a parameterization of anthropogenic aerosol optical properties and an associated Twomey effect for use in CMIP6, *Geoscientific Model Development*, 10, 433–452, <https://doi.org/10.5194/gmd-10-433-2017>, 2017.
- 1295 Team, G. T., Hastings, D. A., Dunbar, P. K., Elphinstone, G. M., Bootz, M., Murakami, H., Maruyama, H., Masaharu, H., Holland, P., Payne, J., Bryant, N. A., Logan, T. L., Muller, J.-P., Schreier, G., and MacDonald, J. S.: The Global Land One-kilometer Base Elevation (GLOBE) Digital Elevation Model, Version 1.0, <https://www.ngdc.noaa.gov/mgg/topo/globe.html>, national Geophysical Data Center, NOAA, Boulder, CO, USA, 1999.
- 1300 Tegen, I., Hollrig, P., Chin, M., Fung, I., Jacob, D., and Penner, J.: Contribution of different aerosol species to the global aerosol extinction optical thickness: Estimates from model results, *Journal of Geophysical Research*, 102, 23 895–23 915, <https://doi.org/10.1029/97jd01864>, 1997.
- Tiedtke, M.: A comprehensive mass flux scheme for cumulus parameterization in large-scale models, *Monthly Weather Review*, 117, 1779–1800, [https://doi.org/10.1175/1520-0493\(1989\)117<1779:Acmsfs>2.0.co;2](https://doi.org/10.1175/1520-0493(1989)117<1779:Acmsfs>2.0.co;2), 1989.
- 1305 Williamson, D., Goldstein, M., and Blaker, A.: Fast Linked Analyses for Scenario-based Hierarchies, *Journal of the Royal Statistical Society: Series C*, 61, 665–691, <https://doi.org/10.1111/j.1467-9876.2012.01042.x>, 2012.
- Winterfeldt, J., Geyer, B., and Weisse, R.: Using QuikSCAT in the added value assessment of dynamically downscaled wind speed, *International Journal of Climatology*, 31, 1028–1039, <https://doi.org/10.1002/joc.2105>, 2011.
- Wouters, H., Demuzere, M., Blahak, U., Fortuniak, K., Maiheu, B., Camps, J., Tielemans, D., and van Lipzig, N. P. M.: The efficient urban canopy dependency parametrization (SURY) v1.0 for atmospheric modelling: description and application with the COSMO-CLM model for a Belgian summer, *Geoscientific Model Development*, 9, 3027–3054, <https://doi.org/10.5194/gmd-9-3027-2016>, 2016.
- 1310 Wouters, H., Varentsov, M., Blahak, U., Schulz, J.-P., Schättler, U., Bucchignani, E., and Demuzere, M.: User guide for TERRA_URB v2.2: The urban-canopy land-surface scheme of the COSMO model, Tech. rep., Ghent University, <http://www.cosmo-model.org>, 2017.
- Zängl, G.: Adaptive tuning of uncertain parameters in a numerical weather prediction model based upon data assimilation, *Quarterly Journal of the Royal Meteorological Society*, 149, 2861–2880, <https://doi.org/10.1002/qj.4535>, 2023.
- 1315 Zängl, G., Reinert, D., Rípodas, P., and Baldauf, M.: The ICON (ICOsahedral Non-hydrostatic) modelling framework of DWD and MPI-M: Description of the non-hydrostatic dynamical core, *Quarterly Journal of the Royal Meteorological Society*, 141, 563–579, <https://doi.org/10.1002/qj.2378>, 2015.
- Zängl, G., D., R., and F., P.: Grid refinement in ICON v2.6.4, *Geoscientific Model Development*, 15, 7153–7176, <https://doi.org/10.5194/gmd-15-7153-2022>, 2022.
- 1320

Zou, G. Y.: Toward using confidence intervals to compare correlations, *Psychological Methods*, 12, 399–413, <https://doi.org/10.1037/1082-989x.12.4.399>, 2007.